CONTROLLING MECHANICAL RESPONSE IN METAMATERIALS VIA TOPOLOGICAL STATES OF MATTER

A Dissertation
Presented to
The Academic Faculty

By

Adrien Saremi

In Partial Fulfillment
Of the Requirements for the Degree
Doctor of Philosophy in Physics

Georgia Institute of Technology

December 2020

CONTROLLING MECHANICAL RESPONSE IN METAMATERIALS VIA TOPOLOGICAL STATES OF MATTER

Approved by:

Dr. Zeb Rocklin, Advisor
School of Physics
Georgia Institute of Technology

Dr. Elisabetta Matsumoto
School of Physics
Georgia Institute of Technology

Dr. Peter Yunker
School of Physics
Georgia Institute of Technology

Dr. Martin Mourigal
School of Physics
Georgia Institute of Technology

Dr. Michael Leamy
The George W. Woodruff School of Mechanical Engineering
Georgia Institute of Technology

Date Approved: August 10, 2020

ACKNOWLEDGEMENTS

First and foremost, I'd like to thank my advisor Zeb Rocklin, who has been over these four years a great mentor and a great teacher of the sciences of theoretical soft matter. Zeb has always pushed me to surpass my limits and through his commitment, he helped me reach a level of professionalism that I lacked when I joined Georgia Tech. The road up until now has been marked with great moments of discoveries and lessons, but I would be dishonest if I claim that my commitment has always been at its best and for that, I thank Zeb for his patience and flexibility. I certainly acknowledge his help and his leadership to the production of our two peer-reviewed articles and my presentations at the APS March meetings. He has constantly been a passionate, bright, and friendly mentor and his help has greatly contributed to the accomplishment of this thesis.

I'd also like to thank the members of my research group: my colleagues Michael, Di and my friend James, who constantly provided great insights on my work and on all other aspects of our lives. I thank them for their sheer commitment to the expansion of our research within the Georgia Tech community and beyond. I'd like to extend this acknowledgement to three figures of the School of Physics: Edwin Greco, my teaching supervisor during my five years at Georgia Tech and whose work flexibility allowed me to manage both my research and TA duties at once; Alberto Fernandez-Nieves for having shared his true passion for soft matter research with me and Predrag Cvitanovic for introducing me to the beauty of nonlinearities during my first year at Tech.

I'd like to thank my parents as well and wish they would have been present for my thesis defense: my mom and her weekly video calls who have always been supporting and have helped me persevere through my research work and my dad for

his contribution to help me move and live in the United States.

It can be mentally exhausting to have my family spread across the globe, but I cherish the moments I was able to spend with all of them during my five years at Georgia Tech. First, my family in France who I had the chance to visit annually and who always brighten my morale. They will most likely be upset not to see their name in this section, so here there are: Myriam, Maxime, Denis, Damien, Caroline, Cecile, Julien, Alexandre, Florence and grandma Huguette. Second, my Persian family and friends in Alabama who I frequently traveled to visit and who helped me endure those challenging years: Mancy, Mohssen, Pooya, Borna, Aria, Ali, Elnaz, Rachael, Eila, Michael, Greg, and my lovely girlfriend Betssi. Finally, I'd like to thank my colleagues and friends from Georgia Tech, whom I started this journey with in 2015: Shashank, Chun-Fai, Zack, Maryrose, Hemaa, Rana, Natalie and my roommate Matt.

While most people listed in this section had little to do with the writing of this dissertation practically speaking, the bond I have with them and their support certainly helped me throughout the completion of this doctorate degree and for that reason, I acknowledge and thank them.

TABLE OF CONTENTS

Acknowledgements **iii**

List of Tables **ix**

List of Figures **xvii**

Summary **xviii**

1 Introduction **1**

1.1 Background 1

1.1.1 Historical context 1

1.1.2 The limits of conventional elasticity 2

1.2 Unconventional Elastic Systems 2

2 Topology and Mechanical Metamaterials **7**

2.1 Topological States of Matter 7

2.1.1 Introduction to topology 7

2.1.2 Topological phases of matter in quantum systems 9

2.1.3 In classical systems 10

2.1.4 In flexible mechanical metamaterials 12

2.2 Background for Mechanical Lattices 14

2.2.1 Ball and spring network 14

2.2.2 Linear theory 15

2.2.3 In reciprocal space 18

2.2.4 Topological modes in isostatic systems 20

2.2.5 Connection with other topological invariant and nonlinearities 23

2.3 Background for Continuum Theory 25
2.3.1 Stresses and forces 25
2.3.2 The rigidity and equilibrium maps in the continuum 27
2.3.3 In reciprocal space 28

3 Continuum Limit of Mechanical Metamaterials 31
3.1 Introduction 31
3.2 Effects of smooth strain field on microstructure 32
3.3 Bulk and Surface Energies 35
3.4 Equilibrium in One-Dimensional Systems 36
3.5 Relaxation and Equilibrium in the Microstructure 39
3.6 Topological polarization in the continuum 42
3.6.1 Definition of the new invariant 44
3.6.2 Topological polarization as a vector 48
3.6.3 Soft directions 49
3.7 Experimental Length Scales 51
3.8 Conclusions 53

4 Mechanical Response in Non-Ideal Systems: Boundary Effects, Additional Bonds, and Disorder 56
4.1 Boundary Effects 56
4.1.1 For a 1D system 58
4.1.2 For a 2D system 60
4.1.3 Density of Modes 62
4.2 The Response Position 65
4.2.1 Introduction And setup 66
4.2.2 Response position of the 1D rotor chain 69
4.2.3 The double spring rotor chain 73

4.3 Limited Disorder in Polarized Systems 75
4.3.1 Bond swapping in 1D 76
4.3.2 Disorder in bond's stiffness 78

5 Higher Order Topological Systems - Corner Mode 82
5.1 Introduction 82
5.1.1 A new counting argument 82
5.1.2 Topological degree of the map 84
5.2 Model Second-Order System: the Deformed Checkerboard 85
5.2.1 Constraints and the corner mode 85
5.2.2 Experimental realization 88
5.3 Conclusion 90

6 Conclusion 92

Appendix A Continuum Limit 95
A.1 Effects of Strains on Microstructure 95
A.2 Energy and Surface Terms 96
A.3 Energy Terms in One Dimension 98
A.4 New Winding Number 99
A.5 Soft Directions, Length Scales and Choice of Basis 101

Appendix B Mechanical Response 104
B.1 Displacement and Pseudo-Inverse 104
B.1.1 Uniform spring stiffness 104
B.1.2 Non-uniform spring stiffness system 105
B.1.3 Significance for the displacements $u_i^j(\mathbf{n})$ 105
B.2 Response Position 106
B.2.1 In wavenumber space 107

B.2.2 Gauge invariance of the response position 108
B.2.3 1D Maxwell chain - rotor chain 110
B.2.4 Double spring rotor chain 113
B.3 Perturbative Theory 113

Appendix C Corner Mode **117**

C.1 Complex projective space and positive degree 117
C.2 Topological Degree Theorem 118
C.3 Constraint Geometry 119
C.3.1 Ball and spring networks 120
C.3.2 Rotations of the pieces 120
C.3.3 Shearing of voids 121
C.4 Numerical calculation of topological degree 123
C.5 Change of Gauge: Additional corners 125

Bibliography **126**

LIST OF TABLES

A.1 We evaluate the energy moduli of the system considered in figure 3.2, lying in the two-dimensional (xy) plane. Each elastic moduli is invariant under permutations of the i, j, k, l indices. 98

LIST OF FIGURES

1.1 Representations of a "spring" like contact force between two soft particles in a jammed media. The magnitude of the force is proportional to the overlap δ and accounts for the softness of the sphere k. This figure is drawn from Ref. [1]. 3

2.1 On the left, a sphere we gradually deform into a cube without changing its genus ($g = 0$). On the right, a similar deformation on a one-holed torus ($g = 1$). 8

2.2 Experimental set up of an amorphous gyroscopic network explored by the Irvine group at the University of Chicago. When an excitation is imposed on a gyroscope at the boundary, the components through the bulk remain still, while those on the boundary follows a chiral edge mode which propagates clockwise [2]. 11

2.3 Visual representation of a deformed Kagome lattice with six cells along the first lattice direction $\mathbf{l}_1$ and four along the second $\mathbf{l}_2$. Each cell is made of three sites moving in two dimensions and six connecting bonds, so that the number of degrees of freedom and constraints are equal. . 15

2.4 Mapping from the bulk modes to the image space of a linear constraint map, such as the rigidity matrix. On the left, the space of all modes $z = e^{iq}$ with the contour representing the bulk modes drawn in blue. On the right, what the mapping of the bulk mode looks like in image space for three scenarios: A, where the zero mode is within the contour and hence its mapping encloses the zero; C, where the mode is outside the contour and the mapping does not enclose the zero; and B, where the zero mode lies on the bulk itself. 22

3.1 A periodic microstructure composed of bonds connecting sites, drawn from a Kagome lattice system. The bond located at $\mathbf{p}$ relative to the center $\mathbf{r}$ of the cell in which it lies, connects two sites with relative position $\mathbf{b}$. These sites undergo displacements $\mathbf{u}_1(\mathbf{r}), \mathbf{u}_2(\mathbf{r})$, which cause the spring to extend / compress. 33

3.2 (a) On a periodic system, we apply a particular strain $\epsilon_{ij}(\mathbf{r}) = (\epsilon_{xx}, \epsilon_{yy})e^{i(\mathbf{q}\cdot\mathbf{r})}$. This causes bonds to stretch (green) or compress (red). (b) The system then relaxes by projecting onto space of self-stresses that mostly capture particles displacing over short distances but reducing the energy cost overall. 40

3.3 The contour used to establish the relationship between bulk structure and zero modes. In the complex plane of q_x, the contour starts at $+\epsilon/|\mathbf{l}_1|$ goes counter-clockwise over the upper arc (dashed), then over the upper real part (solid) from left to right, then clockwise over the lower arc (dashed), and finally over the lower real part (from left to right) to come back to its starting point. As explained in the text, the two dashed portions cancel out and the difference between modes with positive and negative imaginary parts is given by the solid lines only. 46

3.4 (a) Topological transition as we deform the Kagome lattice. Its geometry is parametrized as $\mathbf{g}(x) = x\mathbf{g}_1 + (1-x)\mathbf{g}_2$. $\kappa_\pm$ are the signed inverse decay lengths, such that when one vanishes the associated mode lies in the bulk and when both have the same sign the system is polarized. (b) The system in the $\mathbf{g}_1$-configuration with trivial polarization along $\hat{r}_n$: the two zero modes are split between the two edges. (c) The system is topologically polarized this time ($\Delta N = 2$): this time, the two modes are on the left side $\hat{r}_n$. On all three figures, the purple dashed lines represent the shape of the system at the topological transition (when $x = 0.7$). 47

3.5 (a) For a fixed deformed Kagome, we numerically compute the signed inverse decay length of each mode $(\kappa_-(\theta), \kappa_+(\theta))$ and the topological polarization $\Delta N(\theta)$ of Eq. (3.30). We do so as a function of the normal direction $\hat{r}_n(\theta)$. (b) A chunk of the system in the bulk which highlights the presence of soft directions (orange lines). The polarization $\Delta N(\theta)$ changes as the normal crosses either soft directions. Between the split regions, the presence the two $\pm$ edge modes is highlighted by the arcs (respectively red / blue). 50

3.6 Shape of the two edge modes in a system with polarization $\Delta N = 2$. On the boundary, which is oriented along $\hat{r}_t$, we impose a mode with wavelength $\lambda = 15.6\,|\mathbf{l}_1|$ (where $\mathbf{l}_1$ is the first lattice primitive vector of the microstructure). The modes then decay through the bulk, along the direction $\hat{r}_n$ and over length scales much longer than the imposed wavelength λ. Each mode (red, blue) varies sinusoidally along its corresponding soft direction and therefore also varies along the boundary. 52

4.1 Deformed Kagome lattice with open boundaries along the first lattice direction ($\mathbf{l}_1$), periodic along the second ($\mathbf{l}_2$). We compute the polarization for a 35×15 cells system from Eq. (4.1) and find $P = -0.96$ and plot the spatial extent of the edge modes in yellow. 58

4.2 Representation of the SSH model for polyacetylene via the 1D isostatic chain of rotors connected by springs. For each of the two topological configurations considered, the SSH model is drawn with its corresponding 1D rotor chain (left figures vs right figures). On the left, we have the trivial state: (a) sublattices A (blue) and B (red squares) are connected by a unique type of bonds while (c) represents the 1D chain of rotors, positioned vertically in equilibrium. On the right, we have the nontrivial state: (b) the dimerized state of the SSH model and its corresponding 1D chain (d) where the rotors are slightly tilted by an angle $\bar{\theta}$ with respect to the vertical axis [3]. 59

4.3 Log-log plot of the finite polarization with respect to its expected value as a function of the system's size (the error), for the deformed Kagome lattice of figure 4.1. Given the expected value is $P = -1$, the polarization error is evaluated using Eq. (4.9) (solid line) for a system growing in size in both lattice directions $N_1 = N_2 = N$. The expected power law for the error evaluated in the continuum limit is drawn as well (dashed line). 62

4.4 Log-log plot of the density of modes through the system, where n_1 indicates the cell numbering away from the polarized edge (right) for the deformed Kagome lattice of figure 4.1. The modes' density $v(n_1)$ is evaluated using Eq. (4.16) (solid line) for a system with $N = 100$ cells. The expected power law for the modes' density is evaluated in the continuum limit (dashed). 64

4.5 The response of unpolarized (left) vs polarized (right) Kagome lattices. Blue color indicates the displacement response due to the combination of bonds swollen/contracted (a, c), while red describes the intensity levels of bonds extensions/compressions due to an applied force (b, d). This image is taken from Ref. [4]. 66

4.6 x component of the response position in the 1D Maxwell rotor chain, as we vary the "degree of polarization" b. The solid line represents the analytical derivation of such system [Eq. (4.35b)] while the dots are evaluated from the numerical formula of Eq. (4.20) for a $N = 100$ long rotor chain. 72

4.7 x component of the response position in the double rotor chain. We vary the spring stiffness of the second system k_2, while the first system stay fixed $k_1 = 1$ and so are the degree of polarization $b_1 = 0.5, b_2 = 3$. The solid line cross the x-axis as we tune the value of k_2, indicating the response position goes from right to left. 74

4.8 Response deformation due to the swelling at a bond (green line) in a system with a missing bond (dashed line) and an added bond from the next nearest neighbor chain (blue line). The 1D rotor chain considered here is polarized to the right. On figure (a), the missing bond is on the opposite side of the polarization, while in (b) it is on the proper side. 77

4.9 Mechanical response in a hyperstatic system with weak secondary springs ($k_2 = 0.02$), compared to the polarized primary system ($k_1 = 1, b = 0.6$) due to swelling of bond at green line. The cyan response is one when there exists no interface of disorder. The blue response occurs when one of the secondary spring (dashed line) is tuned up $k_s = 100$. 79

5.1 Cartoon representation of different systems, all with open boundaries, lying in different dimensions d and with different order n. The top 3 figures represent conventional Maxwell systems ($n = 1$) where an imbalance of the zero modes on the edge results in bulk polarization (arrow). For those with higher-order $n \geqslant 2$, the new Maxwell rigidity results in modes in corners and edges, with new polarized elements on surfaces a dimension higher. 83

5.2 (a) Rigid quadrilateral faces are hinged at their vertices and allowed to rotate relative to one another. The faces form a void, which upon rotation of the pieces, is allowed to shear. The edges of the faces are labeled by $\mathbf{r_1}, \mathbf{r_2}, \mathbf{r_3}, \mathbf{r_4}$ and the voids are defined by the four shearing angles: $\phi_{14}, \phi_{21}, \phi_{32}, \phi_{43}$. For the system considered, the zero-energy deformation is exponentially localized in the lower left corner, with green and yellow shading indicating shearing in opposite directions and darker colors hinting at higher amplitudes. This corner mode lies between two topologically polarized edges (red arrows). 86

5.3 Using Appendix C.3.3, we can deform the piece to move the mode around the four corners. Such deformation take place by moving one of the corner of the checkerboard in the (x', y') plane [the right one on the pieces of figure 5.2 (a)] while the remaining three are fixed (black dots). The location of the moving corner of the prototype generates a zero mode computed from the geometries of the system and that is in agreement with the topological degree of the map (shading) [5]. . . . 88

5.4 (a) Prototype of the checkerboard lattice. (b) Computation of the topological character χ_{T} over a broad range of amplitudes: the topological corner mode $\hat{s}_{\mathrm{T}}$ is dominant. (c) Shape of the shearing mode in cells (n_1, n_2) with $1 \leqslant n_1, n_2 \leqslant 3$ over the same range amplitude. The experimental results are indicated by error bars, plotted along the theoretical predictions (solid lines in red, light green and dark green). 89

B.1 Geometric description of the 1D rotor chain. The end points $\mathbf{r}_1, \mathbf{r}_2$ of two consecutive rotors of length d are connected by a spring of length l (red). When the spring is at rest, each rotor makes an angle $\bar{\theta}$ with the vertical but when stretched, each rotor rotates by a additional small amount θ_i. 111

C.1 Representation of a 2×2 checkerboard pieces. The vertices A, B along the 5 connecting edges form the unit cell in the sites and bonds characterization. The angles ϕ_1, ϕ_2, ϕ_3 represent the shearing motions across each void. 121

C.2 Representation of the zero modes similar to those obtained from the deformed checkerboard lattice, in a manifold of mode coordinates' magnitude $|z_1|, |z_2|$, with the phases of z_i not shown. The "origin" of such plot is the bulk mode $|z_1| = |z_2| = 1$. Zero modes in the region of interest $\mathcal{B}$ (those exponentially localized in the lower left corner of the system) appear in the lower left quadrant of the plot, with the oriented boundary $\mathcal{B}_{\mathrm{LL}}$ of this region marked by a red arrow. This region may be extended to the right (dashed arrow) to capture the lower right corner zero modes and hence obtain the total number of modes localized to the bottom edge ($|z_2 \leqslant 1|$) with care taken for this non-compact region. Similarly, one can obtain the number of zeros in the upper-right corner, as indicated by the blue arrow, as long as a change of gauge is made. 124

SUMMARY

Flexible metamaterials are materials whose mechanics are defined by the geometrical structure of their building blocks, which allows them to possess exciting elastic properties, such as robust, programmable soft deformations. In recent years, topological states of matter have been used in metamaterials to generate mechanical responses that are protected against nonlinearities and disorder. These topological states create a *bulk-boundary correspondence*, in which the bulk structure guarantees the existence of (mechanically) conducting edge states on the boundary. While recent work by Kane and Lubensky [6] derived these surface effects for mechanical lattices that counted for equal number of degrees of freedom and constraints, we extend the topological paradigm in two ways: 1) lattices that are over-constrained and 2) continuum systems. For the former, we prove that novel deformation modes in rigid metamaterials can be found on lower-dimensional elements of the surface dictated by the degree of coordination of the unit cell. For the latter, we derive a continuum theory which uses the energetic cost of applied strains on a microstructure to derive an elastic bulk-boundary correspondence that is topological in nature. In order to observe topological soft deformations, these systems rely on a microscopic relaxation mechanism that accounts for both short-distance rearrangements of the cell and for long-wavelength strains. Finally, we use the topological nature of well-established metamaterials to quantify the mechanical response of non-ideal systems, such as those hyperstatic in nature or those with weak disorder. This work includes the introduction of a polarization and a geometric phase to quantify boundary effects and the bulk response, respectively. The purpose of this dissertation is to expand the theory of topological modes to a greater variety of flexible metamaterials.

Chapter 1
INTRODUCTION

1.1 Background

1.1.1 Historical context

Historically, there isn't evidence of well established mathematical models for the mechanics of elastic materials prior to the XIX century. The Renaissance era saw glimpses of elaborate solid mechanics studies led by historical figures like da Vinci [7] Newton [8], Hooke [9], Bernouilli [10] and Young [11]. New models were developed to quantify the mechanical properties of solid materials, to study material resistance to applied forces and to control fractures in solids. Over time, the concepts of pressures, forces, tensions were soon commonly used in the material science domain, and it was really Cauchy who in 1822 [12], formalized the theory of elasticity: shearing, expressed as a tensor, is directly related with the gradient of deformations.

Elasticity is an area of mechanical engineering with focus on systems able to distort under the influence of applied forces and able to return to their original configurations. While the industrial revolution of the 1800s saw the emergence of mechanical engineering as a formidable discipline for its various applications in machinery and transportation, part of those applications included the expansion of elastic theories as means to explain a range of natural phenomena and also to engineer deformable materials like rubber. To this day, the need to understand the mechanics of flexible materials remains essential in biological systems, soft robotics and metamaterials research, with the theory of elasticity as an important domain of study in those systems.

1.1.2 The limits of conventional elasticity

The theory of elasticity introduced by Cauchy is well summarized in the 7$^{\text{th}}$ volume of Landau and Lifshitz's Course of Theoretical Physics [13], whose first edition dates back to 1959. In this volume, it is explained that elastic materials are fundamentally defined by a linear stress and strain relationship at an infinitesimal point of the media, which is considered continuous in space. But what if the system considered is discrete in nature? Or if the deformations are so large that a nonlinear contribution must be accounted for? Or if the model needed to identify novel mechanical properties is more complex than a simple stress / strain relationship? The growth in studies of flexible systems with unconventional mechanical properties is precisely what pushed for those questions to be asked.

In recent years, models outside of the conventional theory of elasticity were built to provide novel mechanical insights of well-established systems, but also to create new artificial materials with tailor-made functionalities. In general, this type of research fits into what we define as "soft matter". Soft matter refers to the capacity of materials to deform and how their mechanical properties heavily rely on the interactions between their basic structural units [14]. Unlike hard (condensed) matter, where the connections between atoms are considered "strong" enough to not majorly influence the mechanical properties of the material, the weak and yet complex interactions between components of soft materials, their heterogenous structures and the varying length scales at which mechanical deformation occur are what make these systems particularly fascinating to study.

1.2 Unconventional Elastic Systems

Some of the systems that have benefited the most from soft matter research are granular materials [15–19]. In fact, it was reported early enough that above a certain density threshold (which directly relates to the volume fraction), suspended colloids

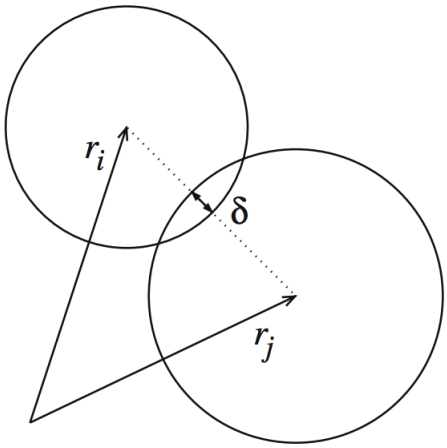

Figure 1.1: Representations of a "spring" like contact force between two soft particles in a jammed media. The magnitude of the force is proportional to the overlap δ and accounts for the softness of the sphere k. This figure is drawn from Ref. [1].

would jam, meaning they would practically behave as a solid [15–17]. Below that threshold, the particles move around and rearrange under an applied stress (similarly to a viscous material) while above, the particles are stuck and can resist external loads. This transition, similar to a phase transition between the liquid and gas states, couldn't remotely be explained by Cauchy's linear theory of elasticity. Nevertheless, it would be wrong to assume that the unjammed/jammed and liquid/solid transitions are completely alike, as the jammed state can suddenly break if the applied stress changes in nature, hence the term "fragile matter" introduced by Cates, Wittmer, Bouchaud, and Claudin [16]. Therefore, accounting for the discrete grains themselves, rather than the material as a continuous media would prove beneficial to study their mechanics. Soon, new phenomena related to the jamming transition would be discovered: formation of so-called force chains along the applied direction of compression [19], the categorization of jamming phenomena [18] and even applications in robotics [20].

At the core of these studies is the understanding of *how jammed particles act on one another*. A great number of models assume discrete contact forces between the particles themselves. While we do not claim that all forces of contact can be re-written

that way, it has been shown that the force model of soft spheres compressing against one another [1,21] can be written as a "repulsive" spring. Luding represents this very well by drawing the overlap δ between the two particles in contact (figure 1.1). While ignoring viscosity effects, such contact force can be modeled as

$$f = k\delta. \tag{1.1}$$

The key concept to remember here is the ability to formulate mechanical relationships at the particle level. Often it is optimal to know the exact distribution of the media's constituents. While some studies rely on ensemble methods which account for local average effects, for others, it is important to know the detailed structure of the material, specially when it carries a repeating pattern in space, for example, for some auxetic materials [22,23]. Auxetics are systems that have a negative Poisson ratio. With conventional materials, the Poisson ratio is positive, meaning the material if pushed on the sides will expand along the transverse direction and vice versa. But for auxetic materials, the strain along the transverse direction would increase with the axial strain. Importantly, some of these auxetic materials consists of an assemble of building blocks and their unconventional mechanical properties (auxeticity) arise from the geometrical organization of these blocks [23]. This type of structures whose mechanics depend on how repeating spatial patterns come together are called *metamaterials*. While it is true that not all metamaterials fit the statement we just wrote — in fact, a metamaterial is simply an engineered material that possesses properties that don't occur naturally — this document will heavily rely on systems that are governed by the structural arrangement of their components.

Metamaterials have also proven to be of particular use to serve as models for origami-inspired systems. Origami sheets [24–27] for example have been found functional in the design of lithium-ion batteries [24] and in the deployment of large mem-

branes in space [25]. In the context of origami as metamaterials, hidden symmetries and a robust mathematical tool named *topology* is used to program the flexibility of those systems [26, 27]. In the next chapter, we will extensively discuss what topology is and how it is responsible for various phenomena across many physical systems. Often enough, these origami sheets fit the metamaterial description we defined in the previous paragraph and additionally, their structure is modeled via a network of springs, which are deemed to represent the edges of the polygonal plates. It isn't obvious why we would use springs that potentially compress or stretch to model non-deformable origami faces, but in reality, we often use this representation and search for the sets of motions that do not stretch the springs. In return, if these springs remain at rest length, then the faces remain un-deformed. In the context of our research on metamaterials, we often search for the minimum state of the system's energy, which corresponds to the springs stretching or compressing by the minimum amount possible. The sets of deformations that stretch none of the springs in are called zero-energy modes and in the next chapter, we will elaborate on how to find them in generic networks of springs using a linear theory.

Metamaterials serve to realize auxetics and origami sheets, but their range of application doesn't stop here: some exhibit new modes of deformation corresponding to conformal maps [28] and others are the perfect manifestation of both topological effects and auxeticity, despite limited structural disorder [29]. Of course, the list of all mechanical systems whose deformations depend on their lattice structures is too exhaustive for this document. Instead, I will mention three more instances where they turn out to be useful. In living systems, the particle / spring model can be used to form a structural hierarchy of the system and has been shown to generate additional robustness to the biological material [30]. In nano-lithography, some topological mechanical materials can serve as waveguides at very high frequencies, with potential application in signal processing application [31]. And finally in fiber networks, where

the coordination number — the average number of connections of a particle with its neighbors — governs the elastic response of the material: if the connectivity is low, the fiber pretty much acts as a fluid with low shear modulus; when it is high, the network can bend, stretch or both [32]. We will see through this document that this coordination number is key to determine the nature of deformations of flexible mechanical metamaterials.

We've alluded to the significance of topology and metamaterials in mechanical systems. We will cover both of those in detail in Chapter 2 and we will reveal how these areas of research all came together through the work of Kane and Lubensky in 2014 [6]. In Chapter 3, we will cover my published work with Dr. Rocklin on the continuum limit of these topological mechanical effects [33]. Then in Chapter 4, we will cover how non-ideal mechanical lattices precisely respond to deformations, followed by the study of effects of disorder in metamaterials. In Chapter 5, we will present another piece of original work which focuses on how topology can explain the presence of flexible regions in otherwise rigid materials [5]. Finally, this document concludes with a conclusion chapter (Chapter 6) which pieces all these chapters together.

Chapter 2
TOPOLOGY AND MECHANICAL METAMATERIALS

2.1 Topological States of Matter

2.1.1 Introduction to topology

In the previous chapter, we mentioned that topology was a mathematical tool used to control the deformations of mechanical systems, for example, in origami sheets [27]. While it is true that engineered materials do not need to be topological in nature to fulfill their functionality, it is also true that topology has been a driving force in soft matter in recent years, particularly for its robust properties governing deformations in metamaterials.

In mathematics, topology is the study of properties of geometric objects that are invariant under continuous deformations. It is often said that two objects are *topologically equivalent* if one can be deformed into the other by continuous deformations, such as twisting and bending, known as homeomorphisms. Consequently, transformations such as tearing and gluing are not permitted operations [34]. A function is homeomorphic if and only if it is 1) one-to-one, 2) continuous and 3) if its inverse exists and is also continuous [34]. This class of functions, along with other important mathematical tools are critical to know for rigorous mathematical studies of topology. For us, topology is more relevant because of its range of application across multiple fields of research, particularly in physics. Hence, this document will not feature scrupulous mathematical derivations, but instead will focus on the essential topological properties.

The easiest and most common example to illustrate for topology is the genus of a two-dimensional surface, referred to popularly as the number of holes. In figure 2.1,

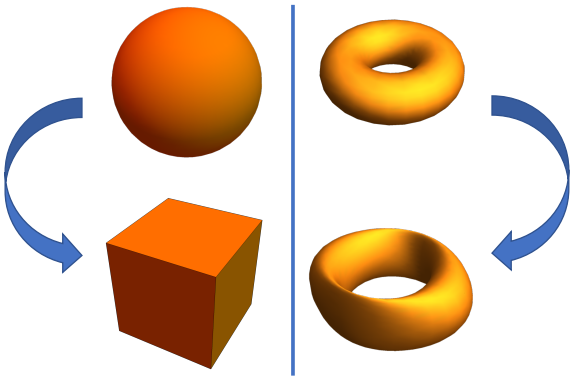

Figure 2.1: On the left, a sphere we gradually deform into a cube without changing its genus ($g = 0$). On the right, a similar deformation on a one-holed torus ($g = 1$).

we start with a simple sphere and a simple one-holed torus, which we deform without tearing through the surface. The result: the surface of a cube and a deformed torus that both carry the same number of holes as the original figures. Respectively, the sphere / cube surfaces both possess genus $g = 0$, while the tori have genus $g = 1$. Here, the surface of a cube and the sphere are perfect illustrations of topologically equivalent objects, while the genus represents a topological invariant. Even though the figures end up geometrically different from where they started, the fact their topology remained invariant is critical for boundary effects, as it directly relates to the Euler characteristic of the system, which itself relates with the integral of the gaussian curvature. For closed two-dimensional manifolds, Gauss-Bonnet theorem is [35]:

$$\oiint K dA = 2\pi(2 - 2g), \tag{2.1}$$

where K is the gaussian curvature and dA is the element of area of the surface. Of course, topological studies aren't just targeted to spheres we deform into surface of cubes. For example, topology has recently been found useful in technological applications such as spintronics [36] and quantum computing [37]. For physical systems, it can also reveal fascinating phenomena. Again, the focus here isn't on the rigorous

mathematics happening behind the scenes, but instead on the critical features of our topological methodology: it is discrete, robust and for the systems we'll consider, we'll explore how it affects properties on the system's boundary [38].

As we mentioned, topology has been used across a range of areas of research, and physical sciences are no exception. While topology is particularly featured in discrete-like systems like metamaterials [2, 6, 27, 39–42], it has proven to show great potential in continuous systems as well [43–45]. Regardless, the topological paradigm remains universal to all studies and consists in identifying a global property of the system that remains invariant under smooth deformations. This property must be discrete in nature and when it changes in value signals abrupt modifications to the nature of the system. In our case, this modification often happens on the boundaries. The research projects on topological metamaterials I conducted with Dr. Rocklin [5, 33] feature this paradigm. Before covering these projects in detail, I'll briefly remind the reader on fundamental topological studies in various physical systems.

2.1.2 Topological phases of matter in quantum systems

Quantum phases of matter is an area which first utilized topological methods to identify new states of matter, known as topological states. In 1980, Von Klitzing et al. [46] discovered that a two-dimensional Fermi gas placed in a strong transverse uniform magnetic field would exhibit quantized Hall conductance values. Their experimental result described consecutive jumps in the conductance levels of the system as the magnetic field was increased. While the connection with topological invariants was weak at the time, the reasoning behind the observed phenomenon was based on the electric conductivity being proportional to the number of Landau levels being filled — those energy states that are found below the system's Fermi energy. At the boundary of the sample, this resulted in a spike of energy potential, where the Fermi levels would cross with the filled Landau levels, resulting in local conducting states for the mobile electrons. In general, we now describe this as the Integer Quantum Hall Effect,

a variant version of the classical Hall effect in that its surface conducting behavior is quantized.

Thouless *et al.* associated the quantization of those levels with a topological invariant, that later on would be commonly referred to as the *"TKNN" invariant* [47]. Later, this would be known as the Chern number (which we explain in details in subsection 2.2.5). While the 1982 study became a benchmark over time for the exploration of topological insulators with eventually, a Nobel Prize awarded to Thouless in 2016, one important thing to remember is the presence of the magnetic field. In fact, it is shown that such a field breaks the time-reversal symmetry of the system and acts as a driving factor for the topological nature of these electronic conducting states. In the 2000s and beyond, other topological electronic systems were found, such as Kane and Mele's model of graphene [48] and the works of Bernevig, Hughes and Zhang on the presence of chiral conducting states on the edges [49]. These studies relied on the phenomenon commonly known as Quantum Spin Hall Effect, which is based on the spin-orbit interaction of electrons and which doesn't need the presence of a magnetic field. Additionally, recent work on quadrupole topological insulators [50–52] has also shown that topological conducting modes can also be located in the corners of an electronic system, rather than on the edges.

2.1.3 In classical systems

But topological states are not only limited to quantum or electronic systems: they exist in those that rely on classical mechanics. In 2015, Nash et al. [53] constructed a honeycomb lattice of gyroscopes coupled by springs. While the geometry of the lattice determines the direction of the chiral edge states, it is truly the fact that the governing forces break time-reversal symmetry, which support their topological nature. In fact, the gyroscopes' angular momenta are governed by a *first order* time evolution, like it is in the Schrödinger equation. In the energy distribution, a band gap appears. Consequently, if a mode is excited within one of the "forbidden bands"

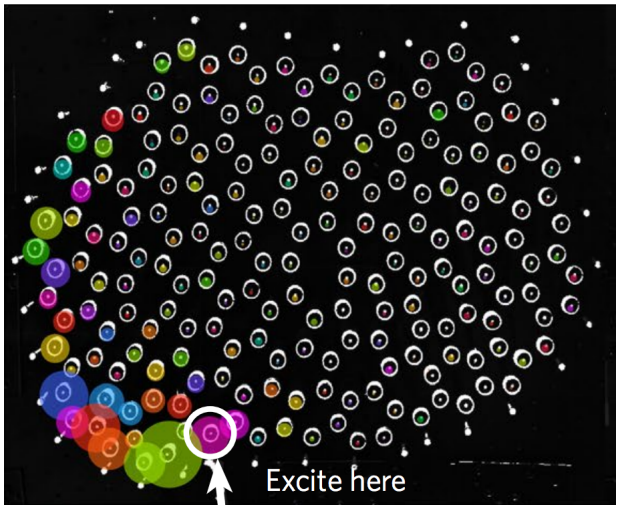

Figure 2.2: Experimental set up of an amorphous gyroscopic network explored by the Irvine group at the University of Chicago. When an excitation is imposed on a gyroscope at the boundary, the components through the bulk remain still, while those on the boundary follows a chiral edge mode which propagates clockwise [2].

it cannot propagate through the bulk of the system, but instead on its boundaries. The direction of such a wave — which does not backscatter — is then guided by the value of the Chern number evaluated on each band, which directly relates to the geometries of the repeating unit cell. Nevertheless, it has been shown that amorphous system of gyroscopes — those that are not distributed along a repeating pattern in space — can still carry the same chiral edge states, as shown in figure 2.2, as long as they undergo breaking of spatial inversion symmetry [2]. Here, since we no longer deal with a periodic structure and hence have no use of a Brillouin Zone, the Chern numbers are instead evaluated numerically in real-space. In the cited work, the disorder effects were quite strong. For our work on mechanical lattices, we'll show that weak and limited disorder effects in periodic structures do not necessarily eliminate the topological behavior as well. We will investigate this in Chapter 4.

Topological studies have also unexpectedly made quite significant impacts on other classical mechanical systems. Recent work on equatorial waves [45] has proven that the Earth's rotation and its Coriolis force break time-reversal symmetry. These are responsible for the formation of two topologically protected waves trapped at the

equator. Flocking — the collective behavior of self-propelled entities — on curved surfaces also has shown that propagating sound modes get trapped to special geodesics on the surface in the presence of spontaneous flow [44]. Meanwhile, in the system presented by Süsstrunk and Huber, lattices of coupled pendulum exhibit phononic edge modes and are supported instead by local spatial inversion symmetry of their sublattices [54]. For the four systems we've described in this section, the nature of the topological mode is protected by a nontrivial $\mathbb{Z}_2$ invariant, meaning that a change in the invariant's value corresponds to a change in the shape of the mode.

2.1.4 In flexible mechanical metamaterials

Topological states of matter are found in various mechanical systems. We will focus on their effects in the physics of flexible metamaterials [55], in particular, those that are modeled by lattices of particles that interact via Hooke's law — where the force attractive is proportional the separation distance. Since their dynamics are governed by *second order* time evolution, the mechanics of springs do not break time-reversal symmetry. While some systems still rely on the lack of spatial inversion symmetry, we particularly are interested in systems where the counting of degrees of freedom with respect to the number of constraints is important in determining its topological behavior. Those flexible mechanical metamaterials have been good illustrations of topological states of matter, with the goal of designing tailor-made mechanical responses [6, 39, 40]. Interest for mechanical metamaterials go beyond physicists: for example, the transport of molecular payloads via structure reconfiguration could have drug delivery applications [56]. In robotics, origami has been used for its self-assembling properties which persist even at the micron scale [57, 58]. A clear advantage is that metamaterials's mechanics are governed by their structure: one would expect similar mechanical behavior between nano-structures and corresponding human-sized objects, as long as their structural arrangements and the interactions are the same or topologically equivalent.

Mechanics in general are good settings for topological states to thrive. For a lot of metamaterials, linear models of deformations and stresses are simple and yet complete enough to describe topological mechanics. In section 2.2, we take full advantage of the nature of lattices governed by linear mechanics. We also use their periodic crystalline structures and to design maps between particles' displacements, bonds' extensions and forces. That way, it is easier to define mechanical lattices that exhibit topological effects that are in nature equivalent to the studies we've mentioned so far. Periodic mechanical structures are characterized by a Hamiltonian operator similar to those found in topological electronic systems [59], yielding a similar bulk-boundary correspondence as the one mentioned in the 2014 study by Kane and Lubensky [6]. While lattices of sites connected by bonds served as a model for many mechanical systems (for example, fibre networks [32]) it is truly Charles Kane and Tom Lubensky who were first to draw the topological nature of flexible metamaterials at the point of critical stability [6]. Those systems known as Maxwell systems possess equal number of degrees of freedom as constraints. The bulk-boundary correspondence depends on this particular counting argument and manifests itself via a topological polarization. This polarization is computed by searching for zero-energy deformations occurring on opposite sides of a lattice. Additionally, more mechanical phenomena can be observed as a consequence of the topological nature of such systems. For example, flexible mechanical metamaterials have shown to direct force and motion in the bulk as a result of their topological nature [4]. Topology also allows to design mechanical systems with soft modes in the bulk itself [60, 61] and with engineered topological defects [40] which are reminiscent of defects in topological insulators [62]. In origami and kirigami, topology serves to create topologically protected folding motions [27]. Even though most of the topics we study in this document involve the effects of strains and displacements of sites on microstructures, it is important to keep in mind that stresses play an equally important role in the mechanics of those materials and that

those stresses undergo similar topological effects, which for example, explain robust buckling in metamaterials [39].

The Maxwell condition plays a critical role in the essence of topological states of matter in mechanical lattices. Throughout this dissertation, we heavily rely on this condition to explore novel deformations in the context of Cauchy's elasticity [33], but also in systems that are not at the point of critical stability (even though it is contradictory in appearance) [5]. We use fundamental concepts of linear algebra to define and characterize the mechanics in theses systems.

2.2 Background for Mechanical Lattices

2.2.1 Ball and spring network

In our context, a metamaterial consists of a repeated pattern in space, with its structure as the governing core of its mechanics. In this document, we often mix up the term "metamaterials" and "lattices". While the former represents materials themselves and may allow for limited disorder in the repeating pattern, the latter truly consists of a sets of points that is invariant under discrete translations in one, two or three directions. Throughout the rest of this document, and unless told otherwise, we consider particles (or sites) distributed along a lattice pattern and which interact with their nearest neighbors via Hooke's law. The connections between them are called bonds (or constraints) and they're simply represented by springs. The extension of each bond, the forces on each site and the energy cost are determined solely by the positions of every site. We do not study effect of the masses of each site and set all of them to be unit magnitude for simplicity. The resulting picture we have in mind, for example, is shown in figure 2.3. Here, we display the structural arrangement of a deformed kagome lattice.

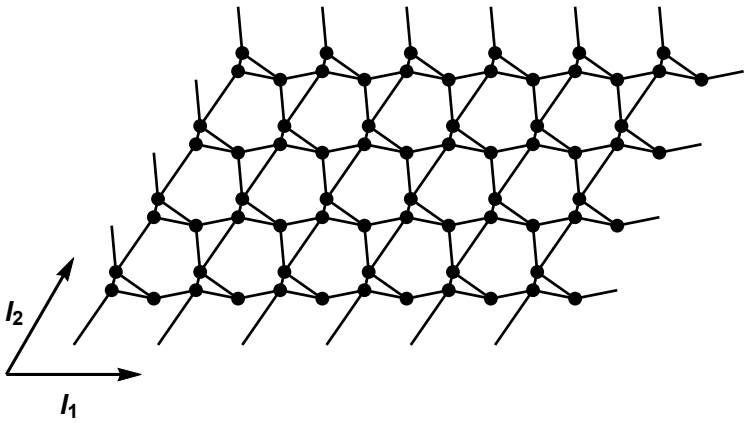

Figure 2.3: Visual representation of a deformed Kagome lattice with six cells along the first lattice direction $\mathbf{l}_1$ and four along the second $\mathbf{l}_2$. Each cell is made of three sites moving in two dimensions and six connecting bonds, so that the number of degrees of freedom and constraints are equal.

2.2.2 Linear theory

The work of Kane and Lubensky [6] relied on a counting argument relating the number of degrees of freedom and constraints. These two quantities need to be equal for the the system to qualify as "Maxwell". More generally, we allow for N_{part} particles to move in d dimensions, which account for a total of $N_{\text{d.o.f}} = d\,N_{\text{part}}$ degrees of freedom. Particles are connected to their neighbors via springs and the whole system accounts for a total of N_{con} bonds. Our linear theory relies on small displacements of these particles from their positions at rest and therefore we can derive a linear map from the space of sites' displacements $\mathbf{u}$ to the space of the bonds' extensions $\mathbf{e}$. In particular, the extension of a bond α between particles with displacements $\mathbf{u}_i$ and $\mathbf{u}_j$ is

$$e_\alpha = \hat{r}_\alpha \cdot (\mathbf{u}_i - \mathbf{u}_j), \tag{2.2}$$

where $\hat{r}_\alpha$ is the direction of the bond at rest. While nonlinear terms certainly make a contribution in reality, our model assumes those to be sufficiently small to be ignored. The mapping of all sites' displacements to all springs' extensions is given by the

rigidity map $\mathbf{R}$, which is in its matrix form

$$\mathbf{R}\,\mathbf{u} = \mathbf{e}. \tag{2.3}$$

While we do in fact refer to the displacements of sites, we can extend this linear mapping between generalized sets of coordinates $\mathbf{u}$ to a generalized constraint vector $\mathbf{e}$. Those generalized coordinates can be rotations (section 4.1) or shearing (section 5.2) for example. The "constraint" term, which often replaces the word "rigidity" is often associated with an energetic cost. Frequently, our goal is to minimize this energy by "violating" constraints as little as possible.

We've focused on displacements and springs' extensions, but such mechanical framing also allows us to determine a linear mapping between the tensions in the bonds and the generated forces on the sites they are attached to,

$$\mathbf{Q}\,\mathbf{t} = -\mathbf{f}. \tag{2.4}$$

The negative sign comes from the fact we deal with static situations and that in equilibrium, the sites do not accelerate and hence undergo external loads $+\mathbf{f}$ [3]. The *equilibrium matrix* $\mathbf{Q}$ maps the tensions in the bonds $\mathbf{t}$ to $\mathbf{f}$, the vector of d components of force of all N_{part} sites. The equilibrium matrix and rigidity matrix are related; they are transposes of one other

$$\mathbf{Q}^T = \mathbf{R}. \tag{2.5}$$

Even though it is not obvious in appearance, if we were to compute the work done by external loads on the sites and compare it with that done by the bonds' tensions and stretched springs [63], we would in principle yield the same result which prompts for the relationship written above [Eq. (2.5)]. Tensions are directly related to extensions

by the spring stiffnesses carried on each spring: $\mathbf{t} = \mathbf{Ke}$, where $\mathbf{K}$ is a diagonal matrix of stiffnesses $\{k_i\}$. Defining the *dynamical* matrix now as $\mathbf{D} = \mathbf{QKR} = \mathbf{R}^T\mathbf{KR}$, we can map directly from the displacement vector to the forces on sites by:

$$\mathbf{Du} = \mathbf{QKR}\,\mathbf{u} = \mathbf{QKe} = \mathbf{Qt} = -\mathbf{f}. \tag{2.6}$$

Frequently, we'll set those spring constants to be unit magnitude ($k_i = 1$).

We've mentioned that topological states of matter manifest via the presence of deformation modes that cost no energy to the systems. We call these deformations *zero-energy modes* as they do not stretch the bonds and, hence, lie in the null spaces of the rigidity map

$$\mathbf{Ru} = 0. \tag{2.7}$$

Self-stresses, set of bonds' extensions that do not result in forces ($\mathbf{Qe} = 0$), have as much importance as their zero mode counterparts, but our study tends to focus more on the latter. Both zero modes and self-stresses constitute force balance modes [from Eq. (2.6)] which one can obtain by minimizing the energy of the system

$$E = (1/2)\sum k_i e_i^2. \tag{2.8}$$

We'll explore this relationship in detail, when it is expressed in the continuum limit of mechanical materials in Chapter 3. We define N_{zm} and N_{ss} respectively as the number of zero modes and the number of self-stresses. The rank-nullity theorem applied to the rigidity and equilibrium matrices then implies that

$$N_{\text{zm}} + \text{rank}(\mathbf{R}) = N_{\text{d.o.f}} \tag{2.9a}$$

$$N_{\text{ss}} + \text{rank}(\mathbf{Q}) = N_{\text{con}}, \tag{2.9b}$$

but since rank($\mathbf{R}$) = rank($\mathbf{Q}$), these two equations simplify to

$$N_{\text{zm}} - N_{\text{ss}} = N_{\text{d.o.f}} - N_{\text{con}}. \tag{2.10}$$

This equality is, in the context of ball and spring systems, due to Calladine [64]. Maxwell a century earlier noted the phenomenon of redundant constraints but did not identifying self-stresses.

2.2.3 In reciprocal space

So far, the mathematical tools we've defined account for the system as a whole and they care little for the presence or absence of periodicity. Our focus is on periodic systems in d dimensions, which have a crystalline structure. We can therefore express our vectors and matrices in reciprocal space, by applying Fourier transforms (see Appendix B.1). Bloch's theorem [59, 65, 66] which is often used for periodic functions in crystals, then specifies that the displacement vector consists of an in-cell contribution which is then multiplied by a cell-to-cell factor. This factor relates to the wavenumber in reciprocal space for all d dimensions $z_i = e^{iq_i}$ so that the displacement vector of all sites in cell $\mathbf{n} = (n_1, n_2, \ldots, n_d)$ can be written as

$$\mathbf{u}(\mathbf{n}) = \mathbf{u}_0 \prod_{i=1}^{d} z_i^{n_i} = \mathbf{u}_0 \prod_{i=1}^{d} e^{iq_i n_i} \tag{2.11}$$

where $\mathbf{u}_0$ represents the vector displacement of sites within the unit cell. For a finite system with open boundary conditions [66], a mode with $|z_i| < 1 \iff \text{Im}(q_i) > 0$ indicates that the deformations are exponentially localized on the "left" side of the i^{th} lattice direction (e.g, the left, the bottom or the front of the lattice). Similarly, a bulk mode is defined by $|z_i| = 1 \iff \text{Im}(q_i) = 0$.

We'll now reason solely in reciprocal space, keeping in mind that we deal with a Bloch wave for the displacements. This allows us to reduce the dimensionality of

our overall lattice to one cell. We define $n_{\text{d.o.f}}$ and n_{con} respectively as the number of degrees of freedom and number of constraints per cell. From this concept, we raise a new definition of the rigidity matrix per cell, at a specific $\mathbf{q} = (q_1, q_2, \ldots, q_d)$ wavenumber:

$$\mathbf{R}(\mathbf{q})\,\mathbf{u}(\mathbf{q}) = \mathbf{e}(\mathbf{q}). \tag{2.12}$$

Here $\mathbf{u}$, $\mathbf{e}$ are the vector displacements and springs' extensions of respective size $n_{\text{d.o.f}}$ and n_{con} expressed in wavenumber space. Just as we did in Eqs. (2.4) and (2.5), we can derive a similar equation as Eq. (2.12) for the equilibrium matrix in reciprocal space with the caveat that $\mathbf{Q}(\mathbf{q})$ isn't precisely the transpose of $\mathbf{R}(\mathbf{q})$, but instead:

$$\mathbf{Q}(\mathbf{q}) = \mathbf{R}^T(-\mathbf{q}). \tag{2.13}$$

This $\mathbf{q} \to -\mathbf{q}$ inversion seems to indicate that if mechanical displacements are located on one side of the lattice, their self-stress counterparts are on the other side. The counting of the two are related via an equation analogous to Eq. (2.10):

$$n_{\text{zm}}(\mathbf{q}) - n_{\text{ss}}(-\mathbf{q}) = n_{\text{d.o.f}} - n_{\text{con}}, \tag{2.14}$$

where $n_{\text{zm}}(\mathbf{q})$ and $n_{\text{ss}}(\mathbf{q})$ are the respective number of zero modes and number of self-stresses evaluated at $\mathbf{q}$. In periodic Maxwell systems, $n_{\text{d.o.f}} = n_{\text{con}}$. Therefore, there must be as many zero modes as self-stresses at each wavenumber $-\mathbf{q}$. For example, you can always expect d translation modes occuring at $\mathbf{q} = 0$ and hence an equal number of self-stresses. One way to find the zeros of $\mathbf{R}(\mathbf{q})$ is to solve for the set of $\mathbf{q}$'s satisfying

$$\det[\mathbf{R}(\mathbf{q})] = 0, \tag{2.15}$$

which is doable only for isostatic systems, because the rigidity matrix is square. In Chapter 5, we'll offer a new method to find those zero-energy deformations in higher-order topological systems. The admissible wavenumbers must be compatible with periodicity of the system, in terms of both their real and imaginary parts.

So far, we've operated under a static framework, where one is focused on the deformation at a given time, regardless of the system's evolution in time. But in reality, dynamics are important. For example, when one stretches a horizontally oriented spring with no friction, one expects the masses to oscillate indefinitely, following a sine wave. The dynamics involved here rely on the energy of the system as a functional of the displacement vector, which results in forces. We then derive the equations of motion via the dynamical matrix, assuming the time dependence of each site's displacement carries a factor of $e^{i\omega t}$, where ω is the frequency of oscillations in time. Considering our spatially varying Bloch waves as well, we can deduce the normal modes per wave vector $\omega(\mathbf{q})$. Many topological studies, both in mechanics [3,63] and in other various physical systems [67] rely on the energetic band structure in order to derive the topological nature of the system. The number of bands is determined by the periodicity of the system and the number of sites per cell. For example, the one-dimensional Su-Schrieffer-Heeger (SSH) model of polyacetylene [68], described in Chapter 4 and Appendix B, possesses two bands from its dispersion relation. While we do not go into details here, one can show that a gap in the band structure is associated with the topological bulk-boundary correspondence of the SSH model. If the gap closes, the boundary modes disappear into the bulk.

2.2.4 Topological modes in isostatic systems

In 2014, Kane and Lubensky introduced their theory of topological states of matter in flexible mechanical materials. They used a counting argument to reveal the number of zero modes of the system. But importantly, they established a connection between the number of modes on the boundary region and the winding of the phase of the

rigidity map in Bloch basis over a full cycle of the Brillouin Zone [6]. This number is commonly referred to as the *winding number* and uses Cauchy's argument principle to indicate how many modes are enclosed by an integration of the phase of $\mathbf{R}(\mathbf{q})$ over the bulk. We've seen that we could find the zero-energy deformation in reciprocal space by solving for the null space of the rigidity map [Eq. (2.15)]. The determinant $\det\big[\mathbf{R}(\mathbf{q})\big]$ is a polynomial with no negative powers in $e^{i\mathbf{q}}$. Therefore, there are no poles to consider for:

$$\mathrm{WN}_i = \frac{1}{2\pi}\int_{\mathrm{BZ}} dq_i \frac{\partial}{\partial q_i}\Big[\arg\det\big(\mathbf{R}(\mathbf{q})\big)\Big]. \tag{2.16}$$

The winding number expressed here is *not* gauge invariant. Additionally, if we count cells from right to left, rather than from left to right, the winding number will return a different number of modes. In figure 2.4, we draw a contour in blue corresponding to the bulk modes, a contour which encloses the modes located on boundary 1. In the $\mathbf{z} = e^{i\mathbf{q}}$ wavenumber complex plane, these bulk modes have unit magnitude and enclose a region with modes $|z_i| < 1$, which correspond to deformations located along the "left edge" of the lattice. In that figure, we deform a fictitious system so that the zero mode moves from boundary 1 to boundary 2 (from situation A to C). In situation B, the winding number is precisely undefined and is characteristic of a zero mode located in the bulk (i.e. a translation mode).

How we define the cell is needed to find the polarization, but it has to be done reasonably. One could for example define the cell so that the constraints rather than being between a cell and its neighbor to the right, is between a cell and one — let's say — seven cells to the right. These two choices are equally valid, but not equally useful. Constructing the rigidity map $\mathbf{R}(\mathbf{z} = e^{i\mathbf{q}})$ in such careless way generates a finite Laurent series, that is, a series with negative powers of $\mathbf{z}$. Such powers are inconvenient to our methods, because we wish to count the number of zeros, whereas

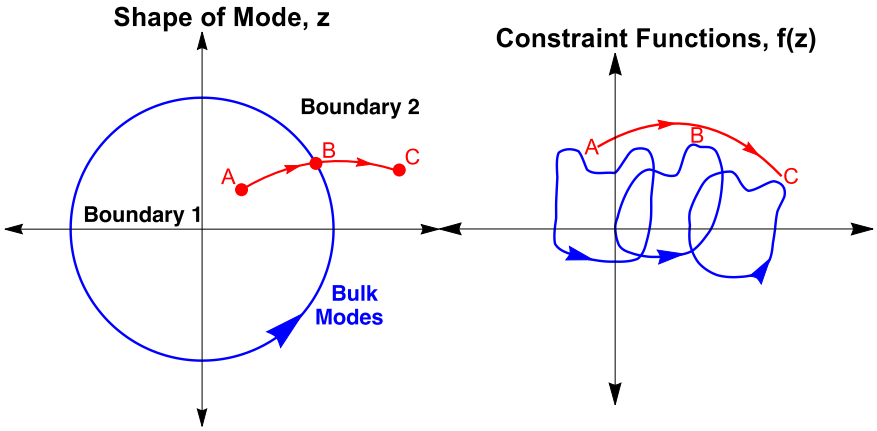

Figure 2.4: Mapping from the bulk modes to the image space of a linear constraint map, such as the rigidity matrix. On the left, the space of all modes $z = e^{iq}$ with the contour representing the bulk modes drawn in blue. On the right, what the mapping of the bulk mode looks like in image space for three scenarios: A, where the zero mode is within the contour and hence its mapping encloses the zero; C, where the mode is outside the contour and the mapping does not enclose the zero; and B, where the zero mode lies on the bulk itself.

the Argument Principle returns the difference between the number of zeros and the number of poles. Consequently, we adjust the definition of the unit cell such that the lowest power is non-negative. This is what we define as the "choice of gauge". Moreover, we choose a gauge that does not create additional spurious (non-physical) zeros at $\mathbf{z} = 0$. Therefore, we choose a unique gauge in which the lowest power of $\mathbf{z}$ is the constant $\mathbf{z}^0$, so that there are neither poles nor zeros at $\mathbf{z} = 0$. This choice for the unit cell is what we call the *minimal holomorphic gauge*. We make particular use of this property in our work to find the number of corner modes from the degree of a map, discussed in subsection 5.1.2.

In the same 2014 study [6], Kane and Lubensky mention the concept of polarization, denoted by a Bravais lattice vector. The winding number is only half the story to find such a polarization. One must compute the winding numbers on opposite edges to make a sense of the system's polarization. This polarization is then the difference between these two which results in exponentially localized edge modes. In Chapter 4, we investigate in detail a finite version of that polarization in open-boundary Maxwell

systems and in Chapter 3, we define a new invariant in the limit of long-wavelength modes which indicates the presence of edge modes immediately.

While edge modes are signatures of a non-trivial topological system, they require the open boundary conditions. When we solve $\mathbf{R}(\mathbf{q})\mathbf{u} = 0$, we ensure that the rigidity equations are met in the bulk, but our main concern is with modes that grow exponentially near the edge. Therefore, we must choose free boundary conditions so that the constraints that extend beyond the boundary are not present, while the displacement of the sites on the boundary still satisfy the bulk constraints. These boundaries need not be rectilinear: we could hypothetically define a boundary that is circular in shape, but this would pose an additional challenge to parametrize with our lattice model. When we solve for self-stresses from $\mathbf{Q}(\mathbf{q})\mathbf{e} = 0$, assuming we don't account for spring stiffnesses, we must instead set fixed boundary conditions, so that degrees of freedom on the boundary are not allowed to vary. In the Maxwell-Calladine counting of Eq. (2.10), this means we have an excess of constraints N_{con}, which ensures the presence of self-stresses. Additionally, fixed boundary conditions implies the sites are held at a fixed position, meaning there are no unbalanced forces on the boundary nor in the bulk, by definition of self-stresses.

2.2.5 Connection with other topological invariant and nonlinearities

In periodic systems, topology is observed via wall domains which separate two systems with different polarizations [6, 69]. Such interface phenomena are widely explored in other topological systems, such as backscattering suppressed edge waves in elastic and electronic media [70, 71]. These one-dimensional systems are characterized by another topological invariant: the Zak phase. The Zak phase is simply the integral of the Berry's phase over the Brillouin zone of 1D systems [67, 72]

$$\mathcal{Z} \equiv \frac{i}{2\pi} \oint_{\text{BZ}} dk \langle u(k) | \partial_k | u(k) \rangle, \tag{2.17}$$

and it is shown the integral evaluated here is a $\mathbb{Z}_2$ invariant.

More generally, the Berry's phase arises because of the ambiguity in defining the wave functions of a system. To briefly summarize it, the states $|u(k)\rangle$ can carry an additional phase in the form of $e^{i\phi(k)}$ and, hence, are not uniquely defined. An analogy can be drawn in electromagnetism where we can add curl-free components to the magnetic vector potential [67]. In principle, the Berry's phase is a geometric phase that is continuous and invariant under the choice of the additional phase: it is gauge-invariant. Additionally, when it is integrated over closing loops such as the Brillouin Zone of d dimensional systems where $d \geqslant 2$, the Berry's phase is then quantized and commonly referred to as the *Chern number*. The only difference with the expression written above, is that the Chern number arises from the integration of the Berry curvature. Such $\mathbb{Z}$ invariant is used in electronic systems to quantize the Hall conductance in topological insulators [47, 73]. In mechanical or circuit systems, the term "Chern number" is commonly used to describe unidirectional edge states [45, 53, 74]. A thorough classification of the nature of these topological invariants can be made depending on the dimensionality of the systems, the present symmetries and the homotopy group considered [75].

Finally, we'll close this section with a brief mention of nonlinearities. While we've so far only consider displacements that are small enough that the linear relation of Eq. (2.2) holds, we must certainly assess that it does not capture all possible ranges of motion in the metamaterials of interest. In particular, the SSH model for poly-acetylene, modeled via a 1D rotor chain is a perfect illustration that nonlinear effects can predict the formation of zero-energy solitary waves [76]. These waves are commonly referred to as solitons and their formation is related with the localized edge modes of the linear theory. If the system undergoes finite deformations, an edge mode turns into a domain wall inside the bulk, which separate two topologically different phases. Other nonlinear effects account for amplitude-dependent dispersions in simi-

lar chains that are corrected by higher-order analyses [77]. Others show that we can break the reciprocity symmetry in mechanical responses using suitable geometrical asymmetries [78].

2.3 Background for Continuum Theory

We now focus on the mechanics tailored to continuum systems. Similarly to discrete particles, we focus on the deformations occurring in an elastic body. In particular, we're interested in the relative displacement of a piece of material from its original position. We defined the strain as the change in displacement over space. If $u_j(\mathbf{r})$ is the j^{th} component of a continuous displacement field $\mathbf{u}$ evaluated at $\mathbf{r}$, then the strain ϵ_{ij} is its derivative with respect to the i^{th} component of $\mathbf{r}$:

$$\epsilon_{ij}(\mathbf{r}) = \frac{\partial u_j(\mathbf{r})}{\partial r_i} = \partial_i u_j(\mathbf{r}) \tag{2.18}$$

Since we're particularly focused on systems that not account for non-uniform rotations, we generally express our results in terms of the *symmetrized strain* instead $\epsilon_{ij} = 1/2(\partial_i u_j + \partial_j u_i)$ which is invariant under $i \leftrightarrow j$ inversion.

2.3.1 Stresses and forces

Similarly to strains being the continuum version of displacements in lattices, we now look to derive stresses in the context of continuum mechanics and draw an analogy with forces. We define the stresses σ_{ij} by using functional derivative on the energy of the system [79]

$$\sigma_{ij}(\mathbf{r}) = \frac{\delta E}{\delta \epsilon_{ij}(\mathbf{r})}. \tag{2.19}$$

But how do these stresses in fact relate to applied forces? In particular, what conditions do the stress fields need to satisfy so that we're in equilibrium on the boundary and in the bulk? We will invoke the chain rule of variational, which we quickly re-

derive for two arbitrary functions g, h, assuming g is scalar, while h is a vector. If g is a function of all h_i, which themselves are functions of variables x_j then:

$$\frac{\partial g}{\partial x_j} = \sum_i \frac{\partial g}{\partial h_i} \frac{\partial h_i}{\partial x_j}. \tag{2.20}$$

If we now treat the indices i, j as continuous variables $\mathbf{r}$ and $\mathbf{r}'$, then this becomes a functional relationship:

$$\frac{\delta g}{\delta x(\mathbf{r})} = \int d\mathbf{r}' \, \frac{\delta g}{\delta h(\mathbf{r}')} \frac{\delta h(\mathbf{r}')}{\delta x(\mathbf{r})}. \tag{2.21}$$

By using the force that the system exerts on the material at $\mathbf{r}$ as a functional derivative of the energy, we derive that

$$\begin{aligned}
f_j(\mathbf{r}) &= -\frac{\delta E}{\delta u_j(\mathbf{r})} && \text{(2.22a)} \\
&= -\int d\mathbf{r}' \, \frac{\delta E}{\delta \epsilon_{i_1 i_2}(\mathbf{r}')} \frac{\delta \epsilon_{i_1 i_2}(\mathbf{r}')}{\delta u_j(\mathbf{r})} && \text{(2.22b)} \\
&= -(1/2) \int d\mathbf{r}' \, \frac{\delta E}{\delta \epsilon_{i_1 i_2}(\mathbf{r}')} \Big(\left(\delta_{i_2 j} \partial_{i_1} + \delta_{i_1 j} \partial_{i_2}\right) \delta(\mathbf{r}' - \mathbf{r}) \Big) && \text{(2.22c)} \\
&= (1/2) \left(\partial_{i_1} \frac{\delta E}{\delta \epsilon_{i_1 j}(\mathbf{r})} + \partial_{i_2} \frac{\delta E}{\delta \epsilon_{j i_2}(\mathbf{r})} \right) && \text{(2.22d)} \\
&= \partial_i \frac{\delta E}{\delta \epsilon_{ij}(\mathbf{r})} && \text{(2.22e)}
\end{aligned}$$

where the relationship between strains and displacement used in Eq. (2.22c) is derived directly from the definition for symmetrized strain. We also note that a lot of these notations use Einstein summation convention. Hence, we see that given our definition of stress as the functional derivative of the energy with respect to strain, we find that

$$f_j(\mathbf{r}) = \partial_i \sigma_{ij}(\mathbf{r}). \tag{2.23}$$

In equilibrium, the force density $\mathbf{f}$ is equal to zero, so we recover that the stress

tensor's gradient must vanish in the bulk $\partial_i \sigma_{ij} = 0$.

What about the boundary? Let us suppose that there are no body forces and that forces are exerted only within a thin boundary layer of thickness w. Then, by integrating the equilibrium condition across the boundary, we can turn the contribution of spatially varying forces $\partial_i \sigma_{ij} + f_j$ into surface terms

$$n_i \sigma_{ij} = f_j^b, \tag{2.24}$$

where $\mathbf{n}$ is the normal to the surface and f_j^b is the force per area on the boundary. Moreover, within the volume across the boundary layer, the equilibrium condition would simplify into

$$\partial_i \sigma_{ij} = f_j^b / w. \tag{2.25}$$

These two last equations show that we can impose conditions on the stress tensor and its gradients coming from the supplied force and the thickness of the boundary in order to achieve mechanical equilibrium.

2.3.2 The rigidity and equilibrium maps in the continuum

We draw mappings between the strain and stress fields and the discrete springs which make for the energetic constraint of the system, which we'll use extensively in Chapter 3. The analogy with the lattice definitions is clear. Let $R_{m,ij}$ the component of the rigidity which maps from the i, j components of the strain to the m^{th} bond extension. Define $Q_{ij,m}$ as the map from the spring extensions to the i, j components of the stress; then using Einstein's notation:

$$e_m(\mathbf{r}) = R_{m,ij}(\mathbf{r})\, \epsilon_{ij}(\mathbf{r}) \tag{2.26}$$

$$\sigma_{ij}(\mathbf{r}) = Q_{ij,m}(\mathbf{r})\, e_m(\mathbf{r}). \tag{2.27}$$

We'll see in that there exist two version for the mappings, one pre-relaxation and one post-relaxation. This analysis can be made on either. The total energy of the system is

$$E = \frac{1}{2}\int d\mathbf{r} e_m^2(\mathbf{r}) = \frac{1}{2}\int d\mathbf{r}\big(R_{m,ij}\epsilon_{ij}(\mathbf{r})\big)^2. \tag{2.28}$$

We look to derive the relationship between rigidity and equilibrium maps

$$\sigma_{ij}(\mathbf{r}) = \frac{\delta E}{\delta \epsilon_{ij}(\mathbf{r})} \tag{2.29a}$$

$$= \frac{\delta}{\delta \epsilon_{ij}(\mathbf{r})}\frac{1}{2}\int d\mathbf{r}\big(R_{m,ij}\epsilon_{ij}(\mathbf{r})\big)^2 \tag{2.29b}$$

$$= R_{m,ij}\, R_{m,ij}\epsilon_{ij}(\mathbf{r}). \tag{2.29c}$$

This implies that

$$\sigma_{ij}(\mathbf{r}) = R_{m,ij}\, e_m(\mathbf{r}), \tag{2.30}$$

where in the final line, we used the linear relationship of Eq. (2.26). From Eq. (2.27) we recognize the equilibrium mapping $Q_{ij,m}$, meaning $Q_{ij,m} = R_{m,ij}$.

2.3.3 In reciprocal space

Her, we move to reciprocal space and look to re-derive the same relationship as Eq. (2.13). In particular, the key sign inversion permits for topological polarization and indicates that zero modes are coupled with self-stresses on opposite ends of a Maxwell system. To that end, we consider the most general, nonlocal classes of rigidity and equilibrium maps:

$$e_m(\mathbf{r}) = \int d\mathbf{r}' R_{m,ij}(\mathbf{r},\mathbf{r}',\partial')\epsilon_{ij}(\mathbf{r}'), \tag{2.31}$$

$$\sigma_{ij}(\mathbf{r}) = \int d\mathbf{r}' Q_{ij,m}(\mathbf{r},\mathbf{r}',\partial')e_m(\mathbf{r}'). \tag{2.32}$$

where the inclusion of "∂" indicates that the maps can involve gradients of their respective domain variables. We once again use the stress-energy functional relationship and start with gradients of the delta functional

$$
\begin{aligned}
Q_{ij,m}(\mathbf{r},\mathbf{r}',\partial') &= \frac{\delta\sigma_{ij}(\mathbf{r})}{\delta e_m(\mathbf{r}')} && \text{(2.33a)}\\
&= \frac{\delta^2 E}{\delta\epsilon_{ij}(\mathbf{r})\,\delta e_m(\mathbf{r}')}. && \text{(2.33b)}\\
&= \frac{\delta}{\delta\epsilon_{ij}(\mathbf{r})}\left(\frac{\delta E}{\delta e_m(\mathbf{r}')}\right) && \text{(2.33c)}\\
&= \frac{\delta}{\delta\epsilon_{ij}(\mathbf{r})}\, e_m(\mathbf{r}') && \text{(2.33d)}\\
&= \frac{\delta}{\delta\epsilon_{ij}(\mathbf{r})}\int d\mathbf{r}'' R_{m,ij}(\mathbf{r}',\mathbf{r}'',\partial'')\epsilon_{ij}(\mathbf{r}'') && \text{(2.33e)}\\
&= \int d\mathbf{r}'' R_{m,ij}(\mathbf{r}',\mathbf{r}'',\partial'')\delta(\mathbf{r}''-\mathbf{r}), && \text{(2.33f)}
\end{aligned}
$$

where in the last steps, we used integration by parts. This leads to the desired result:

$$Q_{ij,m}(\mathbf{r},\mathbf{r}',\partial') = R_{m,ij}(\mathbf{r}',\mathbf{r},-\partial), \tag{2.34}$$

which shows that the functional differentiation flips the sign of the derivatives.

Finally, by accounting for the system's translational invariance and the local interactions the rigidity map term can be written using a delta function:

$$R_{m,ij}(\mathbf{r},\mathbf{r}',\partial) = \delta(\mathbf{r}-\mathbf{r}')R_{m,ij}(\partial). \tag{2.35}$$

Moreover, in wavenumber space, the derivatives turn into products with the wavenumber, $\partial \to i\mathbf{q}$, so that

$$Q_{ij,m}(\mathbf{q}) = R_{m,ij}(-\mathbf{q}). \tag{2.36}$$

Our linear maps then have the form:

$$e_m(\mathbf{q}) = R_{m,ij}(\mathbf{q})\epsilon_{ij}(\mathbf{q}), \tag{2.37}$$

$$\sigma_{ij}(\mathbf{q}) = Q_{ij,m}(\mathbf{q})e_m(\mathbf{q}). \tag{2.38}$$

Chapter 3
CONTINUUM LIMIT OF MECHANICAL METAMATERIALS

This chapter heavily focuses on our PRX publication: *Topological Elasticity in Flexible Materials* [33].

3.1 Introduction

We have previously established a framework for discrete mechanical lattices. We now look to develop a novel micromorphic continuum elastic theory, one that provides far richer mechanical response than with conventional Cauchy elasticity. Cauchy's elasticity relies on strain and stress relationship over infinitesimally small regions, but the goal here is to derive a continuum theory that extends the microscopic lattice structure in the long-wavelength regime and that retains the topological boundary effects seen across the entire macroscopic system. Eventually, we aim to build such a theory without the need for a microstructure to rely on, even in our context its presence is necessary to break the spatial inversion symmetry. The main concept in either scenario is to use an energetic cost that is based on the gradients of a input function — in the elastic case, that is the strain field — and to build from it a system that is topological in nature. Like in the 2014 work of Kane and Lubensky [6], we're interested in topologically protected boundary modes, reminiscent of electronic conducting states on the boundary, in the integer quantum Hall effect. Recent work has shown that these surface modes can be generated in systems that lack periodicity such as quasicrystals [80] and in those that are distributed from a random point sets [2].

The main issue we face by extending the work done in lattice theory is the topo-

logical nature of the discrete systems relies on the existence of a Brillouin Zone, upon which the winding number is calculated. We no longer have such tool in the long-wavelength limit. Nevertheless, we use this to our advantage and introduce a new topological invariant which measures the *difference* between the number of zero modes on opposite edges, which is more indicative of a topological polarization. The only similarity with the lattice theory is that we're still focused on systems at the point of critical mechanical stability. We will prove that the energetic costs of the system which break spatial inversion symmetry result from the gradients of the strains and their existence is necessary in order to observe modes localized on only one side.

The remainder of this chapter is organized as follows: in section 3.2, we demonstrate the coupling between macroscopic strains, the microscopic degrees of freedom and the energetic costs of the microstructure. In section 3.3, we break down the total energy into a bulk term and a surface term, and show that the latter is a signature of the topological state. We do so in even greater details for a system in one dimension (section 3.4). In section 3.5, we explain the process of relaxation via a linear model involving states of self-stress, which results in an effective theory of smooth strains only. In section 3.6 we introduce our new topological invariant evaluated in the long-wavelength limit. Finally, we discuss the length scales associated with our surface modes (section 3.7), followed by a brief conclusion section (section 3.8).

3.2 Effects of smooth strain field on microstructure

We now explore how the strain field affects a microstructure, in particular the extensions of the springs which directly relate to the energy cost stored in such system. The model studied is identical to that of a lattice of sites connected by bonds. Let $\mathbf{u}(\mathbf{r})$ be the displacements of the sites of a cell positioned at $\mathbf{r}$, $\mathbf{p}$ be the position of the center of the bond relative to the center of cell and $\mathbf{b}$ be the direction of the bond connecting two sites, as shown in figure 3.1. Assuming the fields are "sufficiently

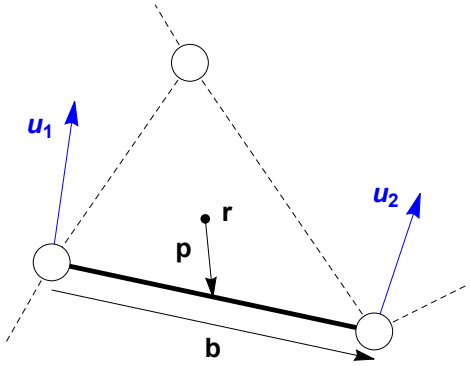

Figure 3.1: A periodic microstructure composed of bonds connecting sites, drawn from a Kagome lattice system. The bond located at $\mathbf{p}$ relative to the center $\mathbf{r}$ of the cell in which it lies, connects two sites with relative position $\mathbf{b}$. These sites undergo displacements $\mathbf{u}_1(\mathbf{r}), \mathbf{u}_2(\mathbf{r})$, which cause the spring to extend / compress.

smooth", meaning they change very little over the length scale of a bond, we can do a Taylor expansion over the displacement vector to find the bond's extension e:

$$e = \frac{1}{|\mathbf{b}|}\mathbf{b} \cdot [\mathbf{u}(\mathbf{r}+\mathbf{p}+\mathbf{b}/2) - \mathbf{u}(\mathbf{r}+\mathbf{p}-\mathbf{b}/2)] \tag{3.1a}$$

$$\approx \frac{b_i b_j}{|\mathbf{b}|}\left[1 + p_k\partial_k\right]\partial_i u_j \tag{3.1b}$$

$$= \frac{b_i b_j}{|\mathbf{b}|}\left[1 + p_k\partial_k\right]\epsilon_{ij}. \tag{3.1c}$$

We go in details over this Taylor expansion in Appendix A.1. In general, strains gradients are ignored because of their relatively small contributions compared to the 0^{th} order, more conventional elastic terms; however, at the point of critical stability, those may vanish. While the 1^{st} order terms may be leading after all, higher-order terms need not to be included in our derivation for their very little contributions. We notice that the expression for e is rotationally invariant (it is invariant under inversion of the indices i and j), therefore, we only need to account for the symmetrized strains $\epsilon_{ij} \equiv (1/2)(\partial_i u_j + \partial_j u_i)$. From now, we'll base our reasoning entirely on them. Finally, it is worth noting that the microstructure itself, i.e. the position of the bonds $\mathbf{p}$ and their orientations $\mathbf{b}$ still does play a critical role in the final expression of the

extension. Does the choice of gauge has an effect on our physics? If we were to define the microcell differently, let's say by assigning one of the bonds to an adjacent cell, the associated $\mathbf{p}$ will be shifted by a combination of lattice vectors. Meanwhile though, the position at which we evaluate the strain would undergo an equal and opposite shift, such that the observables remain invariant.

Based off Eq. (3.1c), we now define the *initial rigidity map* $\mathbf{R}^0$ as follow. It maps from dimensionless strains to springs' extensions that have units of length:

$$e_m(\mathbf{r}) = R^0_{m,ij}\epsilon_{ij}(\mathbf{r}) \tag{3.2}$$

$$R^0_{m,ij} \equiv \frac{b^m_i b^m_j}{|\mathbf{b}^m|}\left[1 + p^m_k \partial_k\right]. \tag{3.3}$$

$\mathbf{R}^0$ is the continuum analog of the rigidity matrix used in lattice theories [3, 6]. Nevertheless, note that it carries the superscript 0 and the term "initial". In fact, springs extensions in the image space of $\mathbf{R}^0$ usually result in unbalanced forces on the sites of the cell, which is why we'll introduce a version of the rigidity that accounts for relaxation in section 3.5.

Clearly, our objective is to determine the shape of the zero-energy strain fields. We know this field, whether it takes form as strains or as displacements, exist in isostatic 2D lattices and it is commonly referred as the Guest mode [81]. The zero-energy deformations appear as combinations of zero-energy strains that lie in the eigenspace of the elasticity tensor. As it is shown in Ref. [81], the mode extends linearly and as a result, every Maxwell lattices necessarily has multiple zero-energy configurations. So far, we've considered only one configuration (figure 3.1) but we could show that a change in configuration alters the topological polarization [82]. We will do so in section 3.6.

3.3 Bulk and Surface Energies

In the preceding section, we derived the linear relationship between strains and the mechanical constraints of the microstructure. In fact, those constraints are related with the total energetic cost of the system: the more the springs are stretched / compressed, the more energy it costs to the system. While our goal is to minimize (and possibly nullify) this energetic cost, we must explore what is its relationship with the strains. For simplicity, we assume that the springs of the microstructure have unit magnitude stiffness and hence, the resultant energy integrated across the whole system is

$$E = \frac{1}{2}\int d^d\mathbf{r}\, e_m(\mathbf{r})e_m(\mathbf{r}). \tag{3.4}$$

Using the linear relationship between strains and extensions [(Eq. (3.1c)], we can manipulate this total energy (see Appendix A.2) to break it down into two terms: a bulk and a surface contributions. The bulk energy accounts for the conventional strains (that lead to conventional elasticities [3]) and the product of two gradient terms, which are both symmetric under spatial invariance

$$E_b = \frac{1}{2}\int d^d\mathbf{r}\, A_{ijkl}\epsilon_{ij}\epsilon_{kl} + D^{\alpha\beta}_{ijkl}(\partial_\alpha\epsilon_{ij})\,(\partial_\beta\epsilon_{kl}), \tag{3.5a}$$

$$A_{ijkl} \equiv \sum_m \frac{b^m_i b^m_j b^m_k b^m_l}{|\mathbf{b}^m|^2}, \tag{3.5b}$$

$$D^{\alpha\beta}_{ijkl} \equiv \sum_m \frac{b^m_i b^m_j b^m_k b^m_l}{|\mathbf{b}^m|^2} p^\alpha_m p^\beta_m. \tag{3.5c}$$

These terms are not as significant in our theory since they cannot carry topological signature. However, the other energetic contribution includes a product of a strain and of strain gradients, which in fact break spatial inversion symmetry. Following our work done in Appendix A.2, we're able to turn the energy expressed in the bulk

in Eq. (3.4) into a surface term using the divergence theorem:

$$E_s = \frac{1}{2}\int_{\text{surface}} d^{d-1}\mathbf{r}\,\mathbf{n}_\alpha B^\alpha_{ijkl}\epsilon_{ij}\epsilon_{kl}, \tag{3.6a}$$

$$B^\alpha_{ijkl} \equiv \sum_m \frac{b^m_i b^m_j b^m_k b^m_l}{|\mathbf{b}^m|^2} p^\alpha_m. \tag{3.6b}$$

where $\mathbf{n}$ is the outward-facing surface normal. $A_{ijkl}, B^\alpha_{ijkl}$ and $D^{\alpha\beta}_{ijkl}$ are all elastic moduli that can be numerically evaluated for a particular configuration of the microstructure (which we do in table A.1 for the system drawn in figure 3.2). While the bulk energetic terms are necessarily positive [from the looks of Eq. (3.5a)], the surface terms can break inversion symmetry, and hence, the surface energies may either be positive or negative.

3.4 Equilibrium in One-Dimensional Systems

To illustrate how the surface energetic terms are signature of topological polarization, we consider the simpler one-dimensional system SSH rotor chain that we've mentioned in Chapters 2 and will mention in 4 [6] which offers the advantage of not worrying about multiple degrees of freedom. While we'll see that this 1D system carries a topological and a translational zero-energy edge modes, we re-write the constraint equation to be more symmetric in form. For such 1D rotor chain, the constraint of the n^{th} spring e_n is related with the rotation of the adjacent rotors $\{u_n\}$ (commonly referred as displacements) via

$$e_n = au_{n+1} - (a+b)u_n + bu_{n-1}. \tag{3.7}$$

We work the direct solution of this equation when written in the context of rigidity mapping and in reciprocal space in Appendix A.3. We prove that the two accepted

zero-energy displacement modes are:

$$u_n = u_0 \text{ (uniform mode) and } u_n = u_0(b/a)^n. \tag{3.8}$$

The second displacement solution indicates the strains take the form $u_{n+1} - u_n \sim (b/a)^n$ which is valid in the long-wavelength limit if $\log|b/a| \ll 1$. Define now l as the spacing of the cells and d as the length of the open-bounded chain (a necessary condition to see a growing / shrinking mode). We conduct a Taylor expansion on the displacements which allows us to re-write the extension of the springs:

$$u_{n\pm1} = u_n \pm l u_n' + (1/2) l^2 u_n'' \tag{3.9}$$

$$\implies e_n = l(a-b)u_n' + (1/2)l^2(a+b)u_n'' \tag{3.10}$$

We then turn the energy into functional form by using Eq. (3.4):

$$E = \frac{l}{2}\int dx\,[(a-b)u'(x) + l/2\,(a+b)u''(x)]^2\,, \tag{3.11a}$$

$$= \frac{k}{2}\int dx\,[u'(x) - \alpha u''(x)]^2\,, \tag{3.11b}$$

$$= \frac{k}{2}\left[-\alpha(u')^2\Big|_{-d/2}^{d/2} + \int dx\,\left(u'(x)^2 + \alpha^2 u''(x)^2\right)\right], \tag{3.11c}$$

where the new *macroscopic* parameters k, α are defined in terms of the *microscopic* constants a, b:

$$k = l(a-b)^2 \text{ and } \alpha = \frac{l}{2}\frac{a+b}{b-a}. \tag{3.12}$$

This is the linear limit of the nonlinear edge mode that was found to extend into a soliton in Ref. [76], which we prove in Appendix A.3. From now, we will consider the case where $b > a \iff \alpha > 0$, where we know a right edge mode exists, given the form of the displacement field. In appearance, Eq. (3.11c) confirms our unproven claim: if

a mode considered is in fact a zero-energy mode, the surface term must be negative, given that the bulk term is always positive. This stipulates that $u'(d/2) > u'(-d/2)$, a signature of a right edge mode. We now look to rigorously prove that the surface energy does in fact indicate where the edge mode is.

From the energy functional, we can derive the force balance modes in the bulk by operating a derivative of E with respect to $u(x)$. Such modes must satisfy constraint on their second derivatives, which in turn provide a general profile for the displacement themselves:

$$(\alpha^2\partial^2 - 1)u''(x) = 0 \tag{3.13}$$

$$\implies u(x) = c_- e^{-(x+d/2)/\alpha} + c_+ e^{(x-d/2)/\alpha} + \epsilon_0 x + u_0. \tag{3.14}$$

Therefore, the general equilibrium profile consists of two boundary modes, a uniform strain (ϵ_0) and a trivial translation (u_0). With our assumption of a positive α, the first mode is exponentially localized to the left edge and it has amplitude c_- at $x = -d/2$. The second mode is exponentially localized to the right edge, with amplitude c_+ at $x = +d/2$. We can plug the value of the mode [Eq. (3.14)] into the energy functional of Eq. (3.11) and use the large system size limit

$$E = \frac{k}{2}\left[\frac{2c_-^2}{\alpha} - 4c_-\epsilon_0 + d\epsilon_0^2\right]. \tag{3.15}$$

What's important to notice here is that the energy functional solely depend on the bulk strain ϵ_0 and the c_- mode. How does that indicate which profiles of Eq. (3.14) is the zero mode and which ones must vanish? Well clearly, if we want the energy to be zero, c_- and the uniform strain ϵ_0 must both be zero, while there is no constraint on c_+ or u_0. This remarkable trick allows us to assert that we in fact deal with a right edge mode (possibly with a translational contribution) which is compatible with our initial condition $\alpha > 0$. A similar reasoning can be made for $\alpha < 0$ of course.

For non-Maxwell systems, for example those that are over-constraint, this continuum energetic theory could have a surface term but no zero-energy modes.

3.5 Relaxation and Equilibrium in the Microstructure

So far, we have not made any assumptions on mechanical equilibrium. From the energy functional of Eq. (3.4), we derive the stress tensor $\sigma_{ij}(\mathbf{r})$ [Eq. (2.19)] and claim that we reach conventional elastic balance — i.e. $\partial_i \sigma_{ij} = 0$ in the bulk — as proven in section 2.3. Problem: we still have unbalanced forces on each of the sites of our microstructure, as shown in figure 3.2 (a). Our solution: we look for a mechanism of relaxation which will preserve the long range behavior of the strains on the system's energy, while re-arranging the sites within each cell to minimize it. We do so by involving the initial equilibrium map $Q^0_{ij,m}$ which maps from bonds' extensions to stresses:

$$\sigma_{ij}(\mathbf{r}) = Q^0_{ij,m} e_m(\mathbf{r}), \tag{3.16}$$

$$Q^0_{ij,m} \equiv \frac{b_i^m b_j^m}{|\mathbf{b}|} \left[1 - p_k \partial_k\right]. \tag{3.17}$$

In reciprocal space, the derivative terms ∂_k turn into iq_k. Per usual, we still consider strains and stresses that follow Bloch wave's form $\exp(i\mathbf{q}\cdot\mathbf{r})$ and confirm the relationship between the equilibrium and rigidity maps in wavenumber space of Eq. (2.36):

$$Q^0_{ij,m}(\mathbf{q}) = R^0_{m,ij}(-\mathbf{q}). \tag{3.18}$$

Let's explore what truly occurs when a set of strains are imposed to the system and affect the microstructure as described in Eq. (3.1c):

1. the strains result in sets of extensions (compressions) of the springs,

2. those cause the tensions in the bonds to change,

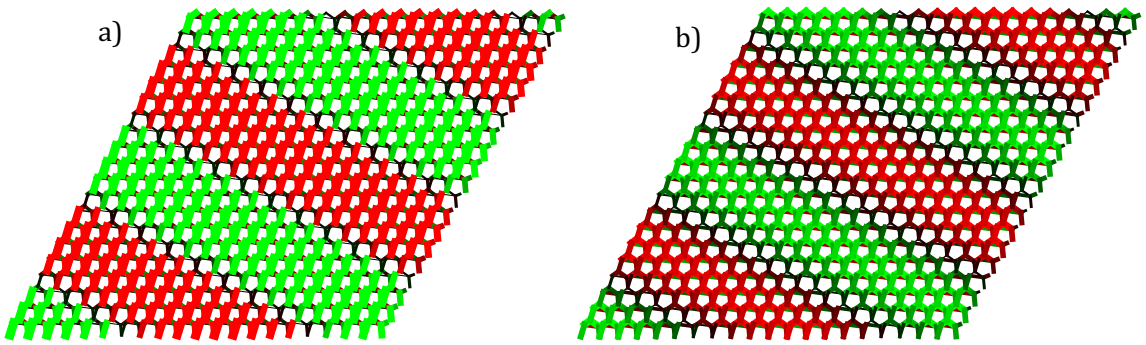

Figure 3.2: (a) On a periodic system, we apply a particular strain $\epsilon_{ij}(\mathbf{r}) = (\epsilon_{xx}, \epsilon_{yy})e^{i(\mathbf{q}\cdot\mathbf{r})}$. This causes bonds to stretch (green) or compress (red). (b) The system then relaxes by projecting onto space of self-stresses that mostly capture particles displacing over short distances but reducing the energy cost overall.

3. which in return generate forces on the sites.

Such a system can't be left in such non-equilibrium state; its sites will re-arrange to minimize the energy and eventually reach force balance. We could account for those displacements using the simple dynamics of Newton 2$^{\text{nd}}$ law, but that is such a computationally heavy method, and to be fair, a pretty boring one. Instead, we offer a more elegant approach which consists of capturing the states of self-stress of the system, those sets of extensions that result in no force on the sites and that lie in the null space of the equilibrium map [6, 64]. As shown in Ref. [63], the new set of extensions — those in the *post-relaxation* state — are given by the projection of the pre-relaxation extensions onto the space spanned by the orthonormal basis of self-stresses.

We note that for the systems we consider, the condition of critical stability offers d modes of translation (corresponding to the number of dimensions) and d states of self-stresses [per Maxwell-Calladine of Eq. (2.10)]. We also note that the elastic tensor possesses $d(d-1)/2$ components, which means there are $d(d-1)/2$ strains that cost no energy. These are in fact the Guest modes [81].

So why can't we simply project our extensions into the space of the two self-stresses (for a 2D system) and simply be done with it? Well, if we did so, we wouldn't perceive

the long range topological effects that we're looking to unfold via our continuum theory. In particular, we want the center of mass of each cell to couple with the external fields over *long distances* even if they dramatically change *within* the cell. To this end, we let the unit cell relax and reach equilibrium, so that the energetics only depend on the slowly-varying strain fields, those that spread over distances much larger than the size of the cell and that are described by Bloch's theorem $\boldsymbol{\epsilon}(\mathbf{r}) = \boldsymbol{\epsilon} \exp(i\mathbf{q} \cdot \mathbf{r})$.

Our solution is as follow: by imposing a set of d external center-of-mass displacements $\{\mathbf{v}_i\}$ on each of the sites of the cell, we're able to generate no center-of-mass forces. Those imposed displacements take form in translations of all sites along the x and y directions and with spatial dependence $\exp(i\mathbf{q} \cdot \mathbf{r})$. That way, the projection of the resulting forces onto the imposed displacements is non-zero

$$\langle v_i | f \rangle \neq 0 \text{ for all } i \in \{1, 2, ..., d\}. \tag{3.19}$$

Meanwhile, this relaxation mechanism allows for the other components of the forces to vanish within the cell. In the end, by letting the cell itself relax, we allow forces on the smooth and slowly-varying strain fields to remain unbalanced generically speaking. The new imposed displacements $\{\mathbf{v}_i\}$ take form by projecting them from the initial equilibrium matrix $\mathbf{Q}^0$. Our new self-stresses and the set of bond extensions post-relaxation are then given by:

$$\{|s_j\rangle\} = \text{Null}\Big[(\mathbb{1} - |v_i\rangle\langle v_i|)\mathbf{Q}^0\Big] \tag{3.20}$$

$$e_{\text{post}} = \sum_j |s_j\rangle\langle s_j|e_{\text{pre}}\rangle, \tag{3.21}$$

assuming $\{\mathbf{s}_j\}$ still forms an orthonormal basis. One could question if we always have the proper of amount of $\{\mathbf{v}_i\}$. In fact, for periodic systems, the modes at

different wave vector $\mathbf{q}$ are orthogonal. And as we've shown in Eq. (2.37), rigidity and equilibrium maps, strain and stress fields are all evaluated at the same $\mathbf{q}$ wave vector. Consequently, there are always d modes $\{\mathbf{v}_i\}$ that need be projected out of the equilibrium map.

The result: a new *rigidity map* $R_{m,ij}$, which describes the springs' extensions from a smooth strain field, following short-distance relaxations within the unit cell. We draw what such relaxation looks like on figure 3.2 (b). Similarly, we can derive the new *equilibrium map*. Both these new maps account for the self-stresses defined in Eq. (3.20):

$$R_{m,ij}(\mathbf{q}) = s^*_{m,n} R^0_{n,ij}(\mathbf{q}), \tag{3.22}$$

$$Q_{ij,m}(\mathbf{q}) = Q^0_{ij,n}(\mathbf{q}) s_{m,n}. \tag{3.23}$$

The above analysis implies that the rigidity map is a square matrix that acts on d independent components of the strain and returns d energetic contributions post-relaxation, using the d states of self-stress. While it isn't the same Maxwell condition than the lattice model (which truly connected number of sites with number of bonds) it still accounts for degrees of freedom (the strain components) and energetic constraints.

3.6 Topological polarization in the continuum

So far, we've generated a mathematical tool that maps from the independent components of the strain, returns energetic contribution and which holds the Maxwell criterion. However, we have not yet proven that such map captures bulk-boundary correspondence, manifested via edge modes, ones that we've mentioned in subsection 2.2.4. The difficulty here is we reason in the long-wavelength limit and there is no Brillouin Zone anymore. So how do we formulate a topological invariant that directs the presence of edge modes? For recall, these modes are found in wavenumber

space. For a system defined in Cartesian coordinates, the position vector is simply $\mathbf{r} = (r_x, r_y)$ while the wave vector has form $\mathbf{q} = (q_x, q_y)$. If the strains follow Bloch's theorem, i.e. they include an exponential term of the form $\exp[i(q_x r_x + q_y r_y)]$, then the left or right edge modes are identified by the imaginary part of q_x: if $\mathrm{Im}(q_x) < 0 \implies$ left edge mode and vice-versa.

For recall Eq. (2.15) states that zero-energy modes are given by the sets of wave vectors for which the determinant of the rigidity map of Eq. (3.22) vanishes. Therefore, we solve for the zeroes of $\det(\mathbf{R}(\mathbf{q}))$ which is an analytical function of q_x and q_y. Since $\det(\mathbf{R}(\mathbf{q}))$ has a double zero at $\mathbf{q} = 0$, it takes on the following form

$$\mathbf{R}(\mathbf{q}) = \begin{pmatrix} R_{11}(\mathbf{q}) & R_{12}(\mathbf{q}) \\ R_{21}(\mathbf{q}) & R_{22}(\mathbf{q}) \end{pmatrix} \tag{3.24a}$$

$$\implies \det(\mathbf{R}(\mathbf{q})) = A_{2,0}q_x^2 + A_{1,1}q_x q_y + A_{0,2}q_y^2 + iA_{3,0}q_x^3 + iA_{2,1}q_x^2 q_y + \ldots, \tag{3.24b}$$

where $A_{n_1 n_2}$ real coefficients set by the microstructure. As we set ourselves in the long-wavelength limit, we can stop the expansion at a degree n, in this case $n = 3$ which indicates there are 3 solutions as well. Of these, two take the form

$$q_x = \alpha_\pm q_y + i\beta_\pm q_y^2, \tag{3.25}$$

while the other is a short-wavelength mode of order q_y^0. We solve "x" as a function of "y" since we're interested in the value of zero modes along the x direction against the value along the transverse direction y. The α's are determined by the coefficients of order $O(q^2)$, i.e. $A_{1,1}, A_{2,0}, A_{0,2}$, while the β's depend on the second and third order terms of Eq. (3.24b). We also define the inverse decay length $\kappa_\pm \equiv \beta_\pm q_y^2$ which we use in procedure of section 4.1 to quantify the value of polarization in finite lattices. Despite being solutions to the mathematical equation of Eq. (3.24b), the short-wavelength modes are not permitted by our continuum formulation; they are

non-physical in nature. Our interest is rather on the long-wavelength edge modes and as we notice they come in pair: if the two imaginary parts of q_x, which are determined by $\kappa_\pm$, have opposite signs, the system is deemed to be trivial, topologically speaking. Therefore, in order to observe an actual left or right edge mode, the inverse decay lengths must be of the same sign.

3.6.1 Definition of the new invariant

Since we no longer have use of a Brillouin Zone, we must think of a different approach to compute the number of zero modes. Other topological research on continuum systems, such as flocking [44] or topological sound [43] use different approaches to compute the Chern number. An immediate suggestion would be to perform an integral over the complete real line, one that includes all real numbers joined with the infinities $\mathbb{R} \cup \{\pm\infty\}$ but this would still account for fictitious, non-physical zero modes.

Let's set $\mathbf{l}_1$ as the lattice spacing of our microstructure (in reality, we're interested in using a dimension of length to keep our quantities dimensionless when needed). Our goal is to capture short-wavenumber zero modes only. These zero modes are given by Eq. (3.25) and have

$$\mathrm{Re}(q_x) \approx q_y \text{ and } \mathrm{Im}(q_x) \approx q_y^2. \tag{3.26}$$

Our method therefore consists of designing an integral path over the bulk modes (over $\mathrm{Re}(q_x)$) that is sufficiently large to account for long-wavelength zero modes and yet sufficiently small to reject the fictitious, undesirable short ones:

$$\text{size of zeros of interest} \ll \text{limits of bulk contour} \ll \text{size of unwanted zeros.} \tag{3.27}$$

This suggests that the transverse component to the x direction of the wave-vector

must be small as well: $q_y|\mathbf{l}_1| \ll 1$. Then Eq. (3.27) implies

$$q_y|\mathbf{l}_1| \ll q_x|\mathbf{l}_1| \ll 1, \tag{3.28}$$

where the first term of the inequality refers to the zero modes themselves, while the second is the limit of integration over the bulk modes. By setting the dimensionless quantity $\epsilon \equiv q_y|\mathbf{l}_1|$, one possible choice for the limits of integration that satisfies Eq. (3.28) can then be

$$\epsilon^{1/2}/|\mathbf{l}_1| \leqslant q_x \leqslant \epsilon^{1/2}/|\mathbf{l}_1|, \tag{3.29}$$

clearly because $\epsilon \ll \epsilon^{1/2} \ll 1$. In Appendix A.4, we show that a change of the exponent of ϵ affects the precision of capture of the modes of interest. Nonetheless, for this particular choice, the resulting topological invariant describing the numbers of modes on the left edge minus those on the right is:

$$N_L - N_R = \frac{1}{\pi} \lim_{\epsilon \to 0^+} \int_{-\sqrt{\epsilon}/|\mathbf{l}_1|}^{\sqrt{\epsilon}/|\mathbf{l}_1|} dq_x \, \frac{\partial}{\partial q_x} \Big[\arg \det \big(\mathbf{R}(q_x, q_y = \epsilon/|\mathbf{l}_1|) \big) \Big]. \tag{3.30}$$

This equation states the difference of number of modes on the edges is given by how the relationship between strains and extensions [encoded in $\det(\mathbf{R}(\mathbf{q}))$] varies for a range of wavenumbers $\mathbf{q}$ in the bulk, reflecting the topological bulk-boundary correspondence we were looking for. Importantly enough, this winding number links two opposite boundaries at once, unlike its lattice theory counterpart. We briefly explain how this equation is valid, given the limits of our integral and the nature of the zero modes.

In reality, we technically integrate over the contour drawn on figure 3.3, which includes both solid and dashed line. By the Argument Principle, and since $\det \mathbf{R}(\mathbf{q})$ is a function with no poles, the integral will return the number of zero modes within

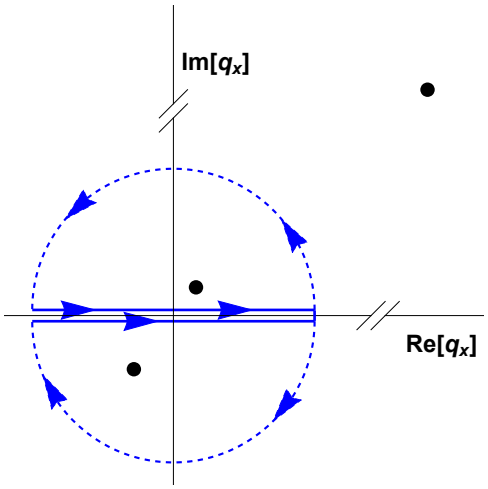

Figure 3.3: The contour used to establish the relationship between bulk structure and zero modes. In the complex plane of q_x, the contour starts at $+\epsilon/|\mathbf{l}_1|$ goes counter-clockwise over the upper arc (dashed), then over the upper real part (solid) from left to right, then clockwise over the lower arc (dashed), and finally over the lower real part (from left to right) to come back to its starting point. As explained in the text, the two dashed portions cancel out and the difference between modes with positive and negative imaginary parts is given by the solid lines only.

the contour. Immediately, we see that the short-wavelength modes are excluded from that contour. Moreover, since the zero modes have the following property — $\mathrm{Re}(q_x) \approx q_y = \epsilon/|\mathbf{l}_1|$ and $\mathrm{Im}(q_x) \approx q_y^2 = \epsilon^2/|\mathbf{l}_1|^2$ — they appear small in comparison to the size of the arcs. Consequently, the contributions due to the two arcs (which are not even in the space of bulk modes) vanish in the limit that the zeros are small. However, we do not claim that each curved portion contributes infinitesimally; it's the difference between the two that does. Therefore, we're left with the contribution due to the solid lines, which are in the space of bulk modes. A zero mode in upper part of the complex plane will cause the phase of $\det \mathbf{R}(\mathbf{q})$ to wind by $+2\pi$, while those with negative imaginary part will induce a winding of -2π. By this argument, the integration over the real line (between $-\sqrt{\epsilon}/|\mathbf{l}_1|$ and $+\sqrt{\epsilon}/|\mathbf{l}_1|$) returns an integer, which couples with the conventional definition of polarization. In Appendix A.4, we explore in greater details the error associated with the choice of our contour and how more aggressive limits capture the transition more sharply.

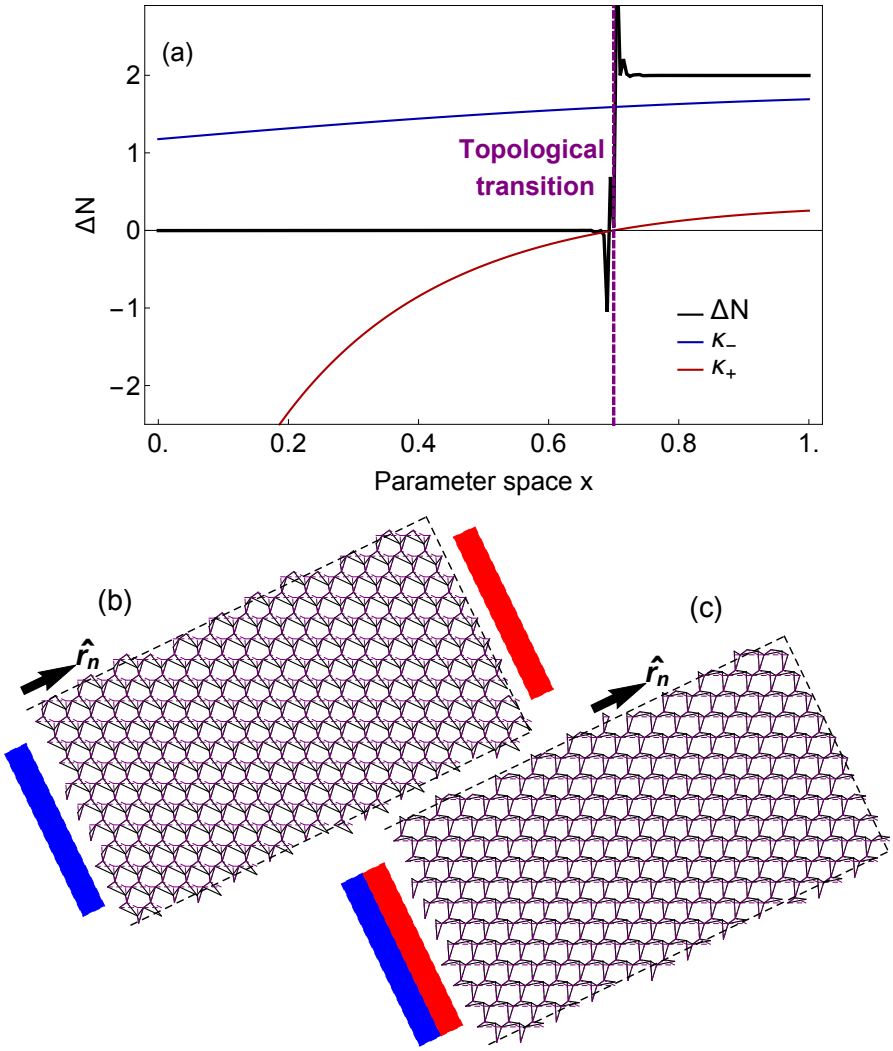

Figure 3.4: (a) Topological transition as we deform the Kagome lattice. Its geometry is parametrized as $\mathbf{g}(x) = x\mathbf{g}_1 + (1-x)\mathbf{g}_2$. $\kappa_\pm$ are the signed inverse decay lengths, such that when one vanishes the associated mode lies in the bulk and when both have the same sign the system is polarized. (b) The system in the $\mathbf{g}_1$-configuration with trivial polarization along $\hat{r}_n$: the two zero modes are split between the two edges. (c) The system is topologically polarized this time ($\Delta N = 2$): this time, the two modes are on the left side $\hat{r}_n$. On all three figures, the purple dashed lines represent the shape of the system at the topological transition (when $x = 0.7$).

We now apply our theory and our new invariant to a particular microstructure: a deformed Kagome lattice. To demonstrate that topological polarization does occur, we deform the system continuously until it reaches a topological transition, and even beyond [figure 3.4 (a)]. We will explain in the next subsection why we can consider a different direction for our polarization than $\hat{x}$. Originally, the system topologically is trivial [figure 3.4 (b)] and as we deform it, the mode on the right slowly but surely moves to the left edge to form a polarized system with invariant $N_L - N_R = +2$ [figure 3.4(c)].

3.6.2 Topological polarization as a vector

So far we've focused on edge modes which decay onto the bulk along the horizontal direction, away from a vertical interface with "the outside". Since we deal with a continuum theory, it is reasonable we ask how such modes behave when the interface is "tilted" by an angle θ with the y axis, and the direction of decay is changed accordingly. Let's define such direction in wavenumber space (while assuming the conversion to real space is trivial) as $\hat{q}_n(\theta) \equiv \cos\theta\,\hat{q}_x + \sin\theta\,\hat{q}_y$, while the interface is rotated by angle $\pi/2$ angle from it: $\hat{q}_t(\theta) \equiv -\sin\theta\,\hat{q}_x + \cos\theta\,\hat{q}_y$. Therefore, by performing a simple rotation transformation, we can express the wave vector $\mathbf{q}$ in its original $\hat{q}_x, \hat{q}_y$ basis and in the rotated one

$$\mathbf{q} = q_x\hat{q}_x + q_y\hat{q}_y = q_n\hat{q}_n + q_t\hat{q}_t, \tag{3.31}$$

with:

$$\begin{cases} q_n = \cos\theta q_x + \sin\theta q_y \\ q_t = -\sin\theta q_x + \cos\theta q_y \end{cases} \iff \begin{cases} q_x = \cos\theta q_n - \sin\theta q_t \\ q_y = \sin\theta q_n + \cos\theta q_t \end{cases} \tag{3.32}$$

This allows us to re-write the determinant of $\mathbf{R}$ in the new (q_n, q_t) basis and find the

long-wavelength modes of present interest:

$$\det(\mathbf{R}(\mathbf{q})) = A'_{2,0}q_n^2 + A'_{1,1}q_n q_t + A'_{0,2}q_t^2 + iA'_{3,0}q_n^3 + \dots \tag{3.33}$$

$$\implies q_n = \alpha_\pm(\theta)q_t + i\beta_\pm(\theta)q_t^2, \tag{3.34}$$

where once again the sign of $\kappa_\pm(\theta) \equiv \beta(\theta)q_t^2$ determines the polaization along the particular $\hat{r}_n(\theta)$ direction. Using this new expressions, and as indicated for a fixed Kagome lattice system (figure 3.5), we demonstrate that the modes are not uniformly spread around the system and that the topological polarization change at different angles. In particular, we notice the presence of so-called *soft directions* indicated by orange lines on figures 3.5 (a, b), which split regions where the topological polarization along $\hat{r}_n(\theta)$ changes.

3.6.3 Soft directions

We explore how these soft directions shape up from the expression of the zero modes of Eq. (3.25). In the context of mechanical lattices, soft deformations that are topological in nature have been found in the bulk [61]. In our continuum limit, the soft directions are given by solving the determinant of the rigidity map only to 2^{nd} order and solely depend on the $\alpha_\pm$ coefficients:

$$q_x = \alpha_\pm q_y \implies \hat{q}_\pm = \frac{(\alpha_\pm, 1)}{\sqrt{1+\alpha_\pm}}. \tag{3.35}$$

Similarly to the previous subsection, we can re-write the determinant of a generic wave vector $\mathbf{q}$ in this new basis $\mathbf{q} = q_+\hat{q}_+ + q_-\hat{q}_-$:

$$\det(\mathbf{R}(\mathbf{q})) = A''_{1,1}q_+q_- + iA''_{3,0}q_+^3 + iA''_{2,1}q_+^2q_- + \dots, \tag{3.36}$$

with the caveat that the basis here is no longer orthonormal. Importantly enough though, if a wave vector lies entirely on either soft directions, i.e $\mathbf{q} = q_+\hat{q}_+$ or $\mathbf{q} =$

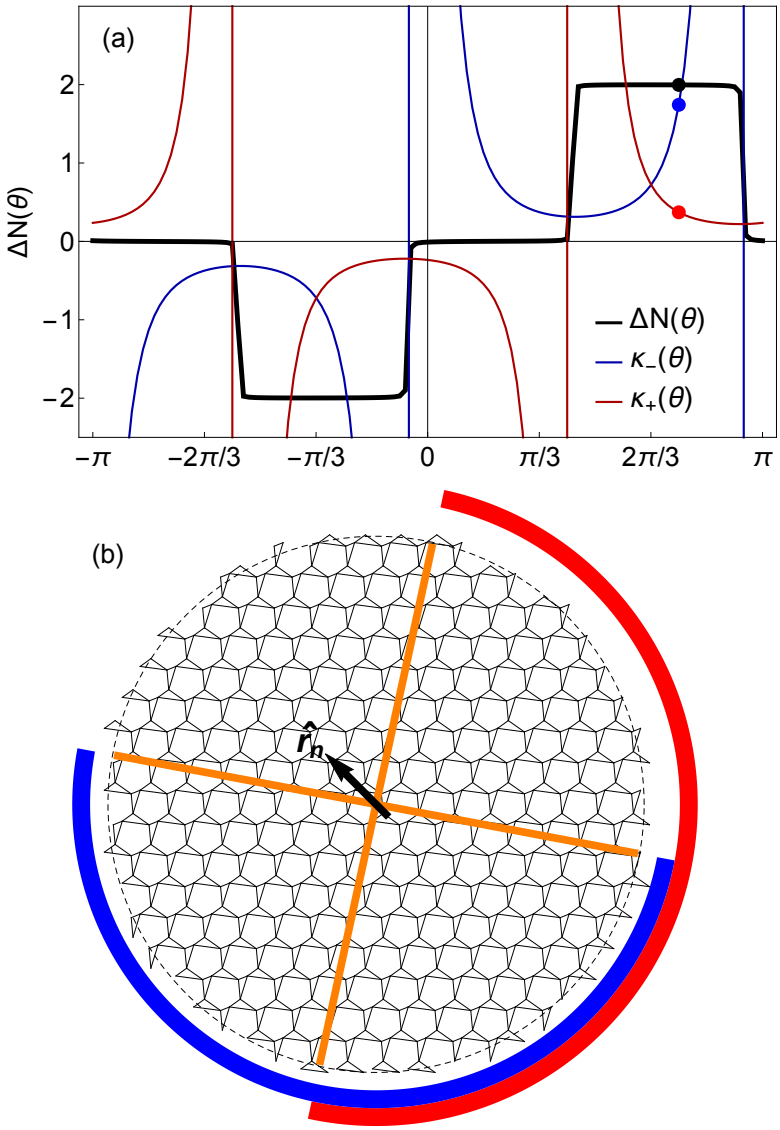

Figure 3.5: (a) For a fixed deformed Kagome, we numerically compute the signed inverse decay length of each mode $(\kappa_-(\theta), \kappa_+(\theta))$ and the topological polarization $\Delta N(\theta)$ of Eq. (3.30). We do so as a function of the normal direction $\hat{r}_n(\theta)$. (b) A chunk of the system in the bulk which highlights the presence of soft directions (orange lines). The polarization $\Delta N(\theta)$ changes as the normal crosses either soft directions. Between the split regions, the presence the two $\pm$ edge modes is highlighted by the arcs (respectively red / blue).

$q_-\hat{q}_-$, it is by definition a zero of our rigidity map to 2nd order.

3.7 Experimental Length Scales

We'll now focus on how the soft directions direct the propagation of an edge mode through the bulk. For that, we consider an interface oriented along the $\hat{r}_t(\theta)$ direction, with imposed boundary mode q_t. For it to be a zero, the system must undergo a deformation associated with one (or both) of the two soft directions described in the preceding section, which we cover in Appendix A.5. In summary, we utilize Eq. (3.36) to find the space of zero modes expressed in the "soft basis" while accounting for the value of the mode at the boundary. The result: the wave vector contributes to first order along the soft direction, while the decay along the normal to the inteface $\hat{q}_n$ is second order

$$\mathbf{q}_\pm = \frac{q_t}{\hat{q}_\pm \cdot \hat{q}_t}\hat{q}_\pm \pm i q_t^2 \frac{A''_{3,0(0,3)}}{A''_{1,1}} \frac{|\hat{q}_+, \hat{q}_-|}{(\hat{q}_\pm \cdot \hat{q}_t)^3}\hat{q}_n, \tag{3.37}$$

where $|\hat{q}_+, \hat{q}_-|$ denotes the area spanned by the corresponding unit vectors. Define $\theta_\pm, \theta$ the angle of the soft and the normal directions with respect to the x axis, then

$$\mathbf{q}_\pm = \frac{q_t}{\sin(\theta_\pm - \theta)}\,\hat{q}_\pm \pm i q_t^2 \,\frac{A''_{3,0(0,3)}}{A''_{1,1}}\,\frac{\sin(\theta_+ - \theta_-)}{\sin^3(\theta - \theta_\pm)}\hat{q}_n. \tag{3.38}$$

We note that the decay part of this expression includes both the value of the mode on surface, the orientation of the surface with respect the soft direction and the system's parameters (in the A" terms). Let's now rewrite the decay part in terms of unitless quantities and the wavelength on the boundary λ:

$$\left[\frac{\zeta_\pm}{|\mathbf{l}_1|}\right] = \pm\frac{1}{(2\pi)^2}\left[\frac{\lambda}{|\mathbf{l}_1|}\right]^2\left[\frac{|\mathbf{l}_1|A''_{1,1}}{A''_{3,0(0,3)}}\right]\frac{\sin^3(\theta - \theta_\pm)}{\sin(\theta_+ - \theta_-)}. \tag{3.39}$$

$\zeta_\pm$ are referred as the penetration depths of the two modes. One interesting fact is

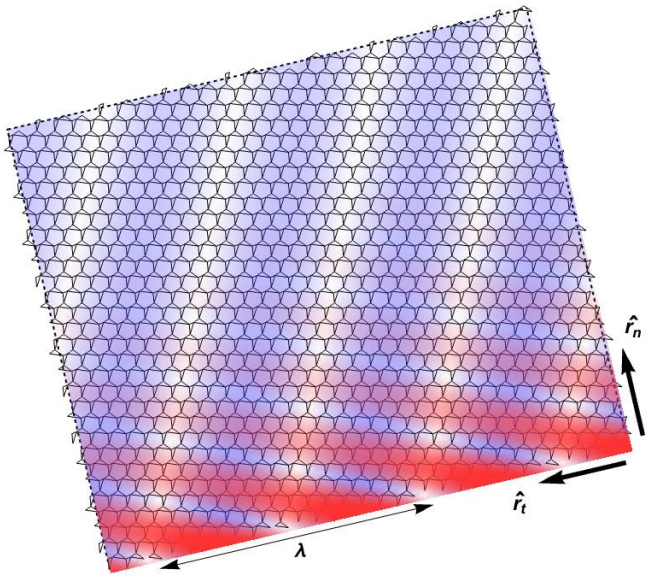

Figure 3.6: Shape of the two edge modes in a system with polarization $\Delta N = 2$. On the boundary, which is oriented along $\hat{r}_t$, we impose a mode with wavelength $\lambda = 15.6\,|\mathbf{l}_1|$ (where $\mathbf{l}_1$ is the first lattice primitive vector of the microstructure). The modes then decay through the bulk, along the direction $\hat{r}_n$ and over length scales much longer than the imposed wavelength λ. Each mode (red, blue) varies sinusoidally along its corresponding soft direction and therefore also varies along the boundary.

that such depth is proportional to the square of the number of cells over which the mode extends on the surface. We can imagine for a continuum system that extends over millions and millions of cells that if we distort the surface of a polarized material over thousands of cells, the mode decays into the bulk over millions. Hence, the surface theory extends from microscopic wavelengths up to the order of the geometric mean of the system size. This binds well with how conventional elasticity is applied to continuum systems, where the mechanical response observed is over distances far greater than the size of an atom . We may also put to use the significance of the other terms of Eq. (3.39). In fact, we see that the closer the normal direction is to the soft direction ($\theta \approx \theta_{\pm}$), the corresponding mode may decay considerably less. The "flexibility"feature of our theory could then be observed in much smaller systems.

Finally, we make a statement on nonlinearities it is true that small, linear strains dominate the nonlinear contributions, which are second order in strain (ϵ^2), but it is critical that the nonlinear terms do not "overshadow" the gradients of linear strains. In general, those are small compared to the linear strains and yet, they are determinant to the topological nature of our theory since they break spatial inversion symmetry. In other words, we want the strain to be respectively smaller than their gradients, and yet still be smaller than 1. For that reason, the ratio of lattice length scale ($|\mathbf{l}_1|$) to the length scale of deformation (λ) must be large compared to the infinitesimal strain: $\epsilon \ll |\mathbf{l}_1|/\lambda \ll 1$.

3.8 Conclusions

Throughout this chapter, we've introduced a model that describes the energetic costs of macroscopic strain fields and their gradients on a microstructure. In order to retain the long-wavelength nature of these strains, the model relies on a relaxation of the unit cell of the microstructure, which in turn induces a topologically protected bulk-boundary correspondence. This correspondence can be expressed via the bulk

and surface energetic terms of this system. While they're guaranteed by the bulk structure, these topological effects are determined by a new topological invariant expressed in the long-wavelength regime, which establishes the relative number of zero-energy edge modes on opposite boundaries. We've shown that these surface modes extend deep within the bulk, on length scales much larger than the unit cell. One key feature is that such model may clear the way to topological systems that do not rely on a microstructure, the only condition being that their mechanics are governed by a map which is isostatic nature (same degrees of freedom and constraints) and which breaks spatial invariance symmetry.

While this type of topological studies of discrete, lattice models extended in the continuum limit are relatively new (we mention that a similar study than the one of this chapter was released roughly around the same time as our publication [83]), other continuum-like systems have benefited from mechanical criticality for quite some time now. Those include the jammed packing systems [84, 85] we've eluded to in Chapter 1 and often enough, the breaking of spatial inversion symmetry rely on additional particles or external fields (e.g. shape of substrate). We must also admit that some other continuum-like systems cannot display polarized zero-energy deformations. For example, while origami sheets bring interesting mechanics due to their curvature [26], the continuum limit of triangulated origami sheets cannot polarize, as the lattice model have been shown not to [27]. In other examples, systems of rigid square pieces joined at corners [22] have been shown to possess nonlinear zero-energy dilations, but their continuum models [86, 87] have not revealed that those lie on the boundary.

We surely hope that such continuum model can be expanded to other mechanical lattices that exhibit topological effects of all kinds: those with directional response in the bulk [4], topological dislocations [40], topological buckling via states of self-stress [39], topological fracture [69] and topological helical edge modes [88]. Because

of the nature of the relaxation, which occurs at short-wavelength and at the unit cell of our microstructure, we are hopeful that relaxation mechanism can be applied to non-periodic structures, such as those totally amorphous [2] or those inspired by biological allostery [89, 90], so long as we're able to break the spatial inversion symmetry.

Chapter 4
MECHANICAL RESPONSE IN NON-IDEAL SYSTEMS: BOUNDARY EFFECTS, ADDITIONAL BONDS, AND DISORDER

So far, we've covered how boundary deformation modes of isostatic systems are generated by the bulk structure via a topological invariant. In order to observe these boundary modes, we must let the boundaries be free of constraint; in other words, we cut the bonds at the boundary to break the periodicity and a clear interface is drawn between the material and the surrounding environment. Previous studies have established metrics to determine the polarization of an edge and its ability to change depending on the bulk structure [63, 82]. Additionally, for periodic Maxwell lattices, we know there exists a Guest mode (a soft homogeneous deformation) regardless of the geometries of the unit cell [81]. In the beginning of this chapter, we uncover new methods that characterize the stiffness of an edge and the concept of polarization in finite open boundary systems. We connect with our work established on micromorphic continuum elasticity [33] to compute how the intensity of edge modes extends through the bulk in lattices of bonds connected by springs. Later, we explore how deformations are generated (and how we quantify them) in periodic systems upon the application of a mechanical perturbation in the bulk of non-ideal systems. Finally, we employ disorder effects, such as bond swapping and bond weakening, to generate new soft deformations in the bulk of metamaterials.

4.1 Boundary Effects

While the concept of polarization has definitely been explored in metamaterials, it was first introduced for those topological in nature by Kane and Lubensky in the form

of Bravais lattice vectors [6]. The topological invariants needed here are the numbers of zero modes on each edge of the lattice, one edge at a time. Instead, similarly to the new invariant introduced in chapter 3, we're interested in an analytical metric which computes the number of zero modes on opposite sides of a lattice direction for *finite size* systems. For the example of a periodic lattice with open boundary conditions, we can numerically compute the spatial extent of zero modes exponentially located on the left minus those on the right edge. We require open boundary conditions along the direction in question (let's say the first lattice vector) and make the problem considerably easier by keeping periodicity along the remaining direction (the second lattice vector). Therefore, since a zero mode is created for each bond cut, the total number of zero modes is proportional to the number of cells along the second lattice direction. We then define the *edge polarization*

$$P \equiv \frac{N_L - N_R}{N_L + N_R} \tag{4.1}$$

where N_L, N_R represent respectively the spatial extent of the modes on the left/right of the lattice, specifically

$$N_L = \sum_{n_1 < N_1/2} \sum_{i,k} |u_i^2(n_1, n_2, k)|. \tag{4.2}$$

The index i here refers to all the zero modes, while k is the site index within each cell. While it makes a little difference for P in large lattices, it is even more sensical to remove the contribution of the uniform translations, as our focus is truly on the exponentially localized edge modes. For a typical deformed Kagome lattice as the one plotted in figure 4.1, the expected polarization is -1, since all the edge modes are exponentially growing near the right edge (numerically, we find that $P = -0.96$).

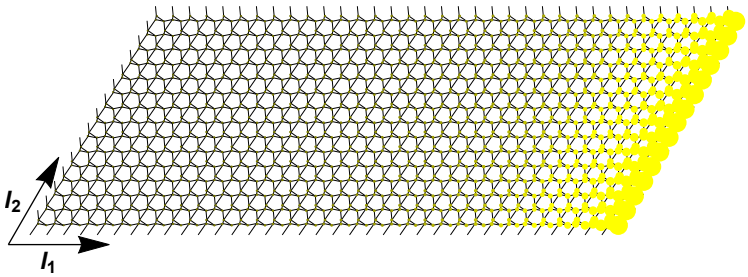

Figure 4.1: Deformed Kagome lattice with open boundaries along the first lattice direction ($\mathbf{l}_1$), periodic along the second ($\mathbf{l}_2$). We compute the polarization for a 35×15 cells system from Eq. (4.1) and find $P = -0.96$ and plot the spatial extent of the edge modes in yellow.

4.1.1 For a 1D system

We now look to connect this polarization evaluated analytically with our continuum theory. We start with the *one-dimensional rotor chain*, a representation of the Su-Schrieffer-Jeeger model for polyacetylene [68] for which the formation of a topological soliton wave has been derived in the nonlinear regime [76]. The 1D rotor chain is similar to the SSH in that the respective phonon and electronic spectrums possess the same gap [3]. We attach a visual representation of both structures from the 2015 Review article by Lubensky, Kane, Mao, Souslov and Sun. (figure 4.2). The rotor 1D chain consists of an assembly of rotors, with one end attached to a neighboring bar via a spring, while the other end is fixed. This allows for rotation of the free ends, under energetic constraint due to the springs (on the figure, these rotations are labeled by $\delta\theta_i$). The SSH model consists of two sublattices A and B [figure 4.2 (a, b)]; the two ends of each spring in the 1D rotor chain couple to elements of the sublattices. When the rods are aligned vertically while at rest, the rotor model is characteristic of a polyacetylene chain with identical bonds [figure 4.2 (a, c)]. But when the bars are tilted by an angle $\bar{\theta}$, the rotor chain represents the dimerized state of the polymer chain with double bonds [figure 4.2 (b, d)]. This last scenario precisely characterizes the nontrivial topological state.

We parametrize the mechanics of this system using our linear theory in the next

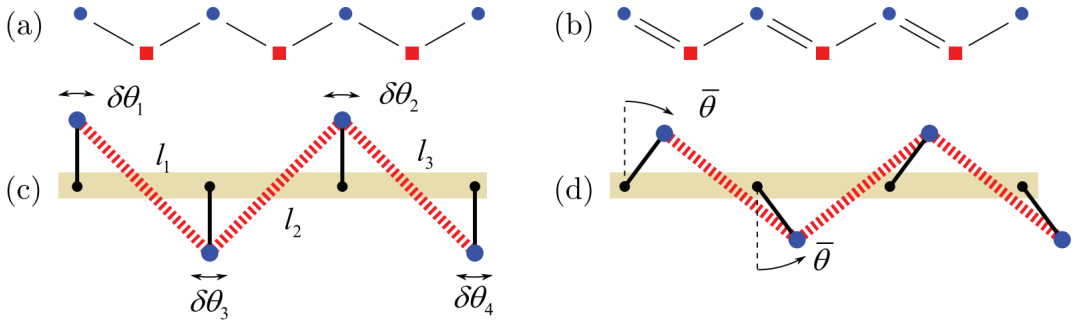

Figure 4.2: Representation of the SSH model for polyacetylene via the 1D isostatic chain of rotors connected by springs. For each of the two topological configurations considered, the SSH model is drawn with its corresponding 1D rotor chain (left figures vs right figures). On the left, we have the trivial state: (a) sublattices A (blue) and B (red squares) are connected by a unique type of bonds while (c) represents the 1D chain of rotors, positioned vertically in equilibrium. On the right, we have the nontrivial state: (b) the dimerized state of the SSH model and its corresponding 1D chain (d) where the rotors are slightly tilted by an angle $\bar{\theta}$ with respect to the vertical axis [3].

section (section 4.2) but also in Appendix B.2. For now, like in the 2D deformed Kagome, one must consider that the nontrivial topological state manifest itself in open boundary chains by sets of zero-energy deformations exponentially localized on one side of the lattice. For a lattice of N sites connected by $N-1$ springs, following Bloch's theorem [66], the magnitude of the rotation of the n^{th} rotor is

$$|u(n)| = |u_0|e^{-\kappa n}, \tag{4.3}$$

where $|u_0|$ is the amplitude of the mode and where κ is a constant of the system. Like in the continuum, κ is the inverse decay length and its sign tells us whether the mode is on the left ($\kappa > 0$) or on the right ($\kappa < 0$), with the difference that it is now a dimensionless quantity. The case $\bar{\theta} = 0$ is precisely the topologically trivial state for which case $\kappa = 0$. The reader must realize that those sets of linear rotations $\mathbf{u}$ are the small displacements labeled by $\delta\theta_i$ on figure 4.2. To be completely clear, the notation used for these small rotations will be $\mathbf{u} = (u_0, u_1, ...)$ from now on, as they represent sets of generalized coordinates that make up the mode. Since the connection with our

lattices of sites connected by springs is evident, we will refer to **u** as the displacement vector, even though its a symbol for the small rotations of the bars in this context.

This means the shape of the intensity profile is $|u(n)|^2 = |u_0|^2 e^{-2\kappa n}$. For a system sufficiently large (i.e. $N \to \infty$), we can use the continuum approximation and calculate the polarization like we did in equation (4.1):

$$P = \frac{\int_0^{N/2} |u(n)|^2 dn - \int_{N/2}^{N} |u(n)|^2 dn}{\int_0^N |u(n)|^2 dn} = \tanh\left(\frac{\kappa N}{2}\right) \tag{4.4}$$

4.1.2 For a 2D system

Let's now re-consider the 2D deformed Kagome lattice of figure 4.1 without assuming the continuum limit yet. The family of edge modes follows the same exponential form as the 1D rotor chain, except now, we deal with multiple edge modes. There is a total of N_2 rows and hence, a total of $2N_2$ zero modes from cutting as many bonds along the first lattice direction. The polarization is then

$$P(N_1, N_2) = \frac{1}{2N_2} \sum_{j \text{ modes}} \tanh\left(\frac{\kappa_j N_1}{2}\right). \tag{4.5}$$

One can evaluate the value of the decays κ_j using the **z**-periodic rigidity matrix. In fact, as a brief recall, zero modes in wavenumber space are those that cancel the determinant of the rigidity map $\mathbf{R}(\mathbf{z})$ and since we deal with a Maxwell system, the rigidity map admits two physical zero-energy solutions for each transverse wavenumber (Chapter 3) :

$$\det \mathbf{R}(z_1, z_2) = 0 \implies z_1 = f_k(z_2) \text{ with } k \in \{1, 2\}, \tag{4.6}$$

where each function f_k is analytical in z_2. While the edge mode in wavenumber space can be expressed using Bloch's theorem, the decay component can carry a nonzero

imaginary part, but the other must satisfy periodic boundary conditions along the transverse direction:

$$z_{2,j} = \frac{2\pi i}{N_2} j \text{ with } j \in \{0, 1, ..., N_2 - 1\} \tag{4.7a}$$

$$z_{1,j} = e^{ik_1 - \kappa_j} \implies \kappa_j = -\log|z_{1,j}| = -\log|f_k(z_{2,k})| \tag{4.7b}$$

While this results gives us the exact shape of the edge mode, we can use our work on the continuum limit to approximate an analytical expression for the inverse decay term κ_j. In fact, we know it is proportional to the square of the wavenumber in the transverse direction. In other words,

$$\kappa_j \approx -\beta_0 \left(\frac{2\pi}{N_2} j\right)^2 = -\beta \frac{j^2}{N_2^2}. \tag{4.8}$$

where β_0, β are constants defined by the system. We've shown that these constants can vary widely in magnitude if the decay direction considered lines up with one of the two soft directions of the system [33], but we do not consider this case here. Still, the sign of β indicates where the mode is: for the deformed Kagome system of figure 4.1, it is on the right, therefore $\beta > 0$. For such system, we can derive analytically the finite-size corrections of the polarization with respect to the expected value (-1), which we often refer to as the error from the continuum approximation:

$$\text{error} = -1 - P = \frac{-1}{N_2} \sum_j \frac{1}{1 + e^{-\kappa_j N_1}}. \tag{4.9}$$

We can then approximate for a very large system $(N_1 \times N_2) = (N, N)$ with $N \to \infty$ using Eq.(4.8)

$$\text{error} \approx \frac{1}{N} \sum_j \exp\left(-\beta \frac{j^2}{N}\right). \tag{4.10}$$

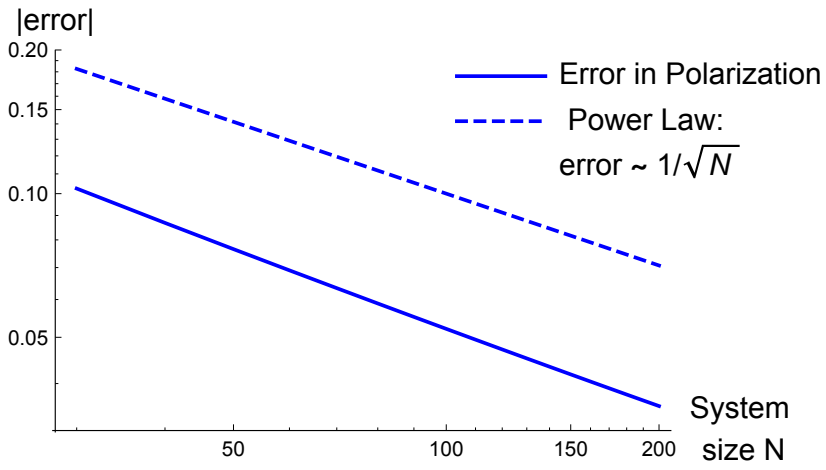

Figure 4.3: Log-log plot of the finite polarization with respect to its expected value as a function of the system's size (the error), for the deformed Kagome lattice of figure 4.1. Given the expected value is $P = -1$, the polarization error is evaluated using Eq. (4.9) (solid line) for a system growing in size in both lattice directions $N_1 = N_2 = N$. The expected power law for the error evaluated in the continuum limit is drawn as well (dashed line).

In the continuum limit, the error is the cumulative distribution over the space of modes of a normal distribution centered around the origin but with standard deviation $\sigma = \sqrt{N/2\beta}$:

$$\text{error} = \frac{1}{N}\int_j \exp\left(-\frac{\beta j^2}{N}\right) dj = \sqrt{\frac{\pi}{\beta N}}\,\frac{1}{\sigma\sqrt{2\pi}}\int e^{-\frac{1}{2}\left(\frac{j}{\sigma}\right)^2} dj. \tag{4.11}$$

This indicates that the error dependance of the system size is a power law as the system grows large (figure 4.3),

$$\implies \text{error} = \sqrt{\frac{\pi}{\beta N}} \text{ as } N \to \infty. \tag{4.12}$$

4.1.3 Density of Modes

We've seen the properties of this finite polarization metric, which varies depending on the system size but yet still connects with the difference of winding numbers on opposite edges. Still, we haven't described for a given 2D lattice, how the mode

decays through the bulk. We therefore introduce the concept of *modes density* (often referred as mode intensity too). Picking up once again on the example of figure 4.1, this density profile is defined per cell n_1 with $1 \leqslant n_1 \leqslant N_1$. However, it is clear that it is invariant across the second lattice direction, as the wavenumber in that direction is purely imaginary. Upon renormalization, we define the density profile per cell as

$$v(n_1, n_2) = \sum_{\text{zm } j,\ \text{site } k} |u_j(n_1, n_2, k)|^2 \tag{4.13}$$

$$\text{with} \sum_{n_1, n_2, k} |u_j(n_1, n_2, k)|^2 = 1, \text{ for each mode } j, \tag{4.14}$$

with the condition that v depends only on n_1. Since the displacement profile follows $|u_j(n_1, n_2)| = |u_0| \exp(-\kappa_j n_1)$, the normalization condition imposes that

$$|u_j(n_1, n_2)|^2 = \frac{1}{N_2} \frac{1 - e^{-2\kappa_j}}{e^{-2\kappa_j} - e^{-2\kappa_j N_1}} e^{-2\kappa_j n_1}. \tag{4.15}$$

Therefore, in the limit case where the system is large enough, $N_1 = N_2 = N \to \infty$, the density is such that

$$v(n_1) = \frac{1}{N} \sum_j \exp\left(-2\kappa_j (n_1 - 1)\right) - \exp\left(-2\kappa_j n_1\right). \tag{4.16}$$

For the sake of having the sum converging, this expression requires that the cell index counts away from the edge that carries the exponentially localized modes. In other words, if the mode is on the left ($\kappa_j > 0$) then the cell index $n_1 > 0$ counts from left to right, whereas if it is on the right ($\kappa_j < 0$) the cell counts from right to left ($n_1 < 0$). This change of orientation is frequently seen when computing the winding number on different surfaces [5,63]. For now, let's assume that the mode is in fact on the left ($\kappa_j = +\beta(j/N_2)^2$). While taking the continuum limit, we can compute the

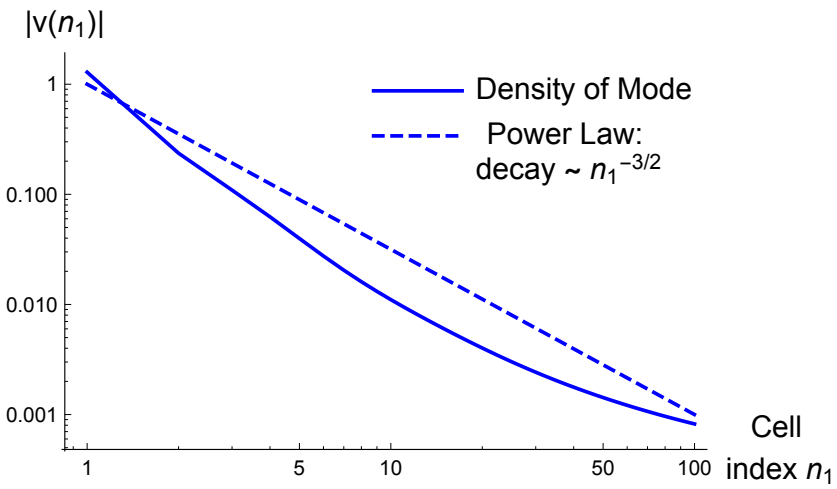

Figure 4.4: Log-log plot of the density of modes through the system, where n_1 indicates the cell numbering away from the polarized edge (right) for the deformed Kagome lattice of figure 4.1. The modes' density $v(n_1)$ is evaluated using Eq. (4.16) (solid line) for a system with $N = 100$ cells. The expected power law for the modes' density is evaluated in the continuum limit (dashed).

density of mode by turning the sum into an integral:

$$v(n_1) = \frac{1}{N}\int dj \Big(\exp\big(-\frac{2\beta(n_1-1)}{N^2} j^2\big) - \exp\big(-\frac{2\beta n_1}{N^2} j^2\big)\Big) \tag{4.17a}$$

$$= \sqrt{\frac{\pi}{2\beta}} \left(\frac{1}{\sqrt{n_1 - 1}} - \frac{1}{\sqrt{n_1}} \right) \tag{4.17b}$$

which indicates that for large n_1, the density of modes decay in power law as seen on figure 4.4:

$$v(n_1) \sim n_1^{-3/2}. \tag{4.18}$$

This formula indicates that the intensity of the zero-energy boundary modes decay quite sharply into the bulk of those lattice systems (for example compared to a decay in $1/n_1$). To be clear, these are the displacements resulting from opening the boundaries and are not comparable with surface modes from imposed surface distortions in the continuum limit that we studied in section 3.7.

4.2 The Response Position

While the intrinsic nature of the mechanics at the boundary is of interest, it is equally important to understand how a material will deform once it undergoes perturbation. Unconventional elastic responses have been found in programmable metamaterials, such as those whose bulk response to compression on the boundary is determined by confinement [91]. The programmability of materials and their ability to deform is of critical importance in engineering and in soft robotics [92]. But so far, we've barely investigated any topological signatures happening in the bulk. Earlier studies show that topological states of matter can prevent fractures under stretching in metamaterials, as most of the stress can be directed toward domain walls of the system [69]. Our goal is now to establish models that quantify the directional response of a variety of flexible metamaterials that undergo applied stresses.

In this section, we follow the work done by Rocklin on the directional response in metamaterials [4] and look to expand it to a broader range of systems. Our intention is to establish the mathematical tools needed to connect the bulk-boundary correspondence established by Kane and Lubensky [6] with the mechanical response to systems beyond the critical stability or those that lack periodic structure. In general, one can consider that the linear mechanical response to an applied force is *reciprocal*, in that the system deforms in all directions. However, we've seen that topologically protected materials support edge modes, which prompts the suggestion that a mechanical response can be polarized as well. In fact, previous work done by Rocklin has covered this well for Maxwell systems, as indicated on figure 4.5 [4]. Of particular interest is the connection between displacement responses due to bonds' swelling and stress responses due to applied forces. This relationship arise from the Maxwell-Betti reciprocity theorem [93], which in the context of lattice of sites

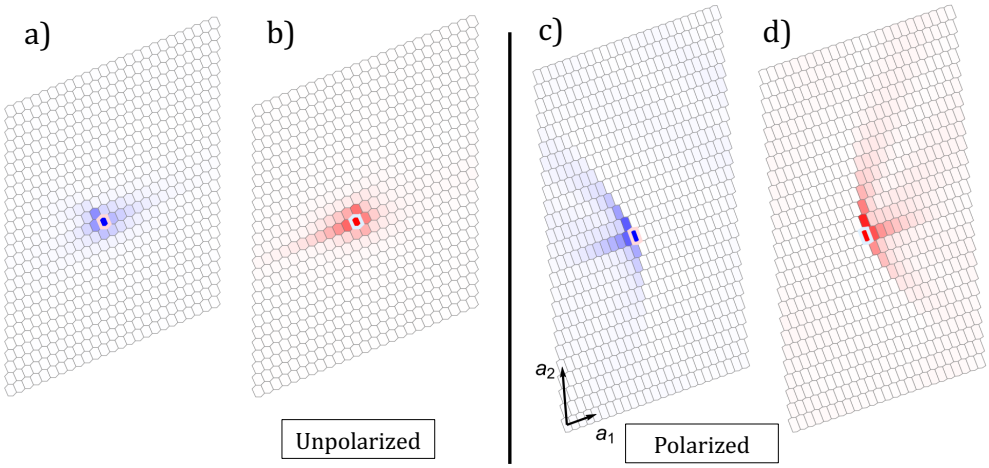

Figure 4.5: The response of unpolarized (left) vs polarized (right) Kagome lattices. Blue color indicates the displacement response due to the combination of bonds swollen/contracted (a, c), while red describes the intensity levels of bonds extensions/compressions due to an applied force (b, d). This image is taken from Ref. [4].

connected by springs reads:

$$\mathbf{u} \cdot \mathbf{f} = \mathbf{e} \cdot \mathbf{t}. \tag{4.19}$$

$\mathbf{u}$ is the displacement response due to a set of extensions $\mathbf{e}$, while $\mathbf{t}$ is the tension response due to an applied set of force $\mathbf{f}$. This means that the displacement response due to the swelling / contraction of bonds is identical to the tension response due to applied forces (figure 4.5). Additionally, if the system considered possesses a nontrivial polarization, these responses are localized on opposite sides of where the perturbation — the stretch or the force — is applied. We now look to expand the work done here in Maxwell systems to over-constrained lattices.

4.2.1 Introduction And setup

Generally speaking, in topological studies, it is common practice to search for topological invariants after having observed how a metric related to the conducting states of the system changes, as the system changes. Here though, we operate "in reverse" to this practice and search for a physical quantity that will indicate the localization

of the mechanical response in a system whose topology is known. Throughout this section, we derive the displacement response from the swelling of each bond located at position $\mathbf{r}_j$, all located within the same cell $\mathbf{n} = 0$. The stretching amount for each bond is unit in magnitude. Let $u_i^j(\mathbf{n})$ be the displacement of the site located at $\mathbf{r}_i$ in cell $\mathbf{n}$ due the stretch of bond at position $\mathbf{r}_j$. We also define $\underline{\mathbf{l}}$ the matrix of lattice vectors, which in two dimensions, can be expressed as $\underline{\mathbf{l}} = (\mathbf{l}_1, \mathbf{l}_2)$. Finally, we define the *response position* $\mathbf{RP}$ as the mean position of the displacement responses due the swelling of all the bonds considered:

$$\mathbf{RP} = \frac{\sum_{ij\mathbf{n}} |u_i^j(\mathbf{n})|^2 (\mathbf{r}_i + \underline{\mathbf{l}} \cdot \mathbf{n} - \mathbf{r}_j)}{\sum_{ij\mathbf{n}} |u_i^j(\mathbf{n})|^2}. \tag{4.20}$$

Before we go any further in investigating what this new metric is, we must understand to what this set of displacements $\mathbf{u}$ corresponds to. Per Chapter 2, the mapping of constraints between the displacement vector $\mathbf{u}$ and the space of springs extensions is the rigidity matrix $\mathbf{R}$. Then the energy cost for any sets of displacement $\mathbf{u}$ due to an imposed sets of *external* tensions $\mathbf{e}_{\text{ext}}$ is

$$E = (1/2) \left(\mathbf{Ru} - \mathbf{e}_{\text{ext}}\right)^T \mathbf{K} \left(\mathbf{Ru} - \mathbf{e}_{\text{ext}}\right). \tag{4.21}$$

Our focus is on the displacement response which reaches equilibrium, so that the displacements vector satisfies:

$$\frac{\partial E}{\partial \mathbf{u}} = 0 \implies \mathbf{R}^T \mathbf{K} (\mathbf{Ru} - \mathbf{e}_{\text{ext}}) = 0 \tag{4.22}$$

Those are precisely the force balance modes. As we show in Appendix B.1, for the types of system considered, Eq. (4.22) can be solved using the *Moore-Penrose inverse*,

denoted $\mathbf{R}^{-1,g}$. For periodic lattices, these modes are given by:

$$\mathbf{u} = \left(\mathbf{K}^{1/2}\,\mathbf{R}\right)^{-1,g}\ \sqrt{\mathbf{K}}\mathbf{e}_{\text{ext}}. \tag{4.23}$$

We now look to find the displacement term of equation (4.20). In wavenumber space, because the pseudo inverse is diagonal, we find that

$$u_i^j(\mathbf{q}) = (\mathbf{K}^{1/2}\mathbf{R}(\mathbf{q}))_{ij}^{-1,g}\sqrt{k_j}, \tag{4.24}$$

and that for a lattice system, using Bloch's theorem, the displacement response can be expressed via its Fourier transform:

$$u_i^j(\mathbf{n}) = \frac{1}{(2\pi)^{d/2}}\int d\mathbf{q}\, u_i^j(\mathbf{q})e^{i\mathbf{q}\cdot\mathbf{n}} \tag{4.25a}$$

$$\implies |u_i^j(\mathbf{n})|^2 = \frac{k_j}{(2\pi)^d}\int d\mathbf{q}d\mathbf{q}'\,(\mathbf{K}^{1/2}\mathbf{R}(\mathbf{q}))_{ij}^{-1,g}(\mathbf{K}^{1/2}\mathbf{R}(\text{-}\mathbf{q}'))_{ij}^{-1,g}e^{i(\mathbf{q}-\mathbf{q}')\cdot\mathbf{n}}. \tag{4.25b}$$

After a long and thorough derivation, we come to an expression for the response position in wavenumber space (Appendix B.2):

$$\mathbf{RP} = \frac{\sum_{ij}k_j(\mathbf{r}_i-\mathbf{r}_j)\int d\mathbf{q}\,\left|\left(\mathbf{K}^{1/2}\mathbf{R}(\mathbf{q})\right)_{ij}^{-1,g}\right|^2}{\sum_{ij}k_j\int d\mathbf{q}\left|(\mathbf{K}^{1/2}\mathbf{R}(\mathbf{q}))_{ij}^{-1,g}\right|^2} + i\,\underline{\mathbf{l}}\cdot\frac{\sum_{ij}k_j\int d\mathbf{q}\,\left(\mathbf{K}^{1/2}\mathbf{R}(\mathbf{q})\right)_{ij}^{-1,g}\,\nabla_{\mathbf{q}}\left(\mathbf{K}^{1/2}\mathbf{R}(\text{-}\mathbf{q})\right)_{ij}^{-1,g}}{\sum_{ij}k_j\int d\mathbf{q}\left|(\mathbf{K}^{1/2}\mathbf{R}(\mathbf{q}))_{ij}^{-1,g}\right|^2} \tag{4.26}$$

where all these integrals are evaluated across the Brillouin Zone: $-\pi \leqslant q \leqslant \pi$ in one dimension. As we can see, the response position is split between a intra-cell position (top-term) and a inter-cell contribution (bottom-term). The inter-cell contribution is of particular interest as it includes a geometric phase of the form $\int dq\langle u(q)|\partial_q|u(q)\rangle$, [67] where the states considered in the Berry's contribution are a combination of the

elements of the pseudo inverse of the rigidity matrix and the spring stiffnesses. These terms are actually the deformations evaluated at a wavevector $\mathbf{q}$: $\left(\mathbf{K}^{1/2}\mathbf{R}(\mathbf{q})\right)^{-1,g}_{ij} = u_{ij}(\mathbf{q})$.

We show that **RP** has the properties of a geometric phase. First, it is evaluated over the Brillouin Zone. Second, we show that this response position is *gauge invariant*. Regardless of how we define the cell, i.e. how we organize the sites and the bonds, the response position will remain unchanged. Physically speaking, we know it shouldn't. For example, suppose the site further to right in a Kagome lattice cell (figures 2.3 and 3.1) "belongs" to the adjacent cell to the right instead. For the sake of argument, define this site to be $i = 1$, then

$$r_{i=1} \to r_{i=1} + \mathbf{l}_1. \tag{4.27}$$

We show in Appendix B.2.2 that such a change of gauge transforms some terms of the rigidity map and of its pseudo-inverse:

$$R^{-1,g}_{1j} \to R_{1j}\, e^{-iq_1}, \tag{4.28}$$

which in turn produces an additional term to both intra-cell and inter-cell contributions of Eq. (4.26). These terms are equal and opposite in sign [see Eq. (B.24) and Eq. (B.26c)] cancel out and hence the response position as a whole is *invariant*.

4.2.2 Response position of the 1D rotor chain

In order to visualize the physical significance of **RP**, we now focus on one-dimensional systems that are topologically protected. The main example we'll use is the one we already mentioned in section 4.1: the SSH model, a system of rotors attached to one another with springs (figure 4.2). As we've mentioned earlier, the polarization of an open-boundary chain is theoretically ± 1, depending on whether the mode is exponentially localized on the left ($P = +1$) or on the right ($P = -1$). But how

does this manifest in the response due to a swollen bond in bulk? If we swell a bond (or contract it for that matter) in the bulk, we allow for a mode where the sites attached experience a missing bond. It's as if the swollen / contracted bond replicates the open boundary condition and therefore, the topological polarization directs the deformation mode to grow toward the swollen bond, the same way it would toward an open boundary. If $P = +1$ (-1) in theory, we expect the response to be located on the *right* (*left*) of the perturbation, with the mode growing exponentially as we get closer to the bond.

The linear relationship between the displacements (or rotations of the rotors, as explained in section 4.1) and the spring extensions is quite simple for the SSH model. In Appendix B.2.3, from the geometry of the system, we derive how to obtain the parameters a, b, both positive in value such that:

$$e_n = au_{n+1} - bu_n. \tag{4.29}$$

Assuming Bloch wave's form [66], i.e. that there exists a complex quantity $z = e^{iq}$ such that $u_{n+1} = zu_n$ then we can write the rigidity matrix in wavenumber space as follow

$$\mathbf{R}(q) = (ae^{iq} - b), \tag{4.30}$$

and the zero modes, those that lie in the null space of the rigidity map, are therefore given by

$$u(n) = u_0 \left(\frac{b}{a}\right)^n. \tag{4.31}$$

As we mentioned earlier, those zero modes have the same form as the displacement response in the bulk. If the system is polarized to the left, i.e. when the ratio $b/a < 1$,

the displacement response due to the swelling of a bond by unit magnitude in the cell $n = 0$ is then:

$$u(n) = \begin{cases} 0 \text{ if } n < 0 \\ \\ u_0 \left(\frac{b}{a}\right)^n \text{ if } n \geqslant 0. \end{cases} \tag{4.32}$$

A similar derivation can be made if $b/a > 1$. This ratio is precisely the inverse decay length we alluded to in section 4.1.

One important feature is that clearly, the mechanical response is only located on one side of the source. Because of such directional behavior, it is relevant to not only compute the mean positional response, but also to derive a response polarization metric, similarly to how we drew the polarization for edge modes in open-boundary systems. One could even formalize this response polarization and broaden its use to more complex mechanical systems than the 1D rotor chain. Assuming they lie in more than one-dimensional space, we can measure the mechanical polarization along a particular direction (let's call it $\hat{r}$), so that if all the displacement is on the right of the source along the $\hat{r}$ direction, then the polarization is $+1$. We offer the following definition for such metric:

$$P_{\hat{r}} = \frac{\sum_{ij\mathbf{n}} |u_i^j(\mathbf{n})|^2 \, \theta\left(\hat{r} \cdot (\mathbf{r}_i + \underline{\mathbf{l}} \cdot \mathbf{n} - \mathbf{r}_j)\right)}{\sum_{ij\mathbf{n}} |u_i^j(\mathbf{n})|^2}, \tag{4.33}$$

but limit its study to the 1D rotor chain considered. *From now on*, in order to facilitate our work, we will set the system's parameter $a = 1$ and focus solely on the value of b with respect to 1. By using the displacement profile of Eq. (4.32), we find as we expected that:

$$P_{\hat{r}} = \begin{cases} +1 \text{ if } b < 1 \\ \\ -1 \text{ if } b > 1 \end{cases} = \text{ sign}(1 - b^2). \tag{4.34}$$

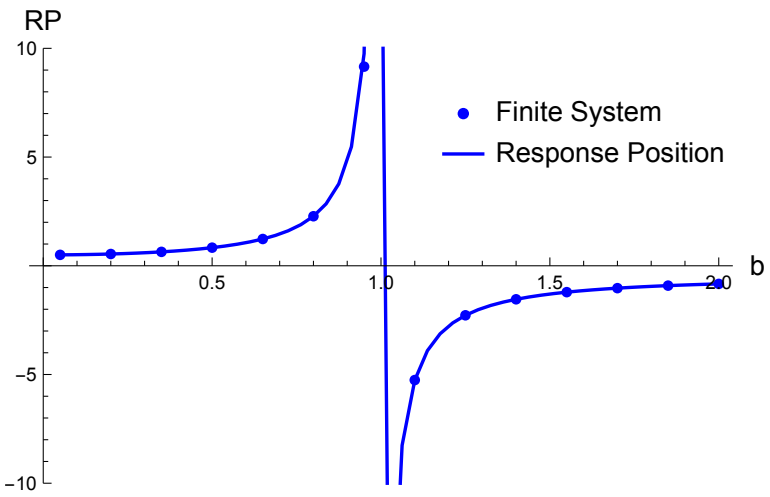

Figure 4.6: x component of the response position in the 1D Maxwell rotor chain, as we vary the "degree of polarization" b. The solid line represents the analytical derivation of such system [Eq. (4.35b)] while the dots are evaluated from the numerical formula of Eq. (4.20) for a $N = 100$ long rotor chain.

Returning to our *response position*, for one-dimensional isostatic systems, we've shown in Appendix B.1 that we no longer need to account for the spring stiffnesses, because if the rigidity matrix is invertible, then the zero force modes precisely are the zero modes of the rigidity map. Moreover, for the particular 1D Maxwell rotor chain, there is only 1 site and 1 bond per cell, and the center of a spring is half a distance between two consecutive sites. This means that $\mathbf{r}_p - \mathbf{r}_b$ — the position of the site with respect to the bond in each cell — is half a lattice unit: $\mathbf{r}_p - \mathbf{r}_b = 1/2\,\mathbf{l}$. This allows us to express the response position as a function of the lattice vector $\mathbf{l}$ and b

$$\mathbf{RP} = \mathbf{r}_p - \mathbf{r}_b + i\mathbf{l}\,\frac{\int dq\; R^{-1,g}(q)\partial_q R^{-1,g}(\text{-}q)}{\int dq\; |R^{-1,g}(q)|^2} \tag{4.35a}$$

$$\implies \mathbf{RP} = \left(-\frac{1}{2} + \frac{1}{1-b^2}\right)\mathbf{l}, \tag{4.35b}$$

given that for the 1D rotor chain,

$$\mathbf{R}(q) = (e^{iq} - b) \implies \mathbf{R}^{-1,g}(q) = 1/(e^{iq} - b). \tag{4.36}$$

On figure 4.6, we plot how the response position varies as a function of b, the "degree of polarization" of the chain. The chain is spread along the x direction, so in reality, we're plotting the x component of **RP**. We compare the analytical formula derived in Eq. (4.35b) against numerical finite results of a $N = 100$ rotor chains. We vary the value of b with respect to 1, at which the system goes through a topological transition. While the response position isn't topological in nature, its x component changing abruptly for $b = 1$ is a signature of the topological transition and indicates that the deformations are located on the left (when RP $> -1/2$) or on the right (when RP $< -1/2$). This change in the topology is reflected by a change of value of RP with respect to $-1/2$, which is the position of the site with respect to the bond. At $b = 1$, the response position diverges, since the system is simply the one-dimensional balls and springs chain. The only zero-energy mode is the mode of translation and hence, it follows that **RP** from its definitional argument [Eq. (4.20)] diverges under such circumstances.

4.2.3 The double spring rotor chain

We now consider a system one could say twice as complicated as the Maxwell 1D rotor chain: a rotor chain constituted of two different isostatic chains, each with a degree of polarization b_1, b_2 and each with a spring stiffness k_1, k_2. We can no longer not account for the difference in spring stiffnesses since the system is hyperstatic. As we've shown in Appendix B.2.4, it is then best to define a modified version of the rigidity map, one that accounts for spring stiffness matrix $\mathbf{K}$: $\mathbf{R} \to \mathbf{K}^{1/2}\mathbf{R}$. In which case, our new rigidity matrix is

$$\mathbf{R}(q) = \left(\sqrt{k_1}(e^{iq} - b_1), \sqrt{k_2}(e^{iq} - b_2)\right). \tag{4.37}$$

Once again, let's assume the chain to be along the x direction. We suggest the one-site of each cell to be at the origin $\mathbf{r}_p = 0$, that both springs and lattice vectors are along

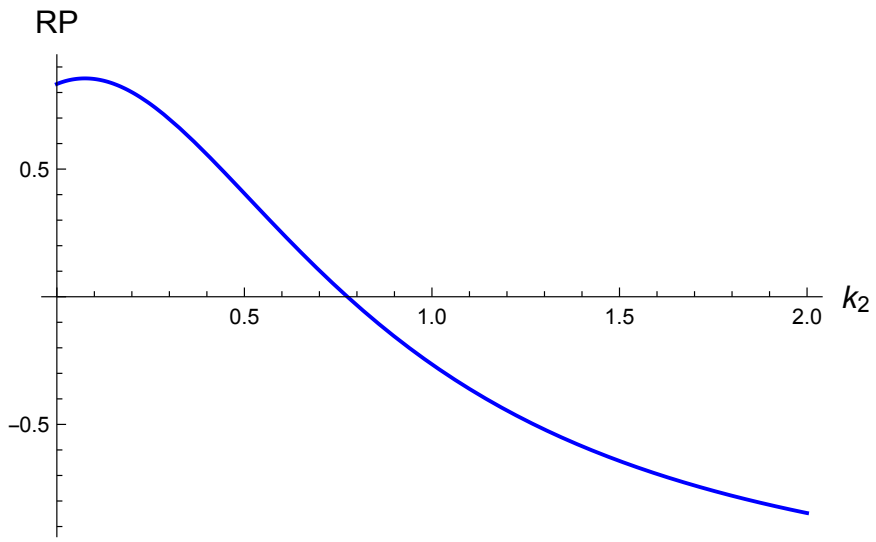

Figure 4.7: x component of the response position in the double rotor chain. We vary the spring stiffness of the second system k_2, while the first system stay fixed $k_1 = 1$ and so are the degree of polarization $b_1 = 0.5, b_2 = 3$. The solid line cross the x-axis as we tune the value of k_2, indicating the response position goes from right to left.

the x-direction $\mathbf{r}_1 = r_1\hat{x}$, $\mathbf{r}_2 = r_2\hat{x}$ and that $r_1 = r_2 = r_b = l/2$. The x component of the response position is then:

$$\mathrm{RP} = -1/2 - \frac{(k_1+k_2)\Big((b_1^2-1)\,k_1^2 - k_1k_2(b_1-b_2)^2 + (b_2^2-1)\,k_2^2\Big)}{(b_1^2-1)^2\,k_1^3 + (b_2^2-1)^2\,k_2^3 + \Big((b_1-b_2)^2 + (1-b_1b_2)^2\Big)\,(k_1^2k_2 + k_1k_2^2)}. \tag{4.38}$$

While its mathematical expression is long and complicated, we find the response position has the following properties:

- It's invariant under inversion of chain 1 with chain 2:

$$b_1 \leftrightarrow b_2, k_1 \leftrightarrow k_2 \implies \mathbf{RP} \to \mathbf{RP}. \tag{4.39}$$

- If one of the chain does not contribute, an inversion of the degree of polarization

implies the mean response to flip side

$$\text{for } k_{2,(1)} = 0, b_{1,(2)} \to 1/b_{1,(2)} \implies \mathbf{RP} \to -\mathbf{RP}. \tag{4.40}$$

- If both chains possess equal spring stiffness and their degree of polarization is inverse of one another

$$\text{for } k_1 = k_2 = 1 \text{ and } b_1 = 1/b_2 \implies \mathbf{RP} = -\mathbf{r}_b. \tag{4.41}$$

While the response position is certainly not a topological invariant, it is definitely practical in determining where the mechanical deformations of complex systems are located, and if they're somewhat directional. For example, as indicated on figure 4.7, we've shown that the response position of the double chain can switch from one side to the other, as we tune up the "strength" (the spring stiffness) of one of the polarized chains.

4.3 Limited Disorder in Polarized Systems

So far, we've only considered systems that are spatially periodic and whose only irregularities come from removing constraints (open-boundary systems) or from swelling/ contracting bonds. But we did not focus on disordered networks, and yet their applications in mechanical metamaterials have proven to show interesting results [94]. Topology is a robust mathematical feature; small and continuous changes brought to a system do not change the topological invariant that governs its physical effects and often, we would expect that a limited amount of disorder shouldn't change the topologically governed response of mechanical systems. In fact, we've seen that a system of gyroscopes on a system built from random point sets, still exhibited topological chiral edge waves on the boundary, despite the total loss of a Brillouin Zone [2]. While we do not claim to be able to replicate such study in the context of our mechani-

cal metamaterials, we show that limited disorder, such as "bond swapping" or "bond weakening" in a topologically protected system helps generate uncommon mechanical deformations.

4.3.1 Bond swapping in 1D

We once again refer to the 1D rotor chain studied by Kane and Lubensky [6]. If we decide to cut a bond, we would generate an additional zero mode by removing a constraint, which drives us away from the isostatic point. In order to remain isostatic, we swap one bond from the 1D rotor chain with its next nearest neighbor counterpart. In the SSH model, this "secondary" chain connects rotors two cells apart, instead of those closest to one another.

We look to generate mechanical responses from bond swelling that amplify the displacement response, where one can expect that the swelling of a bond causes large displacements even far away — comparable to a seesaw mechanism. Mechanical functionality is an important feature of metamaterials. For example, it has been shown that allostery-based mechanical responses are pretty successful at generating a target response far away from the imposed sources, using an efficient "bond cutting" algorithm method [89]. Rather than doing *bond swapping* from numerical simulation approach, we suggest a perturbative-based method that computes the mechanical response for a set of removed and added bonds.

We observe that for the case of the 1D rotor chain, in order to generate any amplifier-like response, the removed bond must be on the side of the polarization with respect to the source (i.e. to its right) and the added bond cannot be found between the source and the cut bond (figure 4.8 (b)). Compared to the system where the removed bond is on the other side (i.e. to its left on figure 4.8 (a)) the mode is $10-100$ larger in magnitude. The dissimilarity between the two responses comes from the contribution of the missing bond: we prove in Appendix B.3 that the mechanical deformations resulting from swelling the bond originates from a superposition of the

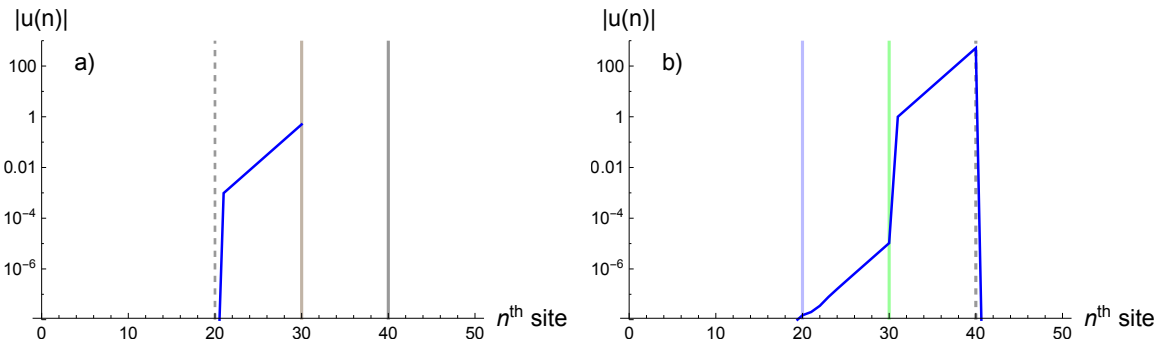

Figure 4.8: Response deformation due to the swelling at a bond (green line) in a system with a missing bond (dashed line) and an added bond from the next nearest neighbor chain (blue line). The 1D rotor chain considered here is polarized to the right. On figure (a), the missing bond is on the opposite side of the polarization, while in (b) it is on the proper side.

response mode and an edge mode. This edge mode exists because cutting a bond from the primary rotor system removes a constraint in the Maxwell-Calladine counting [64] [see Eq. (2.10)]:

$$\mathbf{u} = \mathbf{R}_0^{-1}\left(\mathbf{e}_s + a_i \mathbf{e}_m^i\right) \tag{4.42}$$

$$\text{with } \delta\mathbf{R}\mathbf{R}_0^{-1}\left(\mathbf{e}_s + a_i \mathbf{e}_m^i\right) \cdot \mathbf{e}_m^j = 0 \text{ for all } j \tag{4.43}$$

In the system studied on figure 4.8 (b), the large value of a_1 is precisely what creates such a large mechanical deformation response. While we recognize this could motivate the design of an experimental model to testify for this amplifier effect in mechanical systems, we also acknowledge that nonlinear effects must be accounted for such response [76] in that they would prevent the displacements to grow too large in amplitude. Other research on allosteric functionality in metamaterials has also shown that such target responses can increasingly become difficult as the number of targets increase [95].

4.3.2 Disorder in bond's stiffness

We now suggest an additional method which takes advantage of disorder effects and hyperstaticity. The concept is to once again involve the 1D rotor chain but now, to also to account for the energy contribution of the small rotations of each rotor. While the *primary* system of a 1D rotor chain carries a degree of polarization b, with spring stiffnesses k_1, the *secondary* system consists of unpolarized spring with stiffness k_2. Since we no longer can take advantage of isostaticity, it is critical to account for the respective bond stiffnesses of the two chains. Those additional bonds contribute to the total energy of the periodic system, made of N sites connected by $2N$ bonds

$$E = \frac{1}{2}\sum_{n=1}^{N} k_1(u_{n+1} - bu_n - e_n)^2 + \frac{1}{2}\sum_{n=1}^{N} k_2(u_n)^2, \tag{4.44}$$

where e_n is the unitay extension corresponding to the swollen bond located at cell n_s. This implies that $e_n = 0$ for all bonds, (except for $n = n_s$). The shape of the mode $u(n) = u_0 z^n$ allows us to use the force balance condition at a site n away from the source and to derive the value of the z mode:

$$\left(1 + b^2 + \frac{k_2}{k_1}\right) u_n - b(u_{n+1} + u_{n-1}) = 0 \tag{4.45}$$

$$\implies z = \frac{1 + b^2 + (k_2/k_1)}{2b} - \frac{1}{2b}\sqrt{(1 + b^2 + k_2/k_1)^2 - 4b^2}. \tag{4.46}$$

We now add limited disorder by weakening only one of the secondary bonds. This creates an interface between two regions of the periodic system. We set that interface at cell $n = 0$, for which and only which the secondary spring stiffness is $k_2 = k_s$. This interface "splits" the decaying mode between a reflected and a transmitted contributions. While this is somehow similar to Fresnel equations for incident electromagnetic waves on a media with different refractive index, one must remember that we do not consider scattering effects (since there's only one direction of motion) but also that

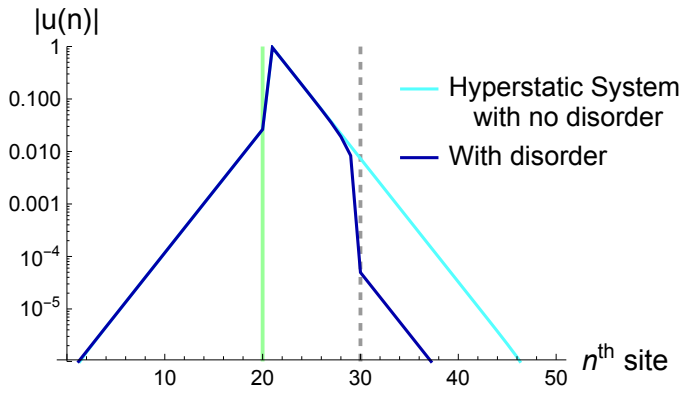

Figure 4.9: Mechanical response in a hyperstatic system with weak secondary springs ($k_2 = 0.02$), compared to the polarized primary system ($k_1 = 1, b = 0.6$) due to swelling of bond at green line. The cyan response is one when there exists no interface of disorder. The blue response occurs when one of the secondary spring (dashed line) is tuned up $k_s = 100$.

here, our study is entirely static (we do not worry for the dynamics of the system). Let's set T, R as the transmission and reflection coefficient of the resulting decaying mechanical mode:

$$\text{for } n \leqslant 0 : u_n = u_0' \left(z^n - Rz^{-n}\right) \tag{4.47}$$

$$\text{for } n > 0 : u_n = u_0' \, T z^n \tag{4.48}$$

We then solve for the value of these coefficients from the system's parameter

$$T = \left(1 + \frac{(k_s - k_2)/k_1}{\sqrt{(1 + b^2 + k_2/k_1)^2 - 4b^2}}\right)^{-1} \tag{4.49}$$

$$R = \left(1 + \frac{\sqrt{(1 + b^2 + k_2/k_1)^2 - 4b^2}}{(k_s - k_2)/k_1}\right)^{-1}, \tag{4.50}$$

which verifies the conservation property

$$T + R = 1, \tag{4.51}$$

meaning the transmission and reflection modes add up to the incident mode. This signifies that there is no dissipation effect as well and that with the proper amount of disorder, the incident mode can decompose entirely into a transmitted or a reflected mode. We study the latter. On figure 4.9, let's first consider a hyperstatic system with relatively weak secondary springs ($k_2 << k_1$). This implies that the the response mode is mostly on the right of the source (green line) due to the degree of polarization of the primary system ($b < 1$). Originally, the system is entirely periodic (cyan). We then add limited disorder by tuning up the spring stiffness of only one secondary spring, at a cell far from the source (dashed line), but on the side of the mechanical response. The result is that the mode is entirely reflected at the interface of disorder (blue):

$$\text{without disorder} \begin{cases} T = 1 \\ R = 0 \end{cases} \quad \text{with disorder} \begin{cases} T = 0.01 \\ R = 0.99 \end{cases} \tag{4.52}$$

While this is usually accomplished with fixed boundary conditions, we demonstrated that disorder can also abruptly stop exponentially decaying mode in the bulk of the system. This complete backscattering effect is often undesirable in mechanical systems [43, 53], but here, we extensively use it to design a domain wall in the bulk that stops the deformations from propagating any further. Unlike other research which often rely on interfaces that separate regions with different topology [3, 6, 70] this 1D chain carries the same topology across the entire system.

Throughout this chapter, we've shown that we can use the topological nature of well established mechanical systems to induce novel responses in more challenging ones and to account for boundary effects in finite size lattices. For example, we've derived how the continuum theory we developed in Chapter 3 [33] can be applied to measure for the error in measurements between the numerically evaluated edge

polarization and its predicted value from Kane and Lubensky's winding number and how those same edge modes decay into the bulk. We then showed that a new mechanical geometric phase can indicate where the mean mechanical response in the bulk of non-ideal systems is and how it can be tuned by changing the system's parameters. Finally, we've shown that disordered effects, while limited, can create exciting mechanical responses in metamaterials such as the presence of soft deformations far from the source via mechanical amplification. We've also seen that disorder effects can serve as an interface which narrows the range of soft deformations within a region of the bulk.

Chapter 5
HIGHER ORDER TOPOLOGICAL SYSTEMS - CORNER MODE

This work heavily relies on our publication as PRB - Rapid Communication: *Controlling the Deformation of Metamaterials: Corner Modes via Topology* [5].

5.1 Introduction

Throughout these past chapters, we've heavily used the Maxwell condition as an argument to derive topological edge modes in 2D lattices. While the breaking of the spatial invariance symmetry determines if a system is polarized, its number of edge modes is given by the Maxwell-Calladine [64] counting of Chapter 2, in particular, that the system must be missing bonds at the boundary in order to exhibit exponentially localized deformations [3]. For those Maxwell systems, we've shown we can simply solve for the zeros of the determinant of the rigidity matrix $\mathbf{R}(\mathbf{z} = e^{i\mathbf{q}})$ to determine zero-energy deformations in wavenumber space.

However, for those lattices that no longer respect the Maxwell condition, the rigidity matrix is no longer square. We've seen we can remediate to that issue by deriving new quantifiable metrics that compute the directional response of hyperstatic systems (Chapter 4), but now, we're interested in a new methodology that accounts for topological modes in higher-dimensional systems.

5.1.1 A new counting argument

Consider a d dimensional systems with $n_{\text{d.o.f}}$ degrees of freedom per cell, where the modes of deformations follow Bloch's theorem [66], those described by $\mathbf{u}(\mathbf{n}) = \mathbf{u}_0 \prod z_i^{n_i}$. We now look to vary n components of the $\mathbf{z}$ vector and to let the $(d-n)$ remaining ones fixed. Given that the modes of deformation within each cell $\mathbf{u}_0$ accounts

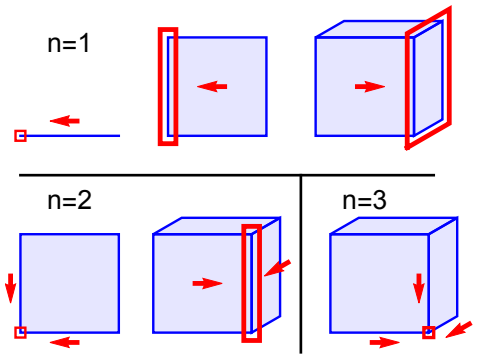

Figure 5.1: Cartoon representation of different systems, all with open boundaries, lying in different dimensions d and with different order n. The top 3 figures represent conventional Maxwell systems ($n = 1$) where an imbalance of the zero modes on the edge results in bulk polarization (arrow). For those with higher-order $n \geqslant 2$, the new Maxwell rigidity results in modes in corners and edges, with new polarized elements on surfaces a dimension higher.

for $n_{\text{d.o.f}}$ variables, there are a total of $n + n_{\text{d.o.f}} - 1$ degrees of freedom, the "-1" term corresponding to the rescaling of deformations $\mathbf{u} \leftrightarrow \alpha\mathbf{u}$ (with $\alpha \in \mathbb{C}^*$) which does not change the nature of our scale-invariant mechanics. On the other hand, we still have n_{con} constraints per cell. We now write what this new Maxwell condition would be, assuming number of degrees of freedom equal number of constraints:

$$n + n_{\text{d.o.f}} - 1 = n_{\text{con}}, \tag{5.1}$$

$$n = n_{\text{con}} + 1 - n_{\text{d.o.f}}. \tag{5.2}$$

Topological modes can exist on surface elements of the system if Eq. (5.2) is satisfied, which we define as the *new counting argument*. For higher-order systems, we refer to the mapping from the $(\mathbf{u}, \mathbf{z})$ configuration space of dimension $n + n_{\text{d.o.f}} - 1$ to the space of n_{con} constraints as the n^{th}*-order Maxwell rigidity*. By setting n of the $\mathbf{z}$ components free, we ensure a mapping between spaces of the same size.

On figure 5.1, we show for different dimensional spaces what a $n = 1, 2, 3$ - order Maxwell system looks like. For the case of $n = 1$, the system is Maxwell: it simply possesses equal number of degrees of freedom and constraints and it is equivalent to

the Kane and Lubensky study of 2014 [6], which in turn, connects with non-Hermitian but square Hamiltonian found in other topological systems [96, 97]. For higher-order systems, we can in fact realize corner or edge modes in 3D systems for example (figure 5.1). It is worth noting that we could also realize higher-order self-stresses in *under-constrained* systems: for those, the order would be given by $n = n_{\text{d.o.f}} + 1 - n_{\text{con}}$ and rather than being open-ended, the boundaries would need to be fixed, to allow for bulk self-stresses to exist. Within this chapter, we will focus on the so-called "checkerboard lattice" which spans over $d = 2$ dimensions and possesses a $n = 2$ - order deformation mode.

5.1.2 Topological degree of the map

We now look for a topological invariant, with the difficulty considered that the space of bulk $|z_i| = 1$ for all i, no longer encloses the space of zero-energy modes. For that reason, we operate over a new element of surface, one higher in dimension than the target space of zero modes. For example, a zero edge mode requires consideration of modes on the attached surfaces (bottom row/second to the left on figure 5.1), while a corner mode can be found by the two adjoining edges (bottom row/first to the left on figure 5.1).

In our configurational space $(\mathbf{u}, \mathbf{z})$, let $\mathcal{B}$ be the region of the zero modes, with dimension n. $\mathcal{B}$ is defined by a set of exponentially localized modes: $0 \leqslant |z_i| \leqslant 1$, for $i = 1, 2, \ldots n$ and is therefore *compact*. In this section and in Appendix C.5, we address how to account for modes localized on the right for example, via a change of basis of the lattice structure. For now, the mapping between the zero modes to the space of constraints $\mathbf{R}(\mathbf{z})\mathbf{u} = \mathbf{e}$ is "square", since the dimensions of the domain and codomain are the same [Eq. (5.1)]. Define J_R as the Jacobian of such map. Like in the Maxwell case and with the winding number of Chapter 2 [Eq. (2.16)], the number of zero modes in $\mathcal{B}$ is given by the number of times the map winds around (or covers) the surrounding boundary $\partial\mathcal{B}$, up to a normalization of the surface area

of the corresponding hypersphere $A_{2n_{\text{con}}-1}$ [5, 98]:

$$N_{\mathcal{B}} = \deg(\mathbf{R}, \mathcal{B}) = A^{-1}_{2n_{\text{con}}-1} \int_{\partial\mathcal{B}} dv_1 \dots dv_{2n_{\text{con}}-1} J_R(\mathbf{v}). \tag{5.3}$$

Because the elements of $\mathbf{z}$ are complex, $\partial\mathcal{B}$ lies over a $2n_{\text{con}}-1$ dimensional manifold. This topological invariant relates the presence of zero modes in n^{th}-order critical systems to nonlinear maps from modes to constraints on the surrounding elements. For example, a corner functions as the "edge" of the two adjoining edges in 2D and the invariant is integrated precisely over these edges. Nevertheless, the bulk structure still matters as it is encoded in the Jacobian J_R. In Appendix C.2, we argue that the considered holomorphic map always have nonnegative degrees and since the homotopy group of spheres to themselves lie in the integers space ($\pi_n(S^n) = \mathbb{Z}$) [75], our invariant does in fact corresponds to the total number of modes.

Eq. (5.3) is only valid when the region of interest $\mathcal{B}$ is compact, for which the boundaries are well defined. For the 2D checkerboard considered in the next section, we're interested in lower left corner modes, therefore $\mathcal{B} : \{|z_1|, |z_2| \leqslant 1\}$. But, if we were instead to look for the lower right corner modes, we would have $\mathcal{B} : \{|z_1| > 1, |z_2| < 1\}$. This invalidates the "compactness" property needed for our theory to be valid. Therefore, to account for the lower right corner modes, we relabel the cell index along the first lattice direction to count from right to left instead. This change of gauge does modify the topological degree of the map, but returns the number of zeros of concern.

5.2 Model Second-Order System: the Deformed Checkerboard

5.2.1 Constraints and the corner mode

To model the general phenomenon of higher-order Maxwell rigidity, we consider the following system: a two-dimensional system with second-order zero mode, which occurs in lattices with one additional constraint per cell beyond the Maxwell condi-

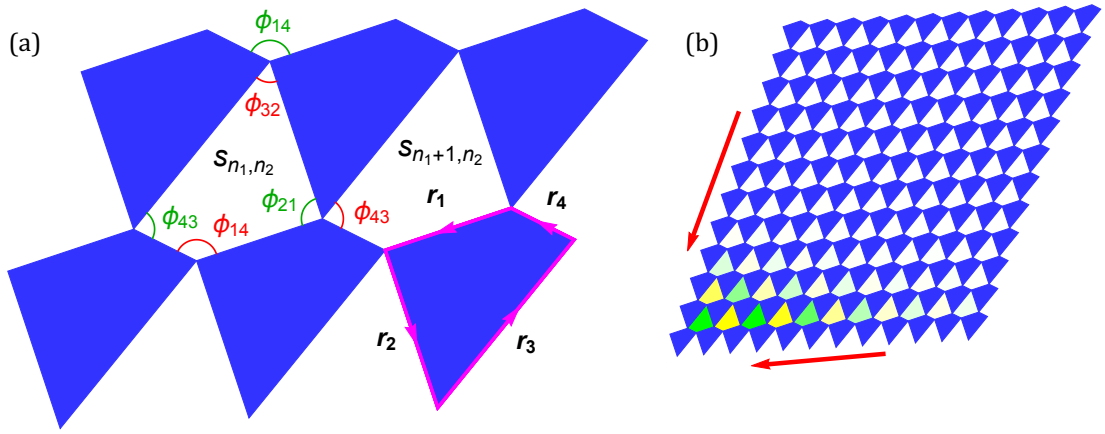

Figure 5.2: (a) Rigid quadrilateral faces are hinged at their vertices and allowed to rotate relative to one another. The faces form a void, which upon rotation of the pieces, is allowed to shear. The edges of the faces are labeled by $\mathbf{r_1}, \mathbf{r_2}, \mathbf{r_3}, \mathbf{r_4}$ and the voids are defined by the four shearing angles: $\phi_{14}, \phi_{21}, \phi_{32}, \phi_{43}$. For the system considered, the zero-energy deformation is exponentially localized in the lower left corner, with green and yellow shading indicating shearing in opposite directions and darker colors hinting at higher amplitudes. This corner mode lies between two topologically polarized edges (red arrows).

tion. Specifically, we offer to study the model of a checkerboard consisting of solid quadrilateral faces joined by free hinges, which form voids in between the pieces (figure 5.2 (a)). As the faces rotate, the voids are allowed to shear. The resulting zero-energy deformation mode ends up in one of the corners of the system, the lower left one (figure 5.2 (b)). While here the existence of the corner mode is given by a counting argument on mechanical stability [Eq. (5.2)], in other topological systems, such as topological insulators, it has been shown that corners support conducting states as well [50], with the difference that the origin of the mode comes down to the breaking of time-reversal symmetry.

The constraint conditions are the following: the solid pieces cannot break and the voids must close. In the sites connected by springs model, the vertices of the faces represent the sites, and the edges, the springs. The constraint conditions do match with our typical definition of a zero-energy deformations (no springs can be stretched). But rather than reason in terms of displacement of sites, we'll use the

shearing angles per void as our free variable. On the other hand, we realize there are two constraint equations per void: that the shearing angle are equal and opposite across a vertex, namely that $\phi_{43} = -\phi_{21}$ and $\phi_{14} = -\phi_{32}$ on figure 5.2 (a).

There are several additional approaches to find the rigidity matrix here (see Appendix C.3). Since, we don't deal with typical displacement of sites, we tend to refer to $\mathbf{R}$ as the *constraint matrix* instead. One of the model is the one we started eluding to: identify the scalar shearing of the voids. Using Bloch's theorem once again, we prove that the shearing mode across all voids $s_{n_1,n_2} = s_0 z_1^{n_1} z_2^{n_2}$ must satisfy the following constraint matrix:

$$\mathbf{R}(z_1, z_2) = \begin{pmatrix} b_1 + a_1\, z_1 \\ \\ b_2 + a_2\, z_2 \end{pmatrix}, \tag{5.4}$$

where a_i, b_i are positive constants of the system (Appendix C.3.3). It is then clear that the zero mode of the system is given by

$$z_1 = -b_1/a_1 \text{ and } z_2 = -b_2/a_2, \tag{5.5}$$

and that the each ratio $|b_i/a_i|$ determines in which corner the mode is. For the system of figure 5.2, both $|b_i/a_i|$ ratios are less than 1. The negative sign here indicates that voids alternatively shrink and expand, indicating that the mode is "antiferromagnetic".

As we explain in details in Appendix C.3.3, we can deform the piece in a way that the a_i constants equal their respective b_i. In particular, we note that if $a_1 = b_1$ and $|b_2/a_2| < 1$ then the mode turns into a bottom edge mode. In such scenario, the constraint matrix is invariant under the reflection $n_1 \to -n_1$. We draw on figure 5.3 how to deform the pieces in order to generate edge (red lines) and bulk modes (intersection of the two red lines). Clearly here for this particular checkerboard system, only

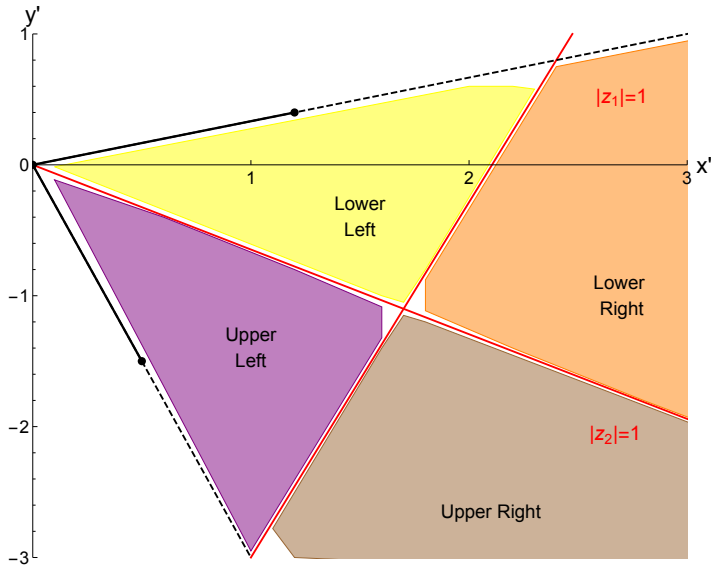

Figure 5.3: Using Appendix C.3.3, we can deform the piece to move the mode around the four corners. Such deformation take place by moving one of the corner of the checkerboard in the (x', y') plane [the right one on the pieces of figure 5.2 (a)] while the remaining three are fixed (black dots). The location of the moving corner of the prototype generates a zero mode computed from the geometries of the system and that is in agreement with the topological degree of the map (shading) [5].

one corner can support the mode at a time; meanwhile electronic conducting states present in quadrupole topological insulators [50] are usually found in all 4 corners simultaneously.

5.2.2 Experimental realization

We realize an experiment prototype corresponding the checkerboard of in figure 5.2 (b), where the mode is exponentially localized in the lower left corner. We cut a 3.2 mm thick acrylic sheet using a high-precision laser cutter (Trotec Speedy 300 from the Montgomery Machining Mall of The George W. Woodruff School of Mechanical Engineering) and assemble a 4×4 prototype of ~ 1 cm pieces, connected by nylon rivets to form the checkerboard system of figure 5.4 (a). We then use a digital camera to track the motion of the rivets (the vertices) as we impose a mode of deformation from the lower left end of the prototype. We then analyze the shearing vector of all the 3×3 voids and compare it with its predicted value $\hat{s}_{\mathrm{T}}$ [figure 5.4 (c)].

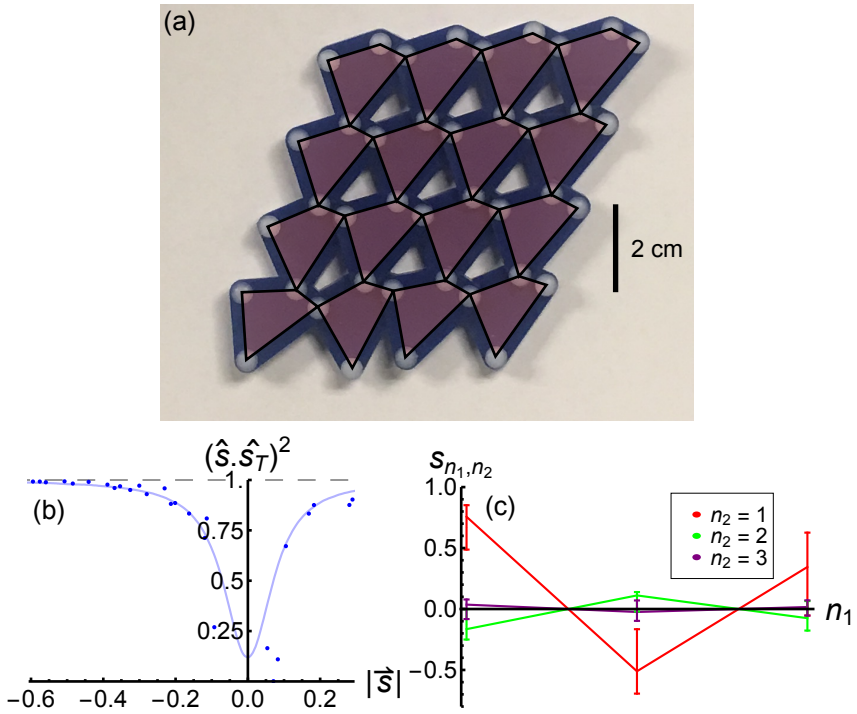

Figure 5.4: (a) Prototype of the checkerboard lattice. (b) Computation of the topological character χ_{T} over a broad range of amplitudes: the topological corner mode $\hat{s}_{\mathrm{T}}$ is dominant. (c) Shape of the shearing mode in cells (n_1, n_2) with $1 \leqslant n_1, n_2 \leqslant 3$ over the same range amplitude. The experimental results are indicated by error bars, plotted along the theoretical predictions (solid lines in red, light green and dark green).

In the interest of deriving a thorough data analysis of our experiment results, we also derive the topological character $\chi_{\mathrm{T}} \equiv (\hat{s} \cdot \hat{s}_T)^2$, that we plot as a function of the mode amplitude [figure 5.4 (b)]. The theoretical blue line is computed assuming a static error imputed to all data points (such as poor placement of the camera) and assuming errors normally distributed across all 9 voids. We smoothen such curve and see that the experimental data (the blue points) fits well with our predicted character. While it is true that for small amplitudes, practical effects of friction and static disorder may hamper on the corner mode, we see that for large ones, the linear topological theory tests well against nonlinearities due to large range of shearing motions. One can even claim that a mechanical amplifier is observed, with shearing angles ranging from -0.43 to 0.31 radians in the most deformed void (the lower left

one) and compare it with the effects predicted in disordered 1D rotor chains (see figure 4.8 of section 4.3). This opens the route to more printed topological systems, such as those realized in 3D [42], though the extra dimension adds a level of complexity to realize those systems experimentally.

5.3 Conclusion

Throughout this chapter, we've focused on over-constrained mechanical lattices that yet possess zero-energy boundary modes described by a higher-order topological invariant. Similarly to Maxwell systems [6], these modes are protected by a new counting argument, which accounts for inter-cell motions (z_i) as degrees of freedom and which returns the dimensionality of the surface element that contains the zero-energy deformations. The number of these zero modes is then given by the topological degree of a constraint map evaluated on the boundary of that surface element. We prove that such topological linear theory is robust against nonlinearities and weak disorder by testing our deformation modes on a experimental prototype. We show that the bulk structure, in particular the geometries of the bulk elements, govern where the mode ends up, most likely in the corner, but possibly on the edges or in the bulk.

This work can potentially by extended to three-dimensional systems, which already have seen exciting features such as programmability of deformations via topology [42] or 2D boundary effects in critical systems [99] that we are familiar with. Even though our focus is typically on displacement modes that result in zero-energy cost to the system, we can on principle focus instead on states of self-stress, for which our higher-order topological study could be realized if one were to exchange the roles of vertices and faces following Maxwell-Cremona dual [100, 101].

Since our corner modes have been shown to extend realistically in the nonlinear regime and despite the presence of disorder, we can also imagine such higher-order theory (which relies on the counting argument) to be expanded to other nonlinear me-

chanical systems, or even those that lack perfect long-range order. We also note that this higher-order topological theory isn't restrained to soft mechanical deformations. In fact, other topological multipoles have been extensively observed in topological insulators [50, 102, 103], but their origin differ from ours. For spin systems in isostatic lattices [104], those still rely on the counting argument and topological winding numbers and we can assume that systems could benefit from higher-order topological effects.

Chapter 6
CONCLUSION

Throughout this document, we've unfolded how topological states of matter directed the presence of novel mechanical deformations in flexible metamaterials. This fascinating mathematical tool known as topology, which in the context of these mechanical systems emerge from their geometrical structures, can control the nature of their distortion on the boundaries and their response to mechanical perturbations. While it is likely that non-topological systems can induce similar mechanism of deformations, by developing a topological linear theory on periodic systems, our analytical and experimental results are robust and protected against nonlinearities and disorder. In general, our models consist in (but are not limited to) analyzing and deriving a topological invariant from the bulk structure of the material and connecting it with the physics happening on the boundaries. The goal of this dissertation is to expand the study on topological modes in isostatic lattices introduced by Kane and Lubensky in 2014 [6] to a greater variety of flexible systems, such as those governed by micromorphic continuum elasticity, those with weak disorder and those that are no longer critically coordinated. I believe that the research work I conducted during my time at Georgia Tech fulfilled that goal via rigorous and complete studies, two of them being published in peer-reviewed journals [5, 33].

First, we've introduced a new method that covers how a microstructure responds to imposed macroscopic strain fields [33]. We've shown that the key element that breaks spatial inversion symmetry are the gradients of the imposed strain and that the topological zero-energy boundary modes manifest after microscopic relaxation. The expressions for the energetic contributions of the bulk and the surface are consistent with the bulk-boundary correspondence established in critically coordinated

systems and in fact, we've shown that the surface energetic term determines which boundary contains the zero-energy deformations, if any. Mathematically, a new topological invariant is introduced and computes the relative number of zero modes on opposite boundaries. Unlike previous topological studies where the invariant is defined across the Brillouin Zone, here, it is determined over sets of long-wavelength modes. This new invariant, also known as polarization, can be computed not only within the lattice vector directions but over a continuum range of directions through the material. Depending on the orientation of the material's interface with the surrounding environment, we've shown that edge modes can decay into the bulk over long distances, much larger than the size of the unit cell. Even though we used a microstructure to support the energetic costs of the applied strains, this theory doesn't require such foundation: it only needs equal numbers of degrees of freedom and energetic constraints and also that the map between the two break spatial inversion symmetry.

Second, we've also looked to expand the work done on directional response in the bulk established by Rocklin [4] to systems more challenging in nature. For example, we derived a polarization metric that describes the distribution of boundary modes in finite size systems and proved that it matched with the long-wavelength modes of the continuum limit model. Rather than limiting our work to periodic critically coordinated lattices, we've expanded our study to complex structures — including those well above the Maxwell point and those with defects — and yet still used topological effects to derive their mechanical response. In particular, a new geometrical phase called the response position was derived to indicate the mean directional response due to an imposed stress and was used eventually to demonstrate inversion of directionality via hyper-tuning of a metamaterial's parameters. We also showed that implementing disorder via a perturbative method consisting of adding, removing or weakening bonds in one dimensional lattices can create amplifier mechanism and

targeted mechanical response upon swelling of one or multiple bonds.

Finally, we've shown that zero-energy modes in higher order topological systems can manifest on particular surface elements of the boundary [5]. Like Maxwell systems, the dimensionality of the space of these modes and the coordination number per cell are related via a new counting argument. We explored in particular the corner modes of two-dimensional higher-order Maxwell systems. The topological degree of a constraint map evaluated on the boundary of the space of deformation indicates the total number of zero-energy deformations. We showed that via control of the bulk structure and of its geometry, we can move the modes between corners. We tested and proved the success of our linear theory against disorder and nonlinearities, by realizing an experimental prototype corresponding to a checkerboard with corner modes. This theory can be extended to higher-order systems lying in higher-dimensional spaces and even to states of self-stresses rather than deformations, so long as boundary requirements are met.

Appendix A
CONTINUUM LIMIT

A.1 Effects of Strains on Microstructure

In our lattice model, we define $\mathbf{r}$ as the position of the center of the cell, $\mathbf{p}$ the middle of the bond with respect to the center of the cell and $\mathbf{b}$ the vector from one end of the bond to the other. Let's now consider a displacement field which leads to an additional end-to-end displacement. On figure 3.1:

$$\delta\mathbf{u} = \mathbf{u}_2 - \mathbf{u}_1 = \mathbf{u}(\mathbf{r} + \mathbf{p} + 1/2\,\mathbf{b}) - \mathbf{u}(\mathbf{r} + \mathbf{p} - 1/2\,\mathbf{b}) \tag{A.1}$$

Assuming smooth and small displacements of the sites attached to the bond compared to the cell overall, we can Taylor expand each displacement about the center of the cell:

$$\mathbf{u}_1 = \mathbf{u}(\mathbf{r}) + (\mathbf{p} - 1/2\,\mathbf{b})_k \nabla_k \mathbf{u}(\mathbf{r}) + \frac{1}{2}(\mathbf{p} - 1/2\,\mathbf{b})_{k_1}(\mathbf{p} - 1/2\,\mathbf{b})_{k_2} \nabla_{k_1}\nabla_{k_2}\mathbf{u}(\mathbf{r}) \tag{A.2a}$$

$$\mathbf{u}_2 = \mathbf{u}(\mathbf{r}) + (\mathbf{p} + 1/2\,\mathbf{b})_k \nabla_k \mathbf{u}(\mathbf{r}) + \frac{1}{2}(\mathbf{p} + 1/2\,\mathbf{b})_{k_1}(\mathbf{p} + 1/2\,\mathbf{b})_{k_2} \nabla_{k_1}\nabla_{k_2}\mathbf{u}(\mathbf{r}) \tag{A.2b}$$

$$\implies \delta\mathbf{u} = b_k \nabla_k \mathbf{u}(\mathbf{r}) + \frac{1}{2}\left(p_{k_1} b_{k_2} + p_{k_2} b_{k_1}\right) \nabla_{k_1}\nabla_{k_2}\mathbf{u}(\mathbf{r}) \tag{A.2c}$$

$$\implies \delta u_j = b_i \left(1 + p_k \partial_k\right) \partial_i u_j \tag{A.2d}$$

This last term contains the gradient of displacement which we use to find the extension

of the bond, linearly:

$$e = \hat{b} \cdot \delta\mathbf{u} = \frac{b_j}{|\mathbf{b}|}\delta u_j \tag{A.3a}$$

$$= \frac{b_j b_i}{|\mathbf{b}|}\left(1 + p_k\partial_k\right)\partial_i u_j \tag{A.3b}$$

$$= \frac{b_i b_j}{|\mathbf{b}|}\left(1 + p_k\partial_k\right)\epsilon_{ij} \tag{A.3c}$$

Note, this operation is invariant under the inversion of indices i, j, confirming that we can express our results purely in term of symmetrized strain.

A.2 Energy and Surface Terms

In this section, we break down the total energy of our system into a bulk and surface terms, using the springs extension formula of Eq. (3.1c).

$$E = \frac{1}{2}\sum_m \int d^d\mathbf{r}\, e_m(\mathbf{r}) e_m(\mathbf{r}), \tag{A.4a}$$

$$e_m(\mathbf{r}) = \frac{b_i^m b_j^m}{|\mathbf{b}^m|}\left(1 + p_k^m\partial_k\right)\epsilon_{ij}(\mathbf{r}). \tag{A.4b}$$

Which leads to:

$$E = \frac{1}{2}\sum_m \int d^d\mathbf{r}\, \frac{b_i^m b_j^m b_k^m b_l^m}{|\mathbf{b}^m|^2}\left[(1 + p_\alpha^m\partial_\alpha)\epsilon_{ij}(\mathbf{r})\right] \times \left[(1 + p_\beta^m\partial_\beta)\epsilon_{kl}(\mathbf{r})\right] \tag{A.5a}$$

$$= \frac{1}{2}\sum_m \frac{b_i^m b_j^m b_k^m b_l^m}{|\mathbf{b}^m|^2}\left(\int d^d\mathbf{r}\left[\epsilon_{ij}(\mathbf{r})(\mathbf{p}_m\cdot\nabla)\epsilon_{kl}(\mathbf{r}) + \epsilon_{kl}(\mathbf{r})(\mathbf{p}_m\cdot\nabla)\epsilon_{ij}(\mathbf{r})\right]\right.$$

$$\left. + \int d^d\mathbf{r}\,\left[\epsilon_{ij}(\mathbf{r})\epsilon_{kl}(\mathbf{r}) + (\mathbf{p}_m\cdot\nabla)\epsilon_{ij}(\mathbf{r})\,(\mathbf{p}_m\cdot\nabla)\epsilon_{kl}(\mathbf{r})\right]\right) \tag{A.5b}$$

The second term of Eq. (A.5b) is evaluated in the bulk and it can't be simplified any further. However, we use the divergence theorem to re-write the first term and

evaluate it on the surface:

$$E_s = \frac{1}{2}\sum_m \frac{b_i^m b_j^m b_k^m b_l^m}{|\mathbf{b}^m|^2}\,\mathbf{p}_m \cdot \left(\int d^d\mathbf{r}\,\nabla(\epsilon_{ij}(\mathbf{r})\epsilon_{kl}(\mathbf{r}))\right) \tag{A.6a}$$

$$= \frac{1}{2}\sum_m \int_{\text{surface}} d^{d-1}\mathbf{r}\frac{b_i^m b_j^m b_k^m b_l^m}{|\mathbf{b}^m|^2}\,(\mathbf{p}_m \cdot \mathbf{n})\,\epsilon_{ij}(\mathbf{r})\epsilon_{kl}(\mathbf{r}). \tag{A.6b}$$

The total energy is then:

$$E = E_s + E_b \tag{A.7a}$$

$$= \frac{1}{2}\int_{\text{surface}} d^{d-1}\mathbf{r}\,\sum_m \frac{b_i^m b_j^m b_k^m b_l^m}{|\mathbf{b}^m|^2} p_m^\alpha n_\alpha\,\epsilon_{ij}\epsilon_{kl}$$

$$+ \frac{1}{2}\int d^d\mathbf{r}\left[\sum_m \frac{b_i^m b_j^m b_k^m b_l^m}{|\mathbf{b}^m|^2}\,\epsilon_{ij}\epsilon_{kl} + \sum_m \frac{b_i^m b_j^m b_k^m b_l^m}{|\mathbf{b}^m|^2}\,(p_m^\alpha \partial_\alpha \epsilon_{ij})\,(p_m^\beta \partial_\beta \epsilon_{kl})\right] \tag{A.7b}$$

which we write in terms of the following elastic moduli, as done in section 3.3:

$$A_{ijkl} = \sum_m \frac{b_i^m b_j^m b_k^m b_l^m}{|\mathbf{b}^m|^2} \tag{A.8a}$$

$$B_{ijkl}^\alpha = \sum_m \frac{b_i^m b_j^m b_k^m b_l^m}{|\mathbf{b}^m|^2} p_m^\alpha \tag{A.8b}$$

$$D_{ijkl}^{\alpha\beta} = \sum_m \frac{b_i^m b_j^m b_k^m b_l^m}{|\mathbf{b}^m|^2} p_m^\alpha p_m^\beta \tag{A.8c}$$

$$\implies E = \frac{1}{2}\int_{\text{surface}} d^{d-1}\mathbf{r}\;\; n_\alpha B_{ijkl}^\alpha \epsilon_{ij}\epsilon_{kl}$$

$$+ \frac{1}{2}\int d^d\mathbf{r}\left[A_{ijkl}\epsilon_{ij}\epsilon_{kl} + D_{ijkl}^{\alpha\beta}(\partial_\alpha\epsilon_{ij})\,(\partial_\beta\epsilon_{kl})\right]. \tag{A.8d}$$

Each of the elastic moduli from Eq. (A.8) is invariant under permutations of either their lower or their upper indices. We evaluate those numerically in table A.1 for the system studied in figure 3.2.

These elastic moduli relate with the initial rigidity map covered in section 3.2. A main contribution to this work is the derivation of a new rigidity map, which alleviate unbalanced forces in the system. While it is more challenging, one could repeat this

(i,j,k,l)	A_{ijkl}	$(B^x_{ijkl},\, B^y_{ijkl})$	$(D^{xx}_{ijkl},\, D^{xy}_{ijkl},\, D^{yy}_{ijkl})$
(x,x,x,x)	3.21878	(0.419412, -0.387303)	(0.358676, -0.0566132, 0.0893519)
(x,x,x,y)	-0.374777	(-0.167225, 0.0139916)	(0.110746, 0.00195441, 0.0193136)
(x,x,y,y)	0.621217	(-0.040412, -0.100059)	(0.216224, 0.0786884, 0.0891775)
(x,y,y,y)	0.274585	(-0.607169, -0.25146)	(0.312016, 0.377231, 0.178096)
(y,y,y,y)	2.94237	(-0.342389, -2.09884)	(2.14663, 0.16367, 1.63641)

Table A.1: We evaluate the energy moduli of the system considered in figure 3.2, lying in the two-dimensional (xy) plane. Each elastic moduli is invariant under permutations of the i,j,k,l indices.

derivation process to find the elastic moduli post-relaxation instead.

A.3 Energy Terms in One Dimension

The constraint equations of the 1D rotor chain can be written as

$$e_n = a u_{n+1} - (a+b) u_n + b u_{n-1}. \tag{A.9}$$

Assuming Bloch's theorem, $u_n \sim z^n$, therefore, a zero-energy mode satisfies the following condition

$$az - (a+b) + b/z = 0 \tag{A.10}$$

We find the two roots to this equations are either $z = 1$ (uniform translation mode) or $z = b/a$ which indicates the edge mode is exponentially localized on the left (if $b < a$) or on the right (if $b > a$).

We also prove that the potential energy of this same 1D rotor system studied in the nonlinear regime — check Ref. [76], Eq. [S5] — which depends on a displacement field $u(x)$ and the system's constants $\bar{u}, K, a$, can be re-written in the limit of small displacements (linear limit):

$$V\left[u(x)\right] = \frac{K}{2}\Big[\left(\bar{u}^2 - u(x)^2\right) + \frac{a^2}{2}\frac{du(x)}{dx}\Big]^2 \tag{A.11}$$

Using $f[u(x)] = \bar{u}^2 - u(x)^2$, do a Taylor-expansion around $\bar{u}$:

$$f[u(x)] = f[\bar{u}] + f'[u]_{u=\bar{u}}\,(u - \bar{u}) \tag{A.12a}$$

$$= -2\bar{u}\,(u - \bar{u}) \tag{A.12b}$$

which we plug back into Eq. (A.11):

$$V\,[u(x)] = \frac{K}{2}\Big[\,-2\bar{u}\,(u - \bar{u}) + \frac{a^2}{2}\frac{d\,(u(x) - \bar{u})}{dx}\Big]^2 \tag{A.13a}$$

$$= 2K\bar{u}^2\Big[\,(u - \bar{u}) - \frac{a^2}{4\bar{u}}\frac{d\,(u(x) - \bar{u})}{dx}\Big]^2 \tag{A.13b}$$

which has the same form as Eq. (3.11b) if $u - \bar{u} \to u'(x)$.

A.4 New Winding Number

As described in section 3.6, we relate the existence of zero-energy boundary modes that exist in the wavenumber complex plane with the system's bulk that consists of real wavenumbers. The key idea is to draw a contour (figure 3.3) which encloses all zeroes of interest close to the origin of the complex plane and ignore those non-physical. For the sake of argument, we implicitly ignore dimensions of length and treat our quantities as pure numbers. As we explain in the main [Eq. (3.26)], the long-wavelength zeros of interest have approximately magnitude ϵ [$\mathrm{Re}(\mathbf{q}) \approx \epsilon$ and $\mathrm{Im}(\mathbf{q}) \approx \epsilon^2$] while the fictitious, undesirable ones have magnitude $\epsilon^0 = 1$. We recall that zeros in the upper (lower) half-plane correspond to modes on the left (right) edge.

We now look to evaluate how the dismissal of the curved contribution of the contour (dashed lines on figure 3.3) creates an error that is negligible and that we recover the result given in the main text. Without loss of generality, let's consider the

error associated with the presence of one zero only. Let's define the complex function

$$f(z) = z - z_0, \tag{A.14}$$

with $|z_0| \approx \epsilon$ and let's find its change in phase from the integral. We deal with a contour of the form $z = re^{i\theta}$ with θ going from 0 to either π or $-\pi$, and with $\epsilon \ll r \ll 1$. We find that the contribution from the dashed arcs due to the long-wavelength modes are

$$\text{arc contribution on long-wavelength ZM } z_0 = 2\,\text{Im}\,\log\left|\frac{r+z_0}{r-z_0}\right|. \tag{A.15}$$

Per Eq. (3.26), we know our zeros have real part $O(\epsilon)$ and imaginary parts $O(\epsilon^2)$, therefore, following a simple expansion of the form $\log(1+x) = x$, we find that the contribution from the arcs is of order $O(\epsilon^2/r)$. Meanwhile, let's find the error associated with the presence of the spurious mode when we integrate over the bulk modes:

$$\text{bulk contribution on short-wavelength ZM } z_0 = 2\,\text{Im}\,\log\left|\frac{z_0-r}{z_0+r}\right|, \tag{A.16}$$

which turns out to be of order $O(r)$. In summary:

$$|z_0| \ll r \implies \text{error} \approx \epsilon^2/r \tag{A.17a}$$

$$|r| \ll 1 \implies \text{error} \approx r \tag{A.17b}$$

We see that our new winding number carries two errors from the negligence of the arcs and the presence of fictitious modes. Our goal is to minimize both, by picking a radius for the contour that lies intermediate between the two regimes $O(\epsilon)$ and $O(1)$. The natural choice is to pick $r = \epsilon^{1/2}$, but more aggressive approaches can pick

$r = \epsilon^{3/4}, \epsilon^{.99}$, which could be needed to accurately represent the polarization around a topological transition. Even though our system includes multiple zeroes all at once, the order of error remains unchanged from Eq. (A.17) and therefore Eq. (3.30) of the main is mathematically justified.

A.5 Soft Directions, Length Scales and Choice of Basis

This section has objective to derive the relationships between the multiple wave vector bases we introduce in the main. We start with a simple Cartesian basis $(\hat{q}_x, \hat{q}_y)$; afterwards, we derive a rotated version thereof in order to compute for polarization in a varying normal direction $\hat{q}_n$ and it's corresponding tangential component $\hat{q}_t$. Finally, as we've introduced the concept of *soft directions*, we define two non-orthogonal vectors $(\hat{q}_+, \hat{q}_-)$ and use the α's paramaters of Eq. (3.34) to unfold their mathematical expression:

$$\hat{q}_\pm = \frac{1}{\sqrt{1+\alpha_\pm^2(\theta)}} \left(\alpha_\pm(\theta)\hat{q}_n + \hat{q}_t\right). \tag{A.18}$$

As discussed in the main text, let's consider a boundary mode with component q_t along the tangent direction. In the $(\hat{q}_n, \hat{q}_t)$ basis, let's express what the zero mode "+" looks like, given its form up to second order [Eq. (3.34)]:

$$\begin{cases} \mathbf{q} = q_n\hat{q}_n \ + \ q_t\hat{q}_t \\ q_n = \alpha_\pm(\theta)q_t + i\beta_+(\theta)q_t^2. \end{cases} \implies \mathbf{q} = q_t\left(\alpha_+(\theta)\hat{q}_n + \hat{q}_t\right) + i\beta_+(\theta)q_t^2\hat{q}_n, \tag{A.19}$$

From Eq. (A.18), we recognize that $\hat{q}_+ \cdot \hat{q}_t = 1/\sqrt{1+\alpha_+^2(\theta)}$. Expressing the zero mode in this form explicitly, we may write:

$$\mathbf{q} = q_t\sqrt{1+\alpha_+^2(\theta)}\,\hat{q}_+ \ + \ i\beta_+(\theta)q_t^2\hat{q}_n \tag{A.20a}$$

$$= \frac{q_t}{\hat{q}_+ \cdot \hat{q}_t}\hat{q}_+ \ + \ i\beta_+(\theta)q_t^2\hat{q}_n, \tag{A.20b}$$

While this expression may seem weird as it involves two directions from two different bases, in reality it isn't: it allow us to easily express what a zero mode is if it lies over the + direction to first order and what the nature of its decay along $\hat{r}_n$ is. A few steps are needed to obtain Eq. (3.37):

1. For it to be a zero mode, the mode must carry a second order correction along $\hat{q}_-$ which statisfies the zero-energy condition

$$A''_{1,1}q_+q_- + i(A''_{3,0}q_+^3 + A''_{2,1}q_+^2q_- + A''_{1,2}q_-q_+^2 + A''_{0,3}q_-^3) = 0, \tag{A.21}$$

   which is the form of the determinant $\det(\mathbf{R}(\mathbf{q}))$ in the $(\hat{q}_+, \hat{q}_-)$ basis. This gives us what the second order correction is.

2. Additionally, we must be able to decompose $\hat{q}_n$ into a combination of $\hat{q}_+, \hat{q}_-$ and account for the condition that we want the mode to resemble q_t along the tangent direction

In summary, we find that the normal term can be re-written and that the wave vector is given by:

$$\mathbf{q}_+ = \frac{q_t}{\hat{q}_+ \cdot \hat{q}_t}\hat{q}_+ \; + \; iq_t^2\frac{A''_{3,0}}{A''_{1,1}}\frac{|\hat{q}_+, \hat{q}_-|}{(\hat{q}_+ \cdot \hat{q}_t)^3}\hat{q}_n. \tag{A.22}$$

Since $(\hat{q}_n, \hat{q}_t)$ form an orthonormal basis, we can use $q_+ = (\hat{q}_+ \cdot \hat{q}_t)q_t$ to also express what a zero mode looks like in terms of the coordinates in the soft basis:

$$\mathbf{q} = q_+\hat{q}_+ \; + \; iq_+^2\frac{A''_{3,0}}{A''_{1,1}}\frac{|\hat{q}_+, \hat{q}_-|}{\hat{q}_+ \cdot \hat{q}_t}\hat{q}_n, \tag{A.23a}$$

$$= q_+\hat{q}_+ \; + \; iq_+^2\frac{A''_{3,0}}{A''_{1,1}}\frac{\sin(\theta_+ - \theta_-)}{\sin(\theta - \theta_+)}\hat{q}_n \tag{A.23b}$$

Finally, as we explain in the main, we now want to re-write the zero mode in terms of the length parameters of the system and of the imposed bond. Consider λ as

the wavelength of the mode on the boundary ($\lambda = 2\pi/q_t$) and from a dimensional analysis, we can use $\mathbf{l}_1$, the first lattice vector, to rewrite the term $A''_{3,0}/(A''_{1,1}|\mathbf{l}_1|)$ as a dimensionless quantity. That way, Eq. (3.38) can be re-written as:

$$\mathbf{q} = \frac{2\pi}{\lambda \sin(\theta_+ - \theta)}\hat{q}_+ + i\left(\frac{2\pi}{\lambda}\right)^2 \frac{A''_{3,0}}{A''_{1,1}} \frac{\sin(\theta_+ - \theta_-)}{\sin^3(\theta - \theta_+)}\hat{q}_n, \tag{A.24}$$

and the decay length through the bulk as:

$$\left[\frac{\zeta_+}{|\mathbf{l}_1|}\right] = \left[\frac{\lambda}{2\pi|\mathbf{l}_1|}\right]^2 \left[\frac{|\mathbf{l}_1|A''_{1,1}}{A''_{3,0}}\right] \frac{\sin^3(\theta - \theta_+)}{\sin(\theta_+ - \theta_-)}. \tag{A.25}$$

Appendix B
MECHANICAL RESPONSE

B.1 Displacement and Pseudo-Inverse

As discussed in Chapter 2, the force balance modes are given in real space by:

$$\mathbf{R}^T\mathbf{K}(\mathbf{R}\mathbf{u} - \mathbf{e}_{\text{ext}}) = 0 \tag{B.1}$$

B.1.1 Uniform spring stiffness

For now, let's assume that the stiffness matrix is the identity $\mathbf{K} = \mathbf{I}$. We find the pseudo-inverse the following way:

$$\mathbf{R}^T(\mathbf{R}\mathbf{u} - \mathbf{e}_{\text{ext}}) = 0 \tag{B.2a}$$

$$\implies \mathbf{D}\mathbf{u} = \mathbf{R}^T\mathbf{e}_{\text{ext}} \tag{B.2b}$$

$$\implies \mathbf{u}(\mathbf{R}, \mathbf{I}) = \mathbf{D}^{-1}\mathbf{R}^T\mathbf{e}_{ext}. \tag{B.2c}$$

We recognize here the pseudo-inverse of Eq. (4.23) for $\mathbf{K} = \mathbf{I}$. Using the definition of the *Moore-Penrose inverse*, for systems we consider — those with no redundant constraints — then $\mathbf{R}$ has full rank (and is yet likely non-square) and:

$$\mathbf{R}^{-1,g} = \left(\mathbf{R}^T\mathbf{R}\right)^{-1}\mathbf{R}^T = \mathbf{D}^{-1}\mathbf{R}^T \tag{B.3a}$$

$$\implies \mathbf{u}(\mathbf{R}, \mathbf{I}) = \mathbf{D}^{-1}\mathbf{R}^T\mathbf{e} = \mathbf{R}^{-1,g}\mathbf{e} \tag{B.3b}$$

The key here is to recognize that the dynamical matrix is invertible. This method is equivalent with getting the force balance modes from the dynamical matrix.

The set of displacement $u(\mathbf{R}, \mathbf{I})$ is of interest, since it describes those found in Maxwell systems with square rigidity map (proof in subsection B.2.3). We can even argue that for Maxwell systems, the rigidity matrix is invertible and its pseudo-inverse is simply the inverse. For the sake of notation, we will keep using the label "pseudo-inverse" regardless of context.

B.1.2 Non-uniform spring stiffness system

In systems with non-uniform spring stiffness, the force balance modes still satisfy $\mathbf{R}^T\mathbf{K}(\mathbf{R}\mathbf{u} - \mathbf{e}_{ext}) = 0$, but let's now define

$$\mathbf{R}' = \mathbf{K}^{1/2}\mathbf{R} \text{ and } \mathbf{e}'_{\text{ext}} = \sqrt{\mathbf{K}}\mathbf{e}_{\text{ext}} \tag{B.4}$$

Then, solving equation (B.2a) and using Eq. (B.4) reads:

$$\mathbf{R}'^T(\mathbf{R}'\mathbf{u} - \mathbf{e}'_{\text{ext}}) = 0 \tag{B.5a}$$

$$\implies \mathbf{u} = \mathbf{R}'^{-1,g}\mathbf{e}'_{ext}, \tag{B.5b}$$

which means that for a system obeying rigidity $\mathbf{R}$ and spring stiffnesses $\mathbf{K}$, the displacement $u(\mathbf{R}, \mathbf{K})$ from the bond swelling $\mathbf{e}' = \sqrt{\mathbf{K}}\mathbf{e} = \sqrt{k_j}\hat{e}_j$ is then:

$$u(\mathbf{R}, \mathbf{K}) = \left(\mathbf{K}^{1/2}\,\mathbf{R}\right)\,\sqrt{\mathbf{K}}\mathbf{e}_{\text{ext}} \tag{B.6}$$

For the rest of the derivations of this Appendix, we will assume we deal with uniform spring stiffness. However, one must remember that in order to return to an expression involving the spring stiffnesses, we just need to plug in $\mathbf{R}^{-1,g} \to (\mathbf{K}\mathbf{R})^{-1,g}\sqrt{k_j}$, the same way Eq. (B.3) $\to$ Eq. (B.6).

B.1.3 Significance for the displacements $u_i^j(\mathbf{n})$

Now that we have a framework for the pseudo-inverse of the rigidity map, let's investigate how it shapes up the displacement mode. It is worth noting that the rigidity

map is translationally invariant. This means that the bond swollen j at $\mathbf{r}'$ returns a displacement of site i at location $\mathbf{r}$ is given by:

$$R_{ij}(\mathbf{r},\mathbf{r}') = R_{ij}(\mathbf{r}-\mathbf{r}') \implies u_i^j(\mathbf{r}) = R_{ij}^{-1,g}(\mathbf{r}-\mathbf{r}'). \tag{B.7}$$

Which in wavenumber space means:

$$u_i^j(\mathbf{q}) = R_{ij}^{-1,g}(\mathbf{q},\mathbf{q}')e_j(\mathbf{q}') = R_{ij}^{-1,g}(\mathbf{q}), \tag{B.8}$$

because the rigidity in reciprocal space is diagonal and the stretch has unit magnitude. Using Bloch's theorem, the displacement response can be expressed via it's Fourier transform

$$u_i^j(\mathbf{n}) = \frac{1}{(2\pi)^{N/2}}\int d\mathbf{q}\, u_i^j(\mathbf{q})e^{i\mathbf{q}\cdot\mathbf{n}} \tag{B.9a}$$

$$= \frac{1}{(2\pi)^{N/2}}\int d\mathbf{q}\, R_{ij}^{-1,g}(\mathbf{q})e^{i\mathbf{q}\cdot\mathbf{n}} \tag{B.9b}$$

$$\implies |u_i^j(\mathbf{n})|^2 = \frac{1}{(2\pi)^{N}}\int d\mathbf{q}d\mathbf{q}'\, R_{ij}^{-1,g}(\mathbf{q})R_{ij}^{-1,g}(\text{-}\mathbf{q}')e^{i(\mathbf{q}-\mathbf{q}')\cdot\mathbf{n}} \tag{B.9c}$$

assuming N to be the number of dimensions.

B.2 Response Position

In Eq. (4.20) we have

$$\mathbf{RP} = \frac{\sum_{ij\mathbf{n}}\ |u_i^j(\mathbf{n})|^2(\mathbf{r}_i + \underline{\mathbf{l}}\cdot\mathbf{n} - \mathbf{r}_j)}{\sum_{ij\mathbf{n}}\ |u_i^j(\mathbf{n})|^2} \tag{B.10}$$

B.2.1 In wavenumber space

Assuming the system being infinitely large, we can turn the sum over the cells $\sum_{\mathbf{n}}$ into an integral $\int d\mathbf{n}$. Treating the numerator of **RP** first:

$$\mathbf{RP}_{num} = \frac{1}{(2\pi)^N} \sum_{ij} \int d\mathbf{q} d\mathbf{q}' d\mathbf{n}\; R_{ij}^{-1,g}(\mathbf{q}) R_{ij}^{-1,g}(\text{-}\mathbf{q}')(\mathbf{r}_i - \mathbf{r}_j + \underline{\mathbf{l}} \cdot \mathbf{n}) e^{i(\mathbf{q}-\mathbf{q}')\cdot\mathbf{n}} \quad \text{(B.11a)}$$

$$= \frac{1}{(2\pi)^N} \sum_{ij} \int d\mathbf{q} d\mathbf{q}' R_{ij}^{-1,g}(\mathbf{q}) R_{ij}^{-1,g}(\text{-}\mathbf{q}')(\mathbf{r}_i - \mathbf{r}_j) \left(\int d\mathbf{n}\; e^{i(\mathbf{q}-\mathbf{q}')\cdot\mathbf{n}} \right)$$

$$+ \frac{1}{(2\pi)^N} \sum_{ij} \int d\mathbf{q} d\mathbf{q}' R_{ij}^{-1,g}(\mathbf{q}) R_{ij}^{-1,g}(\text{-}\mathbf{q}')\, \underline{\mathbf{l}} \cdot \left(\int d\mathbf{n}\; \mathbf{n} e^{i(\mathbf{q}-\mathbf{q}')\cdot\mathbf{n}} \right) \quad \text{(B.11b)}$$

Using the following properties:

$$\int d\mathbf{n}\; e^{i(\mathbf{q}-\mathbf{q}')\cdot\mathbf{n}} = (2\pi)^N \delta(\mathbf{q} - \mathbf{q}') \quad \text{(B.12)}$$

$$\int d\mathbf{n}\; \mathbf{n} e^{i(\mathbf{q}-\mathbf{q}')\cdot\mathbf{n}} = -i(2\pi)^N \delta'(\mathbf{q} - \mathbf{q}') \quad \text{(B.13)}$$

Hence the second term becomes:

$$-i \int d\mathbf{q} d\mathbf{q}'\; R_{ij}^{-1,g}(\mathbf{q}) R_{ij}^{-1,g}(\text{-}\mathbf{q}') \delta'(\mathbf{q} - \mathbf{q}') \quad \text{(B.14a)}$$

$$= +i \int d\mathbf{q} d\mathbf{q}'\; \nabla_{\mathbf{q}-\mathbf{q}'} \left(R_{ij}^{-1,g}(\mathbf{q}) R_{ij}^{-1,g}(\text{-}\mathbf{q}') \right) \delta(\mathbf{q} - \mathbf{q}') \quad \text{(B.14b)}$$

$$= +i \int d\mathbf{q}\; R_{ij}^{-1,g}(\mathbf{q}) \nabla_{\mathbf{q}} R_{ij}^{-1,g}(\text{-}\mathbf{q}) \quad \text{(B.14c)}$$

Letting us simplify the numerator of **RP** as:

$$\implies \mathbf{RP}_{num} = \sum_{ij} (\mathbf{r}_i - \mathbf{r}_j) \int d\mathbf{q} R_{ij}^{-1,g}(\mathbf{q}) R_{ij}^{-1,g}(\text{-}\mathbf{q})$$

$$+ i \sum_{ij} \int d\mathbf{q} R_{ij}^{-1,g}(\mathbf{q}) \left(\underline{\mathbf{l}} \cdot \nabla_{\mathbf{q}} \right) R_{ij}^{-1,g}(\text{-}\mathbf{q}) \quad \text{(B.15)}$$

Similarly, the denominator:

$$\mathbf{RP}_{den} = \frac{1}{(2\pi)^N} \sum_{ij} \int d\mathbf{q} d\mathbf{q}' d\mathbf{n}\; R_{ij}^{-1,g}(\mathbf{q}) R_{ij}^{-1,g}(\text{-}\mathbf{q}') e^{i(\mathbf{q}-\mathbf{q}')\cdot\mathbf{n}} \tag{B.16a}$$

$$= \sum_{ij} \int d\mathbf{q} R_{ij}^{-1,g}(\mathbf{q}) R_{ij}^{-1,g}(\text{-}\mathbf{q}) \tag{B.16b}$$

$$= \sum_{ij} \int d\mathbf{q} \left| R_{ij}^{-1,g}(\mathbf{q}) \right|^2 \tag{B.16c}$$

Therefore:

$$\mathbf{RP} = \frac{\sum_{ij}(\mathbf{r}_i - \mathbf{r}_j) \int d\mathbf{q} \left| R_{ij}^{-1,g}(\mathbf{q}) \right|^2}{\sum_{ij} \int d\mathbf{q} \left| R_{ij}^{-1,g}(\mathbf{q}) \right|^2} + i\,\underline{\mathbf{l}} \cdot \frac{\sum_{ij} \int d\mathbf{q} R_{ij}^{-1,g}(\mathbf{q}) \nabla_{\mathbf{q}} R_{ij}^{-1,g}(\text{-}\mathbf{q})}{\sum_{ij} \int d\mathbf{q} \left| R_{ij}^{-1,g}(\mathbf{q}) \right|^2}, \tag{B.17}$$

which in 1D, can be re-written as

$$\mathbf{RP} = \frac{\sum_{ij}(\mathbf{r}_i - \mathbf{r}_j) \int dq \left| R_{ij}^{-1,g}(q) \right|^2}{\sum_{ij} \int dq \left| R_{ij}^{-1,g}(q) \right|^2} + i\mathbf{l} \frac{\sum_{ij} \int dq R_{ij}^{-1,g}(q) \partial_q R_{ij}^{-1,g}(-q)}{\sum_{ij} \int dq \left| R_{ij}^{-1,g}(q) \right|^2}. \tag{B.18}$$

While the generic expression which accounts for spring stiffness can be found in Eq. (4.26).

B.2.2 Gauge invariance of the response position

We need to verify the gauge invariance nature of the wavenumber formula we derived in Eq. (B.17). Suppose that one of the sites "belongs" to the adjacent right cell instead so that

$$r_{i=1} \to r_{i=1} + \mathbf{l}_1. \tag{B.19}$$

It follows that:

$$R_{1,j} \to R_{1,j}\, e^{iq_1} \tag{B.20a}$$

$$\text{then } R_{1j}^{-1,g} \to R_{1j}\, e^{-iq_1} \tag{B.20b}$$

Therefore, the rigidity matrix becomes

$$\mathbf{R} \to \mathbf{R} \begin{pmatrix} e^{iq_1} & 0 & ... & 0 \\ 0 & 1 & ... & 0 \\ ... & & & \\ 0 & 0 & ... & 1, \end{pmatrix} \tag{B.21}$$

and its pseudo inverse is

$$\mathbf{R}^{-1,g} \to \begin{pmatrix} e^{-iq_1} & 0 & ... & 0 \\ 0 & 1 & ... & 0 \\ ... & & & \\ 0 & 0 & ... & 1 \end{pmatrix} \mathbf{R}^{-1,g}. \tag{B.22}$$

The left term of Eq. (B.17) then becomes:

$$\frac{\sum_{ij}(\mathbf{r}_i - \mathbf{r}_j)\int d\mathbf{q}\left|R_{ij}^{-1,g}(\mathbf{q})\right|^2}{\sum_{ij}\int d\mathbf{q}\left|R_{ij}^{-1,g}(\mathbf{q})\right|^2} \to \frac{1}{\sum_{ij}\int d\mathbf{q}...}\Big\{(\mathbf{r}_1 + \mathbf{l}_1 - \mathbf{r}_j)\int d\mathbf{q}|R_{1j}^{-1,g}(\mathbf{q})|^2 + (\mathbf{r}_2 - \mathbf{r}_j)\int d\mathbf{q}|R_{2j}^{-1,g}(\mathbf{q})|^2 + ...\Big\} \tag{B.23}$$

$$= \frac{\sum_{ij}(\mathbf{r}_i - \mathbf{r}_j)\int d\mathbf{q}\left|R_{ij}^{-1,g}(\mathbf{q})\right|^2}{\sum_{ij}\int d\mathbf{q}...} + \mathbf{l}_1\frac{\sum_j\int d\mathbf{q}\left|R_{1j}^{-1,g}(\mathbf{q})\right|^2}{\sum_{ij}\int d\mathbf{q}...} + ... \tag{B.24}$$

Meanwhile

$$\sum_j \int d\mathbf{q} R_{1j}^{-1,g}(\mathbf{q})\nabla_{\mathbf{q}} R_{1j}^{-1,g}(\text{-}\mathbf{q}) \to \sum_j \int d\mathbf{q} R_{1j}^{-1,g}(\mathbf{q}) e^{-iq_1}\nabla_{\mathbf{q}}\left(R_{1j}^{-1,g}(\text{-}\mathbf{q})e^{(+iq_1))}\right) \tag{B.25a}$$

$$= \sum_j \int d\mathbf{q} R_{1j}^{-1,g}(\mathbf{q})\nabla_{\mathbf{q}} R_{1j}^{-1,g}(-\mathbf{q}) + \sum_j \int d\mathbf{q}\big(i,0,0\big)^T |R_{1j}^{-1,g}(\mathbf{q})|^2. \tag{B.25b}$$

So the right term of Eq. (B.17) becomes:

$$i\,\underline{\mathbf{l}}\cdot\frac{\sum_{ij}\int d\mathbf{q}R_{ij}^{-1,g}(\mathbf{q})\nabla_{\mathbf{q}}R_{ij}^{-1,g}(\text{-}\mathbf{q})}{\sum_{ij}\int d\mathbf{q}\left|R_{ij}^{-1,g}(\mathbf{q})\right|^2}\rightarrow \tag{B.26a}$$

$$\rightarrow i\underline{\mathbf{l}}\cdot\frac{\sum_{ij}\int d\mathbf{q}R_{ij}^{-1,g}(\mathbf{q})\nabla_{\mathbf{q}}R_{ij}^{-1,g}(\text{-}\mathbf{q})}{\sum_{ij}\int d\mathbf{q}...}+i\underline{\mathbf{l}}\cdot\frac{\sum_{j}\int d\mathbf{q}\big(i,0,0\big)^T|R_{1j}^{-1,g}(\mathbf{q})|^2}{\sum_{ij}\int d\mathbf{q}...} \tag{B.26b}$$

$$=i\underline{\mathbf{l}}\cdot\frac{\sum_{ij}\int d\mathbf{q}R_{ij}^{-1,g}(\mathbf{q})\nabla_{\mathbf{q}}R_{ij}^{-1,g}(\text{-}\mathbf{q})}{\sum_{ij}\int d\mathbf{q}...}-\mathbf{l}_1\frac{\sum_{j}\int d\mathbf{q}\left|R_{1j}^{-1,g}(\mathbf{q})\right|^2}{\sum_{ij}\int d\mathbf{q}...} \tag{B.26c}$$

In conclusion, a change of gauge creates an additional term for both intra-cell and inter-cell positions, as indicated in Eq. (B.24) and Eq. (B.26c). Those terms are equal and opposite and cancel out, hence the response position as a whole is invariant.

B.2.3 1D Maxwell chain - rotor chain

For systems critically stable, the Maxwell condition makes the rigidity matrix $\mathbf{R}$ square and invertible. In such scenario the pseudo inverse is simply the inverse of the rigidity map $\mathbf{R}^{-1,g}=\mathbf{R}^{-1}$ and we can affirm that the equilibrium displacements $\mathbf{u}(\mathbf{R},\mathbf{K})$ are exactly the zero modes of $\mathbf{R}$. Therefore, this allows us to simplify what the displacement at site i due to swelling at bond j is:

$$u_i^j(\mathbf{R},\mathbf{K})=\left(\mathbf{K}^{1/2}\,\mathbf{R}\right)_{ij}^{-1,g}\,\sqrt{k_j} \tag{B.27a}$$

$$=\left(\mathbf{R}^{-1}\mathbf{K}^{-1/2}\right)_{ij}\sqrt{k_j} \tag{B.27b}$$

$$=\sum_l R_{il}^{-1}k_{lj}^{-1/2}\sqrt{k_j} \tag{B.27c}$$

$$=R_{ij}^{-1}, \tag{B.27d}$$

which means if the system is Maxwell and invertible, varying spring stiffness is pointless and is identical to a system with unit magnitude spring stiffnesses. We can then write the response position per Eq. (B.17).

Let's now investigate how Eq. (4.29) is considered to properly describe the form

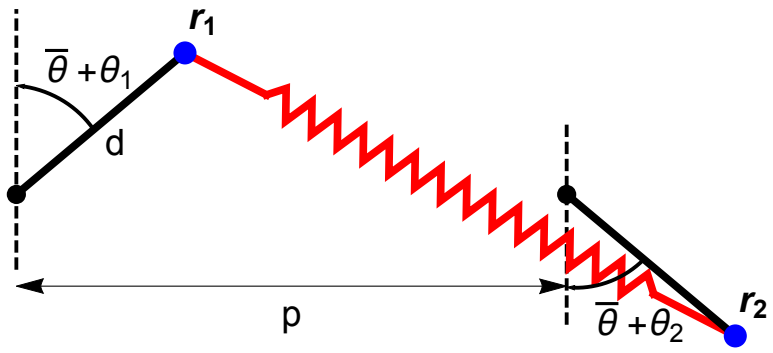

Figure B.1: Geometric description of the 1D rotor chain. The end points $\mathbf{r}_1, \mathbf{r}_2$ of two consecutive rotors of length d are connected by a spring of length l (red). When the spring is at rest, each rotor makes an angle $\bar{\theta}$ with the vertical but when stretched, each rotor rotates by a additional small amount θ_i.

of the rotors' rotation in the linear regime. Using figure B.1, we can Taylor expand about the angle at rest $\bar{\theta}$ and derive the position of the two connected sites along with the orientation of the bond at rest:

$$\mathbf{r}_1 = d\langle \sin\bar{\theta} + \cos\bar{\theta}\,\theta_1, \cos\bar{\theta} - \sin\bar{\theta}\,\theta_1 \rangle \tag{B.28a}$$

$$\mathbf{r}_2 = \langle p + d(\sin\bar{\theta} + \cos\bar{\theta}\,\theta_2), d(-\cos\bar{\theta} + \sin\bar{\theta}\,\theta_2) \rangle \tag{B.28b}$$

$$\hat{r} = \frac{1}{l}\langle p, -2\cos\bar{\theta} \rangle \tag{B.28c}$$

Given the spring's net extension is $e_0 = \hat{r} \cdot (\mathbf{r}_2 - \mathbf{r}_1)$, we can work out the rest length of the spring l_0 (when $\theta_1 = \theta_2 = 0$), its net extension e_{net} and the amount of stretch e:

$$l_0 = \frac{p^2 + 4d^2\cos^2\bar{\theta}}{l} \tag{B.29a}$$

$$e_{\text{net}} = \frac{1}{l}\left(p^2 + pd\cos\bar{\theta}(\theta_2 - \theta_1) + 4d^2\cos^2\bar{\theta} - 2d^2\sin\bar{\theta}\cos\bar{\theta}(\theta_1 + \theta_2)\right) \tag{B.29b}$$

$$\implies e = \frac{d\cos\bar{\theta}}{l}\left((p - 2d\sin\bar{\theta})\,\theta_2 - (p + 2d\sin\bar{\theta})\,\theta_1\right) \tag{B.29c}$$

This can be rewritten in the same form as Eq. (4.29) with the caveat that $\theta_i \to u_i$,

considering that

$$e = a\,\theta_2 - b\,\theta_1 \tag{B.30a}$$

$$\text{with } \begin{cases} a = \left(d\cos\bar{\theta}(p - 2d\sin\bar{\theta})\right)/l \\ b = \left(d\cos\bar{\theta}(p + 2d\sin\bar{\theta})\right)/l \end{cases} \tag{B.30b}$$

We clearly see that if $\bar{\theta} = 0$, the terms a and b equal one another, which in the context of mechanics, correspond to zero energy deformations spread across the bulk (i.e, the translation mode). Throughout Chapter 4 and this section, we set the a coefficient to 1 and only base our study of mechanics on the value of coefficient b with respect to 1, which we refer to as the "degree of polarization" of the 1D rotor chain.

We can rewrite our constraint equation for all rotors n via the rigidity map. In reciprocal space, assuming Bloch's form for the rotations/displacements $u_n = u_0 e^{iqn}$, this means the rigidity matrix and its pseudo-inverse are

$$e_n = u_{n+1} - bu_n = (e^{iq} - b)u_n \tag{B.31}$$

$$\implies \mathbf{R}(q) = (e^{iq} - b) \quad \mathbf{R}^{-1,g}(q) = 1/(e^{iq} - b). \tag{B.32}$$

We derive an expression for the response position of the Maxwell 1D rotor chain using equation (B.18) and since there is only 1 site and 1 bond per cell:

$$\mathbf{RP} = \frac{(\mathbf{r}_p - \mathbf{r}_b)\int dq\ |R^{1,-g}(q)|^2}{\int dq\ |R^{-1,g}(q)|^2} + i\mathbf{l}\,\frac{\int dq\, R^{-1,g}(q)\partial_q R^{1,-g}(-q)}{\int dq\ |R^{-1,g}(q)|^2}. \tag{B.33a}$$

$$= \mathbf{r}_p - \mathbf{r}_b + i\mathbf{l}\,\frac{\int dq\, R^{-1,g}(q)\partial_q R^{-1,g}(\text{-}q)}{\int dq\, |R^{-1,g}(q)|^2}, \tag{B.33b}$$

which you can find simplified in the main.

B.2.4 Double spring rotor chain

As mentioned in the hyperstatic double chain of section 4.2, the new rigidity matrix accounting for two different springs (b_1, k_1 and b_2, k_2) of the 1D rotor chain is

$$\mathbf{R}(\mathbf{q}) = \left(\sqrt{k_1}(e^{iq} - b_1), \sqrt{k_2}(e^{iq} - b_2)\right) \tag{B.34}$$

$$\implies \mathbf{R}^{-1,g}(q) = \begin{pmatrix} \frac{-b_1\sqrt{k_1}+\sqrt{k_1}e^{-iq}}{b_1^2k_1-2\cos(q)(b_1k_1+b_2k_2)+b_2^2k_2+k_1+k_2} & \frac{-b_2\sqrt{k_2}+\sqrt{k_2}e^{-iq}}{b_1^2k_1-2\cos(q)(b_1k_1+b_2k_2)+b_2^2k_2+k_1+k_2} \end{pmatrix} \tag{B.35}$$

While we choose that the chain to be oriented along the x direction, $\mathbf{l} = l\,\hat{x}$, that the one-site of each cell is placed at the origin $\mathbf{r}_p = 0$ then, this suggests that both springs are halfway between two consecutive sites along the x direction, $\mathbf{r}_1 = r_1\hat{x} = \mathbf{r}_2 = r_2\hat{x} = l/2\,\hat{x}$:

$$\begin{aligned} \mathrm{RP} = &- \frac{r_1k_1\int dq\,\left|R_1^{-1,g}(q)\right|^2}{\int dq\,k_1\left|R_1^{-1,g}(q)\right|^2 + k_2\left|R_2^{-1,g}(q)\right|^2} + il\,\frac{k_1\int dq\,R_1^{-1,g}(q)\partial_q R_1^{-1,g}(\text{-}q)}{\int dq\,k_1\left|R_1^{-1,g}(q)\right|^2 + k_2\left|R_2^{-1,g}(q)\right|^2} \\ &- \frac{r_2k_2\int dq\,\left|R_2^{-1,g}(q)\right|^2}{\int dq\,k_1\left|R_1^{-1,g}(q)\right|^2 + k_2\left|R_2^{-1,g}(q)\right|^2} + il\,\frac{k_2\int dq\,R_2^{-1,g}(q)\partial_q R_2^{-1,g}(\text{-}q)}{\int dq\,k_1\left|R_1^{-1,g}(q)\right|^2 + k_2\left|R_2^{-1,g}(q)\right|^2} \end{aligned} \tag{B.36a}$$

$$= -l/2 + i\,l\,\frac{\int dq\,k_1R_1^{-1,g}(q)\partial_q R_1^{-1,g}(\text{-}q) \;+\; k_2R_2^{-1,g}(q)\partial_q R_2^{-1,g}(\text{-}q)}{\int dq\,k_1\left|R_1^{-1,g}(q)\right|^2 + k_2\left|R_2^{-1,g}(q)\right|^2} \tag{B.36b}$$

B.3 Perturbative Theory

We start with $\mathbf{R}_0$, the rigidity matrix of primary bonds in the 1D rotor chain. Since we plan to add disorder, we can no longer resolve the mechanical response in wavenumber space... we must do so in real space. Consider n_{swap} the number of removed and added bonds. These added bonds are pulled from the next nearest neighbor 1D rotor chain (a.k.a secondary bonds). In order to remain isostatic, the number of removed bonds must be balanced with those added.

Define $|\mathbf{e}_m\rangle$ the set of removed bonds. Let $\mathbf{R}_m$ be $\mathbf{R}_0$ with the $\mathbf{e}_m$ bonds removed. We look for a mechanical response due to swelling of one bond, written form as $\mathbf{e}_s$:

$$\mathbf{R}_m\mathbf{u} = \mathbf{e}_s \tag{B.37}$$

$$\implies \mathbf{u} = \mathbf{R}_0^{-1}\left(\mathbf{e}_s + \sum_{i=1}^{n_{\text{swap}}} a_i \mathbf{e}_m^i\right) \tag{B.38}$$

In this form, $|\mathbf{e}_m\rangle$ form an orthonormal basis of the removed bonds. We now define a new rigidity matrix which incorporates for the secondary added bonds:

$$\mathbf{R}_m = \mathbf{R}_m + \delta\mathbf{R} \tag{B.39}$$

Using a perturbative method to 1st order:

$$(\mathbf{R}_m + \delta\mathbf{R})(\mathbf{u} + \delta\mathbf{u}) = \mathbf{e}_s \tag{B.40a}$$

$$\implies \mathbf{R}_m\delta\mathbf{u} + \delta\mathbf{R}\mathbf{u} = 0 \tag{B.40b}$$

$$\implies \delta\mathbf{u} = \mathbf{R}_0^{-1}\left(-\delta\mathbf{R}\mathbf{u} + \sum_{j}^{n_{\text{swap}}} b_j \mathbf{e}_m^j\right), \tag{B.40c}$$

this last line follows the same reasoning of Eq. (B.38). Then once again, we plug the result of Eq. (B.38) here and drop the summation symbol:

$$\delta\mathbf{u} = \mathbf{R}_0^{-1} b_j \mathbf{e}_m^j - \mathbf{R}_0^{-1}\delta\mathbf{R}\mathbf{R}_0^{-1}\left(\mathbf{e}_s + a_i\mathbf{e}_m^i\right) \tag{B.41}$$

Let's now define a couple of projection operators:

$$\mathbf{P}_p = \mathbf{R}_m\,\mathbf{R}_0^{-1} = \text{ projection operator from space of non-removed bonds} \tag{B.42}$$

$$\mathbf{P}_m = \mathbf{I} - \mathbf{P}_p = \text{ its complement} \tag{B.43}$$

Let's apply $\mathbf{R}_m$ on $\delta\mathbf{u}$ from Eq. (B.41):

$$\mathbf{R}_m\delta\mathbf{u} = \mathbf{R}_m\mathbf{R}_0^{-1}b_j\mathbf{e}_m^j - \mathbf{R}_m\mathbf{R}_0^{-1}\delta\mathbf{R}\mathbf{R}_0^{-1}\left(\mathbf{e}_s + a_i\mathbf{e}_m^i\right) \tag{B.44a}$$

$$= \cancel{\mathbf{P}_p b_j \mathbf{e}_m^j} - P_p\delta\mathbf{R}\mathbf{R}_0^{-1}\left(\mathbf{e}_s + a_i\mathbf{e}_m^i\right). \tag{B.44b}$$

We now have two equations involving $\mathbf{R}\delta\mathbf{u}$: equations B.44b and B.40b. We equate those two and once again take advantage of Eq. (B.38):

$$-\mathbf{P}_p\delta\mathbf{R}\mathbf{R}_0^{-1}\left(\mathbf{e}_s + a_i\mathbf{e}_m^i\right) = -\delta\mathbf{R}\mathbf{u} \tag{B.45a}$$

$$= -\delta\mathbf{R}\mathbf{R}_0^{-1}\left(\mathbf{e}_s + a_i\mathbf{e}_m^i\right) \tag{B.45b}$$

$$= -(\mathbf{P}_p + \mathbf{P}_m)\delta\mathbf{R}\mathbf{R}_0^{-1}\left(\mathbf{e}_s + a_i\mathbf{e}_m^i\right) \tag{B.45c}$$

$$\implies -\mathbf{P}_p\delta\mathbf{R}\mathbf{R}_0^{-1}\left(\mathbf{e}_s + a_i\mathbf{e}_m^i\right) = -\mathbf{P}_p\delta\mathbf{R}\mathbf{R}_0^{-1}\left(\mathbf{e}_s + a_i\mathbf{e}_m^i\right) + \mathbf{P}_m\delta\mathbf{R}\mathbf{R}_0^{-1}\left(\mathbf{e}_s + a_i\mathbf{e}_m^i\right) \tag{B.45d}$$

Which finally means

$$\implies \mathbf{P}_m\delta\mathbf{R}\mathbf{R}_0^{-1}\left(\mathbf{e}_s + a_i\mathbf{e}_m^i\right) = 0. \tag{B.46}$$

Finally, by projecting the result of Eq. (B.46) on the space of removed bonds we get rid of the projecting operator $\mathbf{P}_m$. We actually project on the basis of that space the $\mathbf{e}_m^j$'s and are left with n_{swapped} equations for n_{swapped} unknowns a_i:

$$\delta\mathbf{R}\mathbf{R}_0^{-1}\left(\mathbf{e}_s + a_i\mathbf{e}_m^i\right)\cdot\mathbf{e}_m^j = 0 \text{ for all } j \tag{B.47}$$

which is a solvable system. Determining the a_i's then helps us solve for the total displacement:

$$\mathbf{u} = \mathbf{R}_0^{-1}\left(\mathbf{e}_s + a_i\mathbf{e}_m^i\right) \tag{B.48}$$

where $\mathbf{e}_s$ is source, $\{\mathbf{e}_m\}$ is the set of removed bonds, $\mathbf{R}_0$ is the original rigidity matrix and where $\delta\mathbf{R}$ is the matrix of added secondary bonds.

Appendix C
CORNER MODE

C.1 Complex projective space and positive degree

In this section, we look to prove that the scale invariance property of $\mathbf{u}$ doesn't affect the validity of the topological degree of the map of Eq. (5.3). As we've mentioned, our concern is with modes that satisfy.

$$R : (\mathbf{u}, \mathbf{z}) \rightarrow \mathbf{e} = 0. \tag{C.1}$$

A naive count would suggest that solutions to such linear function exist when the constraints are equal in number to the combined total number of degrees of freedom of $\mathbf{u}, \mathbf{z}$. However, since scaling $\mathbf{u}$ by a factor α doesn't change anything, we must take 1 degree of freedom out of this equation [as done in Eq. (5.2)]. In reality, the mathematical procedure behind this trick consists in projecting the vector of deformation $\mathbf{u}$ into the complex projective space $CP^{n_{\text{d.o.f}}-1}$, and to leave $\mathbf{z}, \mathbf{e}$ in the full complex spaces of n, n_{con} respectively.

However, the result of Eq. (5.3) relies on the fact that the Jacobian of the constraint map J_R is positive (which we show in section C.2). This condition holds for holomorphic maps between complex spaces, but it is not obvious that it extends to maps from complex projective spaces. Let's consider a modified constraint map that accounts for the original rigidity function and a constraint on normalization:

$$R : (\mathbf{u}', \mathbf{z}) \rightarrow (\mathbf{e}, e'), \tag{C.2}$$

$$\text{with } \mathbf{u}' \in \mathcal{C}^{n_{\text{d.o.f}}} \text{ and } e' \equiv \mathbf{u}' \cdot \mathbf{s} - 1 = 0, \tag{C.3}$$

where $\mathbf{u}'$ refers to a non-normalized complex vector and $\mathbf{s}$ is simply a vector of reference. This additional constraint on e' is necessary to prevent a scaling like $\mathbf{u} \to \alpha\mathbf{u}$. Let's now break down the $\mathbf{u}'$ vector into components: $\mathbf{u}' = \{\phi_j, \mathbf{u}' \cdot \mathbf{s}\}$ where

- the $2(n_{\text{d.o.f}} - 1)$ $\{\phi_j\}$'s are the coordinates describing the position of $\mathbf{u}$
- $\mathbf{u}' \cdot \mathbf{s}$ encodes the remaining constraints

The Jacobian of the full map then becomes

$$\begin{pmatrix} \frac{\partial \mathbf{e}}{\partial \mathbf{z}} & \frac{\partial \mathbf{e}}{\partial \mathbf{p}} & \frac{\partial \mathbf{e}}{\partial \mathbf{u}' \cdot \mathbf{s}} \\ \frac{\partial e'}{\partial \mathbf{z}} & \frac{\partial e'}{\partial \mathbf{p}} & \frac{\partial e'}{\partial \mathbf{u}' \cdot \mathbf{s}} \end{pmatrix}. \tag{C.4}$$

Recognizing that the bottom row is simply $(0, \ldots 0, \mathbf{I})$, this Jacobian has the same determinant than $(\frac{\partial \mathbf{e}}{\partial \mathbf{z}}, \frac{\partial \mathbf{e}}{\partial \mathbf{p}})$, which is the Jacobian of the original constraint map $\mathbf{R}$. Hence, since the small Jacobian has a positive real determinant, the larger one does as well and we've proven that the scale invariance property doesn't affect the degree of the map.

C.2 Topological Degree Theorem

Let us define the notion of *degree* of a map, a concept well known in topology [98]. The degree of a map f from a closed and oriented $(n-1)$ dimensional manifold $\partial\mathbf{M}$ to the surface of the corresponding unit hypersphere $\mathbf{S}^{n-1}$ is the (signed) integer number of times that hypersphere is covered:

$$\deg f = \frac{1}{A_{n-1}} \int_{\partial \mathbf{M}} f^* \sigma', \tag{C.5}$$

where A_{n-1} is the surface area of $\mathbf{S}^{n-1}$ and σ' is on $\partial\mathbf{M}$. Like described on figure 2.4 for the winding number, our degree remains invariant so long as the zeros of f remain within the boundary. We can therefore show that the degree of the map is equal to the number the zeros, times their multiplicity. However, we're not entirely certain

that a zero contributes "positively" here. Hence, we can't yet affirm that the degree of the map corresponds exactly to the number of zeros.

As we discussed in the main, our mappings can be described via complex, holomorphic functions. In this particular chapter, we've shown that the Jacobian of our system involves complex projective spaces and yet is still positive (see Appendix C.1). Taking that as given, we use Ref. [105], where in Chapter 2, D'Angelo uses a holomorphic map that is considered from the boundary of a space of n complex coordinates to the equal-dimension unit sphere, $\mathbf{S}^{2n-1}$. This is precisely the framework in which we apply our topological degree; it is then found that the degree of the map is the sum of the degrees over isolated zeros within the region, with the particular condition that each degree is always *positive*, given the holomorphic property and the positive Jacobian. Hence, for our rigidity map $\mathbf{R}(\mathbf{z})$, which is holomorphic, the number of zeros in the region of interest $\mathcal{B}$ is precisely

$$N_{\mathcal{B}} = A^{-1}_{2n_{\text{con}}-1} \int_{\partial\mathcal{B}} dv_1 \dots dv_{2n_{\text{con}}-1} J_R(\mathbf{v}). \tag{C.6}$$

In the context of our lower left corner modes, the region $\mathcal{B}$ and its boundary $\partial\mathcal{B}$ are defined by:

$$\mathcal{B} = \{|z_1| < 1 \text{ and } |z_2| < 1\} \tag{C.7}$$

$$\partial\mathcal{B} = \{|z_1| < 1 \text{ and } |z_2| = 1\} \cup \{|z_2| < 1 \text{ and } |z_1| = 1\} \tag{C.8}$$

That way, the number of modes in $\mathcal{B}$ is equal to the number of times the constraint map takes boundary $\partial\mathcal{B}$ over the hypersphere $\mathbf{S}^{2n_{\text{con}}-1}$.

C.3 Constraint Geometry

We now explore three different approaches to parametrize the mode and the constraints of the checkerboard system studied in section 5.2, including the one of shear-

ing voids that we select in the main. Our goal isn't to capture all sets of possible configurations, but instead to capture the possible motions allowed in a zero-energy setting for the system. Additionally, we care little for the rigid-body motions of translations and global rotation and hence, do not account for those.

C.3.1 Ball and spring networks

The first method is to employ the conventional network of sites connected by springs and to derive the rigidity matrix that maps from sites's displacements to springs extension. Since each vertex of the quadrilateral piece is shared between two pieces, two vertices are needed per unit cell, while each rigid face consists of 5 non-violable constraints (4 sides + a diagonal). This turns into a 4×5 rigidity problem for each cell, confirming that we're in fact in a 2^{nd}-order Maxwell system.

C.3.2 Rotations of the pieces

We can also take advantage that the pieces are free to rotate, up until the part that they must close at all touching vertices. This does in fact qualify as a zero-energy mode. In the linear regime, the rotation of a piece by angle θ_{n_1,n_2} implies that each edge has been moved by that same amount. We can then easily derive the constraint condition at one around one of the voids. For example, on figure C.1, at the center void, it reads:

$$\mathbf{r_4}\theta_{n_1,n_2} + \mathbf{r_3}\theta_{n_1,n_2+1} + \mathbf{r_2}\theta_{n_1+1,n_2+1} + \mathbf{r_1}\theta_{n_1+1,n_2} = 0. \tag{C.9}$$

where n_1, n_2 indicates the lower left piece (in blue). Assuming Bloch's theorem [66], that $\theta_{n_1,n_2} = \theta_0 z_1^{n_1} z_2^{n_2}$, then Eq. (C.9) simplifies into

$$\mathbf{r_4} + z_1\mathbf{r_1} + z_2\mathbf{r_3} + z_1 z_2\mathbf{r_2} = 0. \tag{C.10}$$

The 4×5 problem of the previous section is therefore reduced to a 2×2 (2 z_i variables

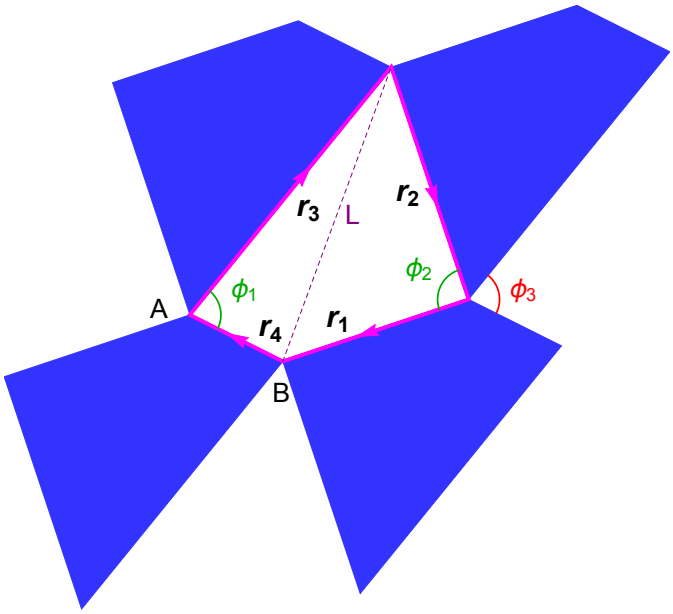

Figure C.1: Representation of a 2×2 checkerboard pieces. The vertices A, B along the 5 connecting edges form the unit cell in the sites and bonds characterization. The angles ϕ_1, ϕ_2, ϕ_3 represent the shearing motions across each void.

and 2 constraints along the x and y directions), which considerably simplifies the difficulty of finding a solution.

C.3.3 Shearing of voids

Our third and preferred way of enforcing the constraints is not to account for rotations of the pieces, but instead shearing of the voids. A shearing mode is valid only if opposite angles across a vertex are equal and opposite. As shown in figure C.1, the diagonal L can be re-written in terms of the edges of the pieces and the interior angles:

$$L^2 = r_3^2 + r_4^2 - 2r_3 r_4 \cos(\phi_1), \tag{C.11a}$$

$$L^2 = r_1^2 + r_2^2 - 2r_1 r_2 \cos(\phi_2). \tag{C.11b}$$

Using the constraint condition $\partial\phi_3/\partial\phi_2 = -1$, we find

$$\frac{\partial\phi_3}{\partial\phi_1} = -\left(\frac{\partial L^2}{\partial\phi_1}\right)\left(\frac{\partial L^2}{\partial\phi_2}\right)^{-1} \tag{C.12a}$$

$$= -\frac{r_3 r_4}{r_1 r_2}\frac{\sin\phi_1}{\sin\phi_2}. \tag{C.12b}$$

$$\implies \frac{\partial\phi_3}{\partial\phi_1} = -\frac{|\mathbf{r_3}\times\mathbf{r_4}|}{|\mathbf{r_1}\times\mathbf{r_2}|}. \tag{C.12c}$$

Assuming Bloch's form for the shearing mode s, we recognize $\phi_3 = \phi_1 z_1$ and a similar constraint along the second lattice direction and find:

$$|\mathbf{r_3}\times\mathbf{r_4}| + |\mathbf{r_1}\times\mathbf{r_2}|z_1 = 0, \tag{C.13a}$$

$$|\mathbf{r_1}\times\mathbf{r_4}| + |\mathbf{r_3}\times\mathbf{r_2}|z_2 = 0. \tag{C.13b}$$

We can now generate the zero mode in $\mathbf{z}$ space, as a function of the geometry of the rigid pieces

$$z_1 = -\frac{|\mathbf{r_3}\times\mathbf{r_4}|}{|\mathbf{r_1}\times\mathbf{r_2}|}, \tag{C.14a}$$

$$z_2 = -\frac{|\mathbf{r_1}\times\mathbf{r_4}|}{|\mathbf{r_3}\times\mathbf{r_2}|}. \tag{C.14b}$$

These elements correspond respectively to $-b_1/a_1$ and $-b_2/a_2$ in Eq. (5.5). These results reveal an interesting symmetry for our system. Since each of the cross-product terms correspond to the area spanned by the each of two corresponding vectors, we can make a statement on the center of mass of the piece with respect to each diagonal: if for example, the center of mass is to the left of the vertical diagonal of the void, then $z_1 < 1$. This indicates that the system becomes symmetric under $n_1 \to -n_1$ when the center of mass lies along the vertical diagonal, which corresponds to a bulk mode along the first lattice direction (but not necessarily along the second). If additionally, the center of mass lies at the intersection of both diagonals, we then deal with a

complete bulk mode. We indicate how a deformation of the piece can in fact lead to the mode moving around the 4 corners, but also along the 4 edges and in the bulk (figure 5.3).

C.4 Numerical calculation of topological degree

Let's set a function f similar in form to the constraint map of Eq. (5.4):

$$\mathbf{f} = (f_1, f_2) = (b_1 + a_1 z_1, b_2 + a_2 z_2). \tag{C.15}$$

We've shown the regions of interest are

$$\mathcal{B}_{\mathrm{LL}} = \{|z_1| \leqslant 1, |z_2| \leqslant 1\} \tag{C.16}$$

$$\partial\mathcal{B}_{\mathrm{LL}} = \{|z_1| \leqslant 1, |z_2| = 1\} \cup \{|z_1| = 1, |z_2| \leqslant 1\} \tag{C.17}$$

On figure C.2, this region is shown as a red arrow. In order to perform the integral over it, we need to parametrize our three-dimensional surface $\partial\mathcal{B}_{\mathrm{LL}}$, starting with:
1) the portion of the surface where $|z_2| = 1$ (indicated by the horizontal part of the red arrow). On it we have $0 \leqslant |z_1| \leqslant 1$, and $-\pi \leqslant \arg z_1, \arg z_2 \leqslant \pi$:

$$\begin{cases} z_1 = |z_1| e^{i \arg z_1} \\ z_2 = e^{i \arg z_2} \end{cases} \xrightarrow[v_0 = |z_1| - 1]{\phi_i = \arg z_i} \begin{cases} z_1 = (1 + v_0) e^{i\phi_1} \\ z_2 = e^{i\phi_2} \end{cases} \tag{C.18}$$

with $-1 \leqslant v_0 \leqslant 0$, and $-\pi \leqslant \phi_1, \phi_2 \leqslant \pi$.
2) the portion of the surface where $|z_1| = 1$ (indicated by the vertical part of the red arrow, which points down). On it we have $0 \leqslant |z_2| \leqslant 1$, similar argument for the arguments, but watch as the magnitude of z_2 decreases to keep the contour oriented

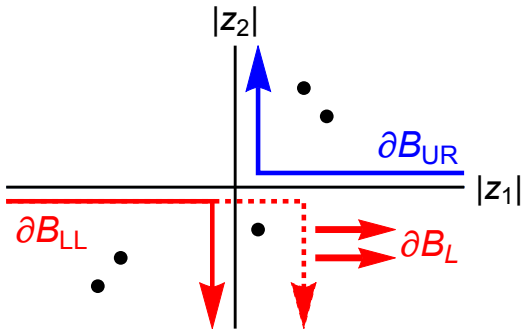

Figure C.2: Representation of the zero modes similar to those obtained from the deformed checkerboard lattice, in a manifold of mode coordinates' magnitude $|z_1|, |z_2|$, with the phases of z_i not shown. The "origin" of such plot is the bulk mode $|z_1| = |z_2| = 1$. Zero modes in the region of interest $\mathcal{B}$ (those exponentially localized in the lower left corner of the system) appear in the lower left quadrant of the plot, with the oriented boundary $\mathcal{B}_{\text{LL}}$ of this region marked by a red arrow. This region may be extended to the right (dashed arrow) to capture the lower right corner zero modes and hence obtain the total number of modes localized to the bottom edge ($|z_2 \leqslant 1|$) with care taken for this non-compact region. Similarly, one can obtain the number of zeros in the upper-right corner, as indicated by the blue arrow, as long as a change of gauge is made.

along the same direction:

$$\begin{cases} z_1 = e^{i \arg z_1} \\ z_2 = |z_2| e^{i \arg z_2} \end{cases} \xrightarrow[v_0 = 1 - |z_2|]{\phi_i = \arg z_i} \begin{cases} z_1 = e^{i\phi_1} \\ z_2 = (1 - v_0) e^{i\phi_2} \end{cases} , \tag{C.19}$$

with $0 \leqslant v_0 \leqslant 1$. We summarize all this as follow:

$$\text{For } -\pi \leqslant \phi_1, \phi_2 \leqslant \pi, \ (z_1, z_2) = \begin{cases} \left((1 + v_0) e^{i\phi_1}, e^{i\phi_2}\right) & \text{if } -1 \leqslant v_0 < 0 \\ \left(e^{i\phi_1}, (1 - v_0) e^{i\phi_2}\right) & \text{if } 0 \leqslant v_0 \leqslant 1 \end{cases} \tag{C.20}$$

We wish to express our constraints in terms of real numbers, such that

$$\mathbf{f} \equiv (\text{Re} f_1, \text{Im} f_1, \text{Re} f_2, \text{Im} f_2) \text{ and } \hat{f} \equiv \mathbf{f}/|\mathbf{f}| \tag{C.21}$$

and now aim to find the volume element of the Jacobian map from $\partial\mathcal{B}$ to the three-

sphere $\mathbf{S}^3$. Problem is that the normalization of $\mathbf{f}$ reduces the dimension of the constraints to 3 and right now, we're looking to evaluate the volume of a 3D object in a 4D space. To that end, we re-augment the size of the Jacobian to 4, by including the normalized vector $\hat{f}$, which by definition is orthonormal to all 3 derivatives $\partial_{v_0}\hat{f}, \partial_{\phi_1}\hat{f}, \partial_{\phi_2}\hat{f}$. This makes the computation of our Jacobian volume much easier:

$$J(\mathbf{v}) = \det\left[\hat{f}, \partial_{v_0}\hat{f}, \partial_{\phi_1}\hat{f}, \partial_{\phi_2}\hat{f}\right]. \tag{C.22}$$

Hence, the degree of the map, which gives the number of zeros in $\mathcal{B}$, is for a given checkerboard lattice

$$N_{\mathcal{B}} = A_3^{-1}\int_{-1}^{1} dv_0 \int_{-\pi}^{\pi} d\phi_1 \int_{-\pi}^{\pi} d\phi_2\, J(\mathbf{v}). \tag{C.23}$$

As seen in figure 5.3, the numerical calculation of the topological degree [Eq. (C.23)] agrees with the direct calculation for the lower-left corner [Eq. (C.14)]. To obtain the charge in the other corners, a new choice of gauge is imposed.

C.5 Change of Gauge: Additional corners

As seen on figures C.2 and figure 5.3, we may want to address how to compute the charge in let's say the lower right corner (where $|z_2| < 1$ but $|z_1| > 1$). This means that in our original coordinate system $\mathcal{B}_{\mathrm{LR}}$ is not compact, which invalidates the computation of topological degree of the map. We fix such issue by changing how the indexing along the first direction is defined: n_1 assumes its lowest value on the right edge and counts up as we move toward the left. This creates a coordinate system in which $z_1 \to 1/z_1$ and $\mathcal{B}_{\mathrm{LR}}$ becomes compact.

One must be careful about the holomorphic property of the constraint function. In fact, such transformation on z_1 means $b_1 + a_1 z_1 = 0 \to b_1 + a_1/z_1 = 0$. In order to apply the theorem, we must recover a minimally holomorphic gauge by scaling the

constraint by z_1: $a_1 + zb_1 = 0$. The zero mode solution is then simply the lower left one with the inversion $a_1 \leftrightarrow b_1$. We repeat this change of gauge for the two other corners, in order to compute the topological degree each time and plot the results on figure 5.3.

BIBLIOGRAPHY

[1] S. Luding, "Cohesive, frictional powders: contact models for tension," *Granular matter*, vol. 10, no. 4, p. 235, 2008.

[2] N. P. Mitchell, L. M. Nash, D. Hexner, A. M. Turner, and W. T. Irvine, "Amorphous topological insulators constructed from random point sets," *Nature Physics*, p. 1, 2018.

[3] T. Lubensky, C. Kane, X. Mao, A. Souslov, and K. Sun, "Phonons and elasticity in critically coordinated lattices," *Reports on Progress in Physics*, vol. 78, no. 7, p. 073901, 2015.

[4] D. Z. Rocklin, "Directional mechanical response in the bulk of topological metamaterials," *New Journal of Physics*, vol. 19, no. 6, p. 065004, 2017.

[5] A. Saremi and Z. Rocklin, "Controlling the deformation of metamaterials: Corner modes via topology," *Physical Review B*, vol. 98, no. 18, p. 180102, 2018.

[6] C. Kane and T. Lubensky, "Topological boundary modes in isostatic lattices," *Nature Physics*, vol. 10, no. 1, p. 39, 2014.

[7] L. Da Vinci, *The notebooks of Leonardo da Vinci*, vol. 1. Courier Corporation, 2012.

[8] B. Cohen, *Isaac Newton's Papers and Letters on Natural Philosophy and Related Documents*. Harvard University Press, 2nd ed., 1978.

[9] R. Hooke, *Micrographia, Or, Some Physiological Descriptions of Minute Bodies Made by Magnifying Glasses : with Observations and Inquiries Thereupon*. J. Martyn and J. Allestry, 1665.

[10] J. Bernoulli and N. Bernoulli, *Die Werke von Johann I und Nicolaus II Bernoulli: Band 6: Mechanik I (v. 6)*, vol. 6. Birkhuser, 2008 ed., 2008.

[11] T. Young, *A course of lectures on natural philosophy and the mechanical arts: in two volumes*, vol. 2. Johnson, 1807.

[12] A.-L. Cauchy, "De la pression ou tension dans un corps solide," *Ex. de math*, vol. 2, pp. 42–56, 1827.

[13] L. Landau, E. Lifshitz, A. Kosevich, J. Sykes, L. Pitaevskii, and Reid, *Theory of Elasticity: Volume 7*. Course of theoretical physics, Elsevier Science, 1986.

[14] J. van der Gucht, "Grand challenges in soft matter physics," *Frontiers in Physics*, vol. 6, p. 87, 2018.

[15] A. Drescher and G. D. J. De Jong, "Photoelastic verification of a mechanical model for the flow of a granular material," *Journal of the Mechanics and Physics of Solids*, vol. 20, no. 5, pp. 337–340, 1972.

[16] M. Cates, J. Wittmer, J.-P. Bouchaud, and P. Claudin, "Jamming, force chains, and fragile matter," *Physical review letters*, vol. 81, no. 9, p. 1841, 1998.

[17] A. J. Liu and S. R. Nagel, "Jamming is not just cool any more," *Nature*, vol. 396, no. 6706, pp. 21–22, 1998.

[18] S. Torquato and F. H. Stillinger, "Multiplicity of generation, selection, and classification procedures for jammed hard-particle packings," *The Journal of Physical Chemistry B*, vol. 105, no. 47, pp. 11849–11853, 2001.

[19] R. Farr, J. R. Melrose, and R. Ball, "Kinetic theory of jamming in hard-sphere startup flows," *Physical Review E*, vol. 55, no. 6, p. 7203, 1997.

[20] E. Brown, N. Rodenberg, J. Amend, A. Mozeika, E. Steltz, M. R. Zakin, H. Lipson, and H. M. Jaeger, "Universal robotic gripper based on the jamming of granular material," *Proceedings of the National Academy of Sciences*, vol. 107, no. 44, pp. 18809–18814, 2010.

[21] J.-P. Wang, "Force transmission modes of non-cohesive and cohesive materials at the critical state," *Materials*, vol. 10, no. 9, p. 1014, 2017.

[22] J. N. Grima and K. E. Evans, "Auxetic behavior from rotating squares," *Journal of Materials Science Letters*, vol. 19, pp. 1563–1565, 2000.

[23] W. Yang, Z.-M. Li, W. Shi, B.-H. Xie, and M.-B. Yang, "Review on auxetic materials," *Journal of materials science*, vol. 39, no. 10, pp. 3269–3279, 2004.

[24] Z. Song, T. Ma, R. Tang, Q. Cheng, X. Wang, D. Krishnaraju, R. Panat, C. K. Chan, H. Yu, and H. Jiang, "Origami lithium-ion batteries," *Nature communications*, vol. 5, no. 1, pp. 1–6, 2014.

[25] K. Miura, "Method of packaging and deployment of large membranes in space," *The Institute of Space and Astronautical Science report*, vol. 618, pp. 1–9, 1985.

[26] J. McInerney, B. G.-g. Chen, L. Theran, C. Santangelo, and Z. Rocklin, "Hidden symmetries generate rigid folding mechanisms in periodic origami," *arXiv preprint arXiv:2003.01095*, 2020.

[27] B. G.-g. Chen, B. Liu, A. A. Evans, J. Paulose, I. Cohen, V. Vitelli, and C. Santangelo, "Topological mechanics of origami and kirigami," *Physical review letters*, vol. 116, no. 13, p. 135501, 2016.

[28] M. Czajkowski, C. Coulais, M. Van Hecke, and Z. Rocklin, "Exotic soft modes in 2d mechanical metamaterials yield powerful new analytic prediction methods," *Bulletin of the American Physical Society*, vol. 65, 2020.

[29] M. Hanifpour, C. F. Petersen, M. J. Alava, and S. Zapperi, "Mechanics of disordered auxetic metamaterials," *The European Physical Journal B*, vol. 91, no. 11, p. 271, 2018.

[30] J. A. Michel and P. J. Yunker, "Structural hierarchy confers error tolerance in biological materials," *Proceedings of the National Academy of Sciences*, vol. 116, no. 8, pp. 2875–2880, 2019.

[31] J. Cha, K. W. Kim, and C. Daraio, "Experimental realization of on-chip topological nanoelectromechanical metamaterials," *Nature*, vol. 564, no. 7735, pp. 229–233, 2018.

[32] C. P. Broedersz, X. Mao, T. C. Lubensky, and F. C. MacKintosh, "Criticality and isostaticity in fibre networks," *Nature Physics*, vol. 7, no. 12, pp. 983–988, 2011.

[33] A. Saremi and Z. Rocklin, "Topological elasticity of flexible structures," *Physical Review X*, vol. 10, no. 1, p. 011052, 2020.

[34] M. Nakahara, *Geometry, topology and physics*. CRC Press, 2003.

[35] V. Guillemin and A. Pollack, *Differential Topology*. AMS Chelsea Publishing, AMS Chelsea Pub., 2010.

[36] D. Pesin and A. H. MacDonald, "Spintronics and pseudospintronics in graphene and topological insulators," *Nature materials*, vol. 11, no. 5, p. 409, 2012.

[37] V. Lahtinen and J. Pachos, "A short introduction to topological quantum computation," *SciPost Physics*, vol. 3, no. 3, p. 021, 2017.

[38] D. Z. Rocklin, *What Topology Reveals About Real Systems*. Georgia Institute of Technology, 2018.

[39] J. Paulose, A. S. Meeussen, and V. Vitelli, "Selective buckling via states of self-stress in topological metamaterials," *Proceedings of the National Academy of Sciences*, vol. 112, no. 25, pp. 7639–7644, 2015.

[40] J. Paulose, B. G.-g. Chen, and V. Vitelli, "Topological modes bound to dislocations in mechanical metamaterials," *Nature Physics*, vol. 11, no. 2, p. 153, 2015.

[41] R. Süsstrunk and S. D. Huber, "Classification of topological phonons in linear mechanical metamaterials," *Proceedings of the National Academy of Sciences*, vol. 113, no. 33, pp. E4767–E4775, 2016.

[42] O. R. Bilal, R. Süsstrunk, C. Daraio, and S. D. Huber, "Intrinsically polar elastic metamaterials," *Advanced Materials*, vol. 29, no. 26, p. 1700540, 2017.

[43] A. Souslov, B. C. Van Zuiden, D. Bartolo, and V. Vitelli, "Topological sound in active-liquid metamaterials," *Nature Physics*, vol. 13, no. 11, pp. 1091–1094, 2017.

[44] S. Shankar, M. J. Bowick, and M. C. Marchetti, "Topological sound and flocking on curved surfaces," *Physical Review X*, vol. 7, no. 3, p. 031039, 2017.

[45] P. Delplace, J. Marston, and A. Venaille, "Topological origin of equatorial waves," *Science*, p. eaan8819, 2017.

[46] K. v. Klitzing, G. Dorda, and M. Pepper, "New method for high-accuracy determination of the fine-structure constant based on quantized hall resistance," *Physical Review Letters*, vol. 45, no. 6, p. 494, 1980.

[47] D. J. Thouless, M. Kohmoto, M. P. Nightingale, and M. den Nijs, "Quantized hall conductance in a two-dimensional periodic potential," *Physical Review Letters*, vol. 49, no. 6, p. 405, 1982.

[48] C. L. Kane and E. J. Mele, "Quantum spin hall effect in graphene," *Physical review letters*, vol. 95, no. 22, p. 226801, 2005.

[49] B. A. Bernevig, T. L. Hughes, and S.-C. Zhang, "Quantum spin hall effect and topological phase transition in hgte quantum wells," *Science*, vol. 314, no. 5806, pp. 1757–1761, 2006.

[50] W. A. Benalcazar, B. A. Bernevig, and T. L. Hughes, "Quantized electric multipole insulators," *Science*, vol. 357, no. 6346, pp. 61–66, 2017.

[51] C. W. Peterson, W. A. Benalcazar, T. L. Hughes, and G. Bahl, "A quantized microwave quadrupole insulator with topologically protected corner states," *Nature*, vol. 555, no. 7696, p. 346, 2018.

[52] M. Serra-Garcia, V. Peri, R. Süsstrunk, O. R. Bilal, T. Larsen, L. G. Villanueva, and S. D. Huber, "Observation of a phononic quadrupole topological insulatoru," *Nature*, vol. 555, no. 7696, p. 342, 2018.

[53] L. M. Nash, D. Kleckner, A. Read, V. Vitelli, A. M. Turner, and W. T. Irvine, "Topological mechanics of gyroscopic metamaterials," *Proceedings of the National Academy of Sciences*, vol. 112, no. 47, pp. 14495–14500, 2015.

[54] R. Süsstrunk and S. D. Huber, "Observation of phononic helical edge states in a mechanical topological insulator," *Science*, vol. 349, no. 6243, pp. 47–50, 2015.

[55] K. Bertoldi, V. Vitelli, J. Christensen, and M. Van Hecke, "Flexible mechanical metamaterials," *Nature Reviews Materials*, vol. 2, no. 11, pp. 1–11, 2017.

[56] S. M. Douglas, I. Bachelet, and G. M. Church, "A logic-gated nanorobot for targeted transport of molecular payloads," *Science*, vol. 335, no. 6070, pp. 831–834, 2012.

[57] J. L. Silverberg, A. A. Evans, L. McLeod, R. C. Hayward, T. Hull, C. D. Santangelo, and I. Cohen, "Using origami design principles to fold reprogrammable mechanical metamaterials," *science*, vol. 345, no. 6197, pp. 647–650, 2014.

[58] M. Z. Miskin, K. J. Dorsey, B. Bircan, Y. Han, D. A. Muller, P. L. McEuen, and I. Cohen, "Graphene-based bimorphs for micron-sized, autonomous origami machines," *Proceedings of the National Academy of Sciences*, vol. 115, no. 3, pp. 466–470, 2018.

[59] A. Alase, E. Cobanera, G. Ortiz, and L. Viola, "Exact solution of quadratic fermionic hamiltonians for arbitrary boundary conditions," *Physical review letters*, vol. 117, no. 7, p. 076804, 2016.

[60] O. Stenull, C. Kane, and T. Lubensky, "Topological phonons and weyl lines in three dimensions," *Physical review letters*, vol. 117, no. 6, p. 068001, 2016.

[61] D. Z. Rocklin, B.-G. Chen, M. Falk, V. Vitelli, and T. Lubensky, "Mechanical weyl modes in topological maxwell lattices," *Physical review letters*, vol. 116, no. 13, p. 135503, 2016.

[62] J. C. Teo and C. L. Kane, "Topological defects and gapless modes in insulators and superconductors," *Physical Review B*, vol. 82, no. 11, p. 115120, 2010.

[63] X. Mao and T. C. Lubensky, "Maxwell lattices and topological mechanics," *Annual Review of Condensed Matter Physics*, vol. 9, pp. 413–433, 2018.

[64] C. Calladine, "Buckminster fuller's tensegrity structures and clerk maxwell's rules for the construction of stiff frames," *International Journal of Solids and Structures*, vol. 14, no. 2, pp. 161–172, 1978.

[65] E. Cobanera, A. Alase, G. Ortiz, and L. Viola, "Exact solution of corner-modified banded block-toeplitz eigensystems," *Journal of Physics A: Mathematical and Theoretical*, vol. 50, no. 19, p. 195204, 2017.

[66] E. Cobanera, A. Alase, G. Ortiz, and L. Viola, "Generalization of bloch's theorem for arbitrary boundary conditions: Interfaces and topological surface band structure," *Physical Review B*, vol. 98, no. 24, p. 245423, 2018.

[67] C. Kane, "Topological band theory and the z2 invariant," *Topological Insulators*, vol. 6, p. 1, 2013.

[68] W. Su, J. Schrieffer, and A. J. Heeger, "Solitons in polyacetylene," *Physical review letters*, vol. 42, no. 25, p. 1698, 1979.

[69] L. Zhang and X. Mao, "Fracturing of topological maxwell lattices," *New Journal of Physics*, vol. 20, no. 6, p. 063034, 2018.

[70] R. K. Pal and M. Ruzzene, "Edge waves in plates with resonators: an elastic analogue of the quantum valley hall effect," *New Journal of Physics*, vol. 19, no. 2, p. 025001, 2017.

[71] P. Delplace, D. Ullmo, and G. Montambaux, "Zak phase and the existence of edge states in graphene," *Physical Review B*, vol. 84, no. 19, p. 195452, 2011.

[72] J. Zak, "Berry's phase for energy bands in solids," *Physical review letters*, vol. 62, no. 23, p. 2747, 1989.

[73] D. Thouless, "Quantization of particle transport," *Physical Review B*, vol. 27, no. 10, p. 6083, 1983.

[74] V. V. Albert, L. I. Glazman, and L. Jiang, "Topological properties of linear circuit lattices," *Physical review letters*, vol. 114, no. 17, p. 173902, 2015.

[75] K. Roychowdhury and M. J. Lawler, "Classification of magnetic frustration and metamaterials from topology," *Physical Review B*, vol. 98, no. 9, p. 094432, 2018.

[76] B. G.-g. Chen, N. Upadhyaya, and V. Vitelli, "Nonlinear conduction via solitons in a topological mechanical insulator," *Proceedings of the National Academy of Sciences*, vol. 111, no. 36, pp. 13004–13009, 2014.

[77] M. D. Fronk and M. J. Leamy, "Higher-order dispersion, stability, and waveform invariance in nonlinear monoatomic and diatomic systems," *Journal of Vibration and Acoustics*, vol. 139, no. 5, 2017.

[78] C. Coulais, D. Sounas, and A. Alù, "Static non-reciprocity in mechanical metamaterials," *Nature*, vol. 542, no. 7642, p. 461, 2017.

[79] M. Baus and R. Lovett, "Generalization of the stress tensor to nonuniform fluids and solids and its relation to saint-venants strain compatibility conditions," *Physical review letters*, vol. 65, no. 14, p. 1781, 1990.

[80] D. Zhou, L. Zhang, and X. Mao, "Topological boundary floppy modes in quasicrystals," *Physical Review X*, vol. 9, no. 2, p. 021054, 2019.

[81] S. Guest and J. Hutchinson, "On the determinacy of repetitive structures," *Journal of the Mechanics and Physics of Solids*, vol. 51, no. 3, pp. 383–391, 2003.

[82] D. Z. Rocklin, S. Zhou, K. Sun, and X. Mao, "Transformable topological mechanical metamaterials," *Nature communications*, vol. 8, p. 14201, 2017.

[83] K. Sun and X. Mao, "Continuum theory for topological edge soft modes," *Physical Review Letters*, vol. 124, no. 20, p. 207601, 2020.

[84] A. J. Liu and S. R. Nagel, "Nonlinear dynamics: Jamming is not just cool any more," *Nature*, vol. 396, no. 6706, p. 21, 1998.

[85] S. Torquato, A. Donev, and F. Stillinger, "Breakdown of elasticity theory for jammed hard-particle packings: conical nonlinear constitutive theory," *International journal of solids and structures*, vol. 40, no. 25, pp. 7143–7153, 2003.

[86] C. Coulais, C. Kettenis, and M. van Hecke, "A characteristic length scale causes anomalous size effects and boundary programmability in mechanical metamaterials," *Nature Physics*, vol. 14, no. 1, pp. 40–44, 2018.

[87] B. Deng, C. Mo, V. Tournat, K. Bertoldi, and J. R. Raney, "Focusing and mode separation of elastic vector solitons in a 2d soft mechanical metamaterial," *Physical review letters*, vol. 123, no. 2, p. 024101, 2019.

[88] M. Miniaci, R. K. Pal, B. Morvan, and M. Ruzzene, "Experimental observation of topologically protected helical edge modes in patterned elastic plates," *Physical Review X*, vol. 8, no. 3, p. 031074, 2018.

[89] J. W. Rocks, N. Pashine, I. Bischofberger, C. P. Goodrich, A. J. Liu, and S. R. Nagel, "Designing allostery-inspired response in mechanical networks," *Proceedings of the National Academy of Sciences*, vol. 114, no. 10, pp. 2520–2525, 2017.

[90] L. Yan, R. Ravasio, C. Brito, and M. Wyart, "Architecture and coevolution of allosteric materials," *Proceedings of the National Academy of Sciences*, vol. 114, no. 10, pp. 2526–2531, 2017.

[91] B. Florijn, C. Coulais, and M. van Hecke, "Programmable mechanical metamaterials," *Physical review letters*, vol. 113, no. 17, p. 175503, 2014.

[92] S. Kim, C. Laschi, and B. Trimmer, "Soft robotics: a bioinspired evolution in robotics," *Trends in biotechnology*, vol. 31, no. 5, pp. 287–294, 2013.

[93] E. Betti, "Teoria della elasticit," *Il Nuovo Cimento*, vol. 7-8, pp. 69–97, 1872.

[94] W. G. Ellenbroek, V. F. Hagh, A. Kumar, M. Thorpe, and M. Van Hecke, "Rigidity loss in disordered systems: Three scenarios," *Physical review letters*, vol. 114, no. 13, p. 135501, 2015.

[95] J. W. Rocks, H. Ronellenfitsch, A. J. Liu, S. R. Nagel, and E. Katifori, "Limits of multifunctionality in tunable networks," *Proceedings of the National Academy of Sciences*, vol. 116, no. 7, pp. 2506–2511, 2019.

[96] S.-D. Liang and G.-Y. Huang, "Topological invariance and global berry phase in non-hermitian systems," *Physical Review A*, vol. 87, no. 1, p. 012118, 2013.

[97] H. Shen, B. Zhen, and L. Fu, "Topological band theory for non-hermitian hamiltonians," *Physical Review Letters*, vol. 120, no. 14, p. 146402, 2018.

[98] H. Flanders, *Differential Forms with Applications to the Physical Sciences by Harley Flanders*, vol. 11. Elsevier, 1963.

[99] G. Baardink, A. Souslov, J. Paulose, and V. Vitelli, "Localizing softness and stress along loops in three-dimensional topological metamaterials," *arXiv preprint arXiv:1707.08928*, 2017.

[100] J. C. Maxwell, "Xlv. on reciprocal figures and diagrams of forces," *The London, Edinburgh, and Dublin Philosophical Magazine and Journal of Science*, vol. 27, no. 182, pp. 250–261, 1864.

[101] L. Cremona, *Two treatises on the graphical calculus and reciprocal figures in graphical statics*. Clarendon Press, 1890.

[102] J. Langbehn, Y. Peng, L. Trifunovic, F. von Oppen, and P. W. Brouwer, "Reflection-symmetric second-order topological insulators and superconductors," *Physical review letters*, vol. 119, no. 24, p. 246401, 2017.

[103] F. Schindler, A. M. Cook, M. G. Vergniory, Z. Wang, S. S. Parkin, B. A. Bernevig, and T. Neupert, "Higher-order topological insulators," *Science advances*, vol. 4, no. 6, p. eaat0346, 2018.

[104] M. J. Lawler, "Supersymmetry protected topological phases of isostatic lattices and kagome antiferromagnets," *Physical Review B*, vol. 94, no. 16, p. 165101, 2016.

[105] J. P. D'Angelo, *Several complex variables and the geometry of real hypersurfaces*, vol. 8. CRC Press, 1993.